DEPARTMENT OF PHYSICS
UNIVERSITY OF JYVÄSKYLÄ
RESEARCH REPORT No. 4/2016

Electron spectroscopy with the SAGE spectrometer

by

Juha Sorri

Academic Dissertation
for the Degree of
Doctor of Philosophy

To be presented, by permission of the
Faculty of Mathematics and Science
of the University of Jyväskylä,
for public examination in Auditorium FYS1 of the
University of Jyväskylä on March 8, 2016
at 12 o'clock noon

Jyväskylä, Finland
February 2016

Preface

> The SAGE spectrometer was constructed as a bridge connecting the gamma ray spectroscopy with the art of electron spectroscopy. The gorge in between is a deep one and the rapids at the bottom are treacherous with lurking stray magnetic fields, sharp toothed high voltage discharges and hidden ground loops. But all these obstacles were overcome by persistent and meticulous work.
>
> *An unpublished start of abstract for Nuclear Structure 2012 conference.*
> *Juha Sorri*

If nothing else I have learned how little I know.

I would like to take this opportunity to thank Professor Paul Greenlees for the help with my thesis in general and Professor Rauno Julin for the insights regarding the ^{194}Po section of my thesis.

The experimental part of this work would not have been possible without the help of Dr. Philippos Papadakis to whom I'm much obliged. Another person worth mentioning in this regard is Dr. Juha Uusitalo who was, and continues to be, around after 4 pm when help was needed.

The members of Atomi Fragor deserve to be mentioned. The football resembling games have been an invaluable way to leave the days work behind and thus a very important part of well being. Thank You all.

Lisäksi haluan kiittää Suojelun Erikoisoston henkilöstöä, joiden kanssa olen viettänyt aikaa kirjaimellisesti "enemmän kuin laki sallii", ikimuistoisista hetkistä ja hyvistä keikoista.

Ja kiitos Minnalle kun olet pitänyt hyvää huolta TouhuTornaadosta allekirjoittaneen ollessa Yliopistolla.

-JSo-

Abstract

Sorri, Juha
Electron spectroscopy with the SAGE spectrometer
Jyväskylä: University of Jyväskylä, 2016, 144 p.
Department of Physics Research Report No. 4/2016
ISSN: 0075-465X; 4/2016
ISBN: ISBN 978-951-39-6539-6 (paper version)
ISBN: ISBN 978-951-39-6540-2 (electronic version)

A device called the SAGE (Silicon And GErmanium) spectrometer, designed for in-beam electron spectroscopy, is introduced in this work. A detailed description to the technical aspects of the device is given along with several examples of analytical procedures related to work done with the device. The radial filtering method and veto/add-back algorithms are tools for improving the quality of the electron-gamma data whilst the time-gate selection procedure helps in determining absolute internal conversion coefficients without reference points.

Two very different types of experiments with results obtained from the electron data are introduced and analysed. Coulomb excitation is used to probe ^{154}Sm and a more typical fusion-evaporation reaction is used to produce ^{194}Po. The ^{154}Sm study is serves mainly for introduce the new analysis methods and no gains are made when compared to other recent works on this isotope. In the ^{194}Po analysis, despite some experimental pitfalls, the mystery regarding the doublets in the electron spectrum measured with SACRED is solved and a possible extension to the known level scheme of ^{194}Po is given.

Keywords: Electron spectroscopy, Instrumentation, ^{154}Sm, ^{194}Po

Author's address Juha Sorri
Department of Physics
University of Jyväskylä
Finland

Supervisors Prof. Paul Greenlees
Department of Physics
University of Jyväskylä
Finland

Reviewers Dr. Tibor Kibédi
Department of Nuclear Physics
Australian National University
Australia

Dr. Adam Garnsworthy
TRIUMF
Canada

Opponents Prof. Andreas Görgen
Department of Physics
University of Oslo
Norway

Contents

1 Introduction **19**

1.1 Experimental challenges 19

1.1.1 Solution 19

1.2 Early phases of the SAGE spectrometer 23

2 Theory **25**

2.1 Physics background 25

2.1.1 Structure of the atom 25

2.1.2 Spherical shell model 26

2.1.3 Deformed nuclei 28

2.1.4 Nilsson model 29

2.1.5 Rotational nuclei 31

2.1.6 Angular momentum and parity selection rules 32

2.1.7 Transition probabilities 33

2.1.8 Transition probabilities in the collective model 34

2.2 Internal conversion 34

2.2.1 Mixing ratio 35

2.2.2 E0 transitions 37

2.2.3 Shape coexistence 38
2.3 γ-γ angular correlations 40
2.4 Detection limits 41

3 Experimental apparatus and techniques 43
3.1 A general description of SAGE 43
3.2 The JUROGAMII germanium array 45
3.3 RITU - Recoil Ion Transport Unit 47
3.4 The GREAT spectrometer 47
3.5 Components of the SAGE spectrometer 49
3.5.1 Generation of the magnetic field 49
3.5.2 Magnetic shielding 51
3.5.3 The SAGE silicon detector 54
3.5.4 Electronics and data acquisition system 56
3.5.5 Vacuum system 57
3.5.6 High voltage barrier technical details 60
3.6 Calculation of the effective HV barrier height 65
3.6.1 Reference case - Point charge 65
3.7 Electron detection efficiency 68
3.8 Experimental tools 69
3.8.1 Coulomb excitation 70
3.8.2 Coulomb excitation safe energy 71
3.9 Fusion-evaporation reactions 72
3.10 Sources of electron background 72
3.10.1 Target matter 72

3.10.2 Other sources 72
3.10.3 Loss processes in flight 73
3.11 Electron distribution in Si-detector 74
3.11.1 Previous experience - the SACRED spectrometer 74
3.11.2 Electron distribution in SAGE 75
3.12 Radial filtering 77
3.12.1 Energy dependence of detection radius 77
3.12.2 Definition of the maximum radius 77
3.13 Kinematic energy correction 79
3.14 Add-back/veto method for SAGE 80
3.14.1 Description of the method 80
3.14.2 Neighbouring pixels 82
3.14.3 Source tests 83
3.14.4 Si detector segment separation 85
3.15 Si detector dead layers 86
3.16 Time gate selection 88
3.17 Angular correlation measurements 91

4 Experimental cases **93**

4.1 Internal conversion coefficients of ^{154}Sm 94
4.1.1 Experiment details 94
4.1.2 Determination of the γ-ray and electron detection efficiencies 96
4.1.3 Extraction of internal conversion coefficients 99
4.2 Transition strengths 101
4.3 ^{154}Sm low gain test 105

4.4 E0 transitions in ^{194}Po 108
4.4.1 Introduction 108
4.4.2 Experimental details 111
4.4.3 Results 119
4.5 Summary of the ^{194}Po results 129

5 Discussion **131**

5.1 Effect of the analysis tools developed 131
5.2 Results from the experiments 132
5.3 Future of the SAGE spectrometer 133

Appendices **135**

A Target thickness study **137**

A.1 Motivation 137
A.2 Procedure 137

List of Figures

1.1 E. Rutherford and H. Robinson apparatus 20

1.2 Lens-type spectrometer 21

1.3 Mini-orange 22

1.4 Solenoid 22

1.5 SPICE 23

1.6 Polish design 24

2.1 Nuclear potentials 26

2.2 Single-particle states 27

2.3 Oblate and prolate 29

2.4 Single-particle orbitals 30

2.5 Angular momentum schematics 30

2.6 Ω splitting 31

2.7 Internal conversion coefficients 36

2.8 Two-state mixing 39

2.9 Decay cascade 40

3.1 Total ICC 44

3.2 SAGE spectrometer 45
3.3 JUROGAMII 46
3.4 JUROGAM absolute efficiency 46
3.5 RITU magnets 47
3.6 GREAT 48
3.7 ToF-ΔE 48
3.8 SAGE coils 49
3.9 Magnetic field profile 50
3.10 Thermal load image 51
3.11 Spectrum from BGO shield in stray magnetic field. 52
3.12 BGO signal vs. stray magnetic field 52
3.13 Magnetic shielding 53
3.14 Si detector photograph 54
3.15 Segmentation of the Si detector 54
3.16 PCB and mountings 55
3.17 Si detector drain current 55
3.18 Si detector biasing schemes 56
3.19 DAQ 57
3.20 Pumping scheme 58
3.21 Carbon foil unit 59
3.22 Optional pumping scheme. 59
3.23 Adapter part 60
3.24 HV barrier 61
3.25 HV barrier cross-section 61
3.26 Rendering of the horse shoe connector. 62

3.27 Simplified circuit diagram of the HV barrier. 62

3.28 The HV barrier positioning. 62

3.29 HV barrier leakage current 63

3.30 HV barrier burn mark 64

3.31 HV barrier equivalent geometry 66

3.32 HV barrier ratios 67

3.33 HV barrier relative transmissions 67

3.34 Maximum transmission angle 68

3.35 SAGE electron detection efficiency 69

3.36 SAGE electron detection efficiency with different HV barrier voltages 70

3.37 Nuclear reactions 71

3.38 Simulated electron energy losses 74

3.39 Normalised distribution of electrons with SAGE 75

3.40 Main coil offset 75

3.41 Electron distribution plots 76

3.42 Maximum radii per energy extraction 78

3.43 Maximum radius per energy 78

3.44 Effect of the radial filtering 79

3.45 Add-back/veto algorithm 81

3.46 Scheme 1 add-back (AB1) search patterns 82

3.47 Scheme 2 add-back (AB2) search patterns 82

3.48 A reconstructed ^{207}Bi spectrum 83

3.49 Relative peak areas with different schemes 84

3.50 Main characteristics of ^{207}Bi coincident electrons spectrum detected by the different add-back schemes 84

3.51 Low energy part of the ^{133}Ba coincident electrons spectrum produced by two different add-back schemes 85

3.52 Effect of add-back procedures on the electron detection efficiency. 85

3.53 A comparison of the simulated and experimental electron peak shape generated using the add-back algorithm. 86

3.54 Alpha peaks 87

3.55 PHD effect 88

3.56 Time spectrum from ^{154}Sm Coulex experiment 89

3.57 Relative contributions to time spectum 89

3.58 Gamma-gamma timing 90

3.59 Gamma-electron timing 90

3.61 The angular correlation for ^{154}Sm 276-185 keV cascade. 92

4.1 Partial level scheme of ^{154}Sm 94

4.2 A total JUROGAMII spectrum 95

4.3 The most prominent ^{154}Sm conversion peaks 95

4.4 Partial level schemes of ^{152,154}Sm and ^{166}Yb 97

4.5 Absolute γ-ray and electron detection efficiencies used in the ^{154}Sm analysis. 98

4.6 A comparison between results for internal conversion coefficients 99

4.7 Simulated relative electron transmission 101

4.8 Measured angular correlations for the 1071-185 keV cascade (Sm) 103

4.9 The A2 and A4 parameters as a function of δ (Sm) 103

4.10 Overflow events 105

4.11 Raw silicon detector spectra (low gain) 107

4.12 A γ-ray spectrum gated with high-energy events 107

4.13 Partial level scheme of ^{194}Po 108

4.14 Level systematics for even-mass $^{192-210}$Po isotopes 109

4.15 A ^{194}Po electron spectrum measured with SACRED 110

4.16 A measured time-of-flight versus energy loss matrix from the ^{194}Po experiment 111

4.17 The γ-ray-recoil time gate 112

4.18 The recoil-electron time gate 113

4.19 ^{194}Po alphas 113

4.20 Effect of recoil gating and recoil-decay tagging on the prompt γ-ray spectra 114

4.21 Effect of recoil gating and recoil-decay tagging on the prompt electron spectra 115

4.22 Electron detection efficiency before and after the ^{194}Po experiment with I_{coils}=800 A. 116

4.23 Ratios between measured ICCs 117

4.24 Examples of fits that are used to extract the ^{194}Po ground state ICCs. 118

4.25 A comparison between electron data measured with SACRED and SAGE with alpha tagging 120

4.26 Comparison between projections of accepted and background γ-γ matrices 120

4.27 Example spectra tagged with the ^{194}Po alpha decay 122

4.28 Partial level schemes of ^{194}Po with two possible placements of the 494 keV transition and relative γ-ray intensities. 123

4.29 γ-ray energy spectra projected from the alpha-tagged γ-γ matrix 124

4.30 Alpha-tagged γ-electron matrix 125

4.31 Alpha-tagged γ-ray and electron singles 130

A.1 Thallium target X-ray images 138

List of Tables

2.1 Weisskopf single-particle estimates 33

2.2 Transition probabilities 33

3.1 Simulated electron energy losses in SAGE 73

4.1 Summary of the ^{154}Sm experiment details 96

4.2 Approximate transmission coefficients 101

4.3 Experimental results for α_K ICCs 102

4.4 The monopole transition strengths (Sm) 104

4.5 Experimental results for ^{152,154}Sm monopole transition strengths compared with literature values. 104

4.6 Summary of the ^{194}Po experiment 110

4.7 Peak area estimations related to the observed electron doublet peak 121

4.8 Peak areas related to the 438K electron 127

4.9 Peak areas related to the 525K electron 128

4.10 Measured ICCs compared with calculated mixed ICCs of the inter band transitions with different adopted multipole mixing ratios. 128

4.11 Summary of the measured ICC values for transitions in ^{194}Po . 129

Chapter 1

Introduction

1.1 Experimental challenges

Electron spectroscopy has become a more and more relevant experimental tool as the limits of the nuclear landscape are pushed towards the extremes. Especially in the case of heavy elements where the most commonly used experimental methods that rely on the detection of γ radiation start to fail due to the increasing probability of internal conversion, the emission of an atomic electron rather than a γ-ray. For example, in the first proposed level scheme of ^{254}No [1] the two lowest transitions could not be observed due to the high probability of conversion.

Another area where common observation methods may fail is in the detection of E0 transitions. These transitions can link states of the same spin and parity. In some cases, E0 transitions can link deformed 0^+ states to the 0^+ ground state, one famous example being ^{186}Pb [2]. If the 0^+ state is the first excited state, the most likely decay mode is internal conversion. Pair production becomes possible for transition energies above 1022 keV and higher order processes such as two-photon or two-electron emission are rather rare.

1.1.1 Solution

One can always measure electrons and γ-rays in separate measurements but with this approach electron-γ-ray coincidences are lost, which can lead to an ambiguous assignment of the transitions. A solution combining both γ-ray and electron spectroscopy is needed. The present work introduces an electron

spectrometer called SAGE that was constructed to combine a silicon detector for electron detection and a High-Purity Germanium (HPGe) detector array for γ-ray detection with a recoil separator and focal plane detector system for decay studies. In order to gain perspective it is useful to familiarise oneself with the other existing and historic electron spectrometers and their working principles. In the following section, a selection of devices intended for electron spectroscopy are introduced in a general manner. A more comprehensive and detailed description of various electron/β spectrometers can be found, for example, in Ref. [3].

Rutherford and Robinson apparatus

Maybe the simplest form of an electromagnetic electron spectrometer was introduced by E. Rutherford and H. Robinson [4] in 1913. Their apparatus is in simplicity a source, radiation shield, slits and a photographic plate constructed within a brass vessel, pumped to create vacuum and positioned within the poles of a dipole magnet. A schematic view of the device is shown in figure 1.1. The

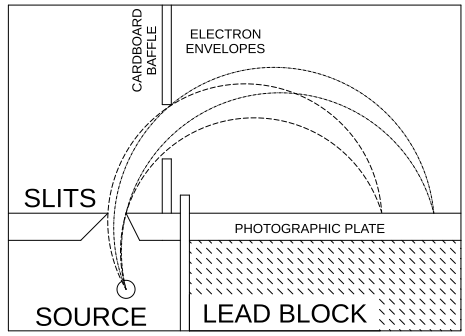

Figure 1.1: A simplified view of the detection system E. Rutherford used in the Radium B and Radium C β-emission analysis. Paths of electrons with different energies are shown in figure. The total size of the main vessel of the device was $\sim$13$\times$13 cm.

cardboard baffle was added to the design to suppress positrons. The energy, or velocity, of the electron was calculated from the exposed positions on the photographic plate. The apparatus produced very good results at the time, even though the intensities of the lines produced at the photographic plate had to be listed with notations like "m.s.- moderately strong". The basic principle of this device was used later, for example, by Berkgvist [5] in Stockholm. Note that modern spectrometers have replaced photographic film with silicon detectors.

Lens type

The first lens type electron (β) spectrometer was introduced by R. A. R. Tricker (1924) [6]. As can be seen from figure 1.2 the device used a magnetic field generated by a solenoid magnet to focus the electrons and a long strip of photographic film to record incident electrons. A large piece of lead was used to shield the film from electromagnetic radiation emitted from the source. The source, lead block and photographic film were placed in a brass box that could be pumped to create vacuum. It is worth noting that Mr. Tricker was under the supervision of E. Rutherford while working with this device.

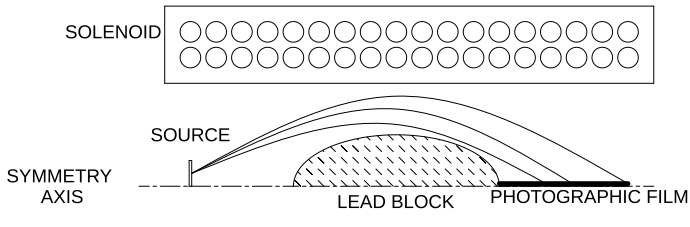

Figure 1.2: A schematic presentation of a lens-type electron spectrometer. Illustrative paths of electrons with different energies are shown. Note that the device has cylindrical symmetry with only half of the cross section drawn and that the full length of the device is ∼40 cm.

Mini-orange

An electron spectrometer described as a mini-orange [7] is constructed of slices of permanent magnets forming a toroidal magnetic field. The magnets are connected to a central piece made of lead or other high-Z material in order to attenuate photon radiation from the source. A detector is mounted on the opposite side of the center piece. A simplified representation of the mini-orange device is shown in figure 1.3. One of the main advantages of the mini-orange is that the system separates positrons and electrons of the same kinetic energy thus lowering the background. The electrons originating from atomic collisions (δ-electrons) are suppressed to some degree depending on the momentum window selected with the magnetic field strength. Another strong point of this kind of system is the compact size. For example, the devices presented in Refs. [7] and [8] are both approximately 12 cm in length. The main disadvantage of this system is the narrow energy window with a reasonable transmission efficiency for a symmetric system, or a low transmission efficiency in general if the magnets are installed in an asymmetric configuration. Mini-orange devices have been successfully used with γ-detectors [9].

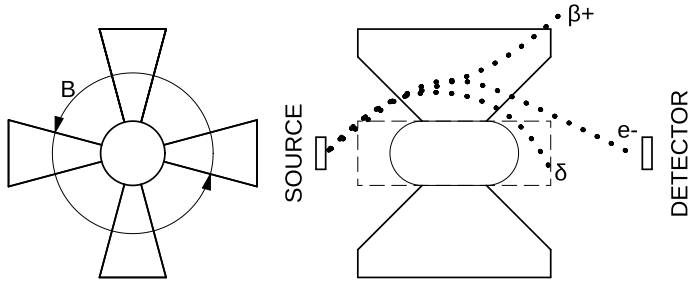

Figure 1.3: A schematic presentation of a mini-orange system. Representative paths of positrons, electrons and δ-electrons are drawn in the figure.

Solenoid type

The solenoid type electron spectrometer is, in a sense, an extension of the lens system. A relatively long solenoid magnet is used to transport electrons from target to detector. As with the lens system, some of the devices incorporate intricate baffles and momentum filters or high voltage elements for background suppression [10, 11, 12]. The basic operational principle of this type of device is shown in figure 1.4. Compared to the pure lens-type device a wider electron energy range can be covered in one measurement and the length (for example, SACRED [12] is 56 cm from target to detector) and structure of the solenoid devices make in-beam measurements feasible. as the electromagnetic radiation emitted at the target dissipates to acceptable level. This is because background radiation produced by the beam interaction with the target can be reduced to a low intensity level to allow observation of the electrons of interest.

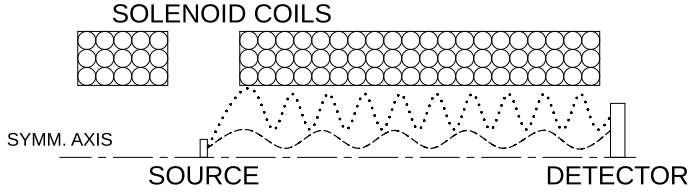

Figure 1.4: A schematic presentation of a solenoid system. Representative paths of electrons with same energies but different emission angles are shown. Note that figure is cylindrically symmetric.

The operational difference between lens and solenoid type spectrometers should be noted. The nature of the lens-type device is such that only electrons within a certain energy range (energy window) are detected with high efficiency. There is no such discrimination in the solenoid type spectrometer without baffle systems, and the detection efficiency in general is dictated by the magnetic field strength

and the physical size of the device.

Other electron spectrometers

There are other kinds of electron spectrometers that do not quite fall into any of the previously presented categories. Examples are SPICE [13] at TRIUMF and the "electron spectrometer for in-beam spectroscopy" [14, 15] at Warsaw/Lodz (later Polish design) and SPEDE [16, 17] at CERN. The first two of these devices employ permanent magnets to bend the electrons to favourable trajectories for detection but do not focus the electrons with different energies as the mini-orange system does. An overview of the SPICE spectrometer is shown in figure 1.5 and the Polish design in figure 1.6. SPEDE is intended for experiments with very low intensity radioactive beams and has no electron optics at all, though some background suppression features are borrowed from common types. At the time of writing, SPICE is undergoing the first commissioning tests. The latter, Polish design, has a low electron detection efficiency at low energies but has been shown to work in experimental conditions [14]. The in-beam commissioning of SPEDE has just been completed but as yet the results are unpublished.

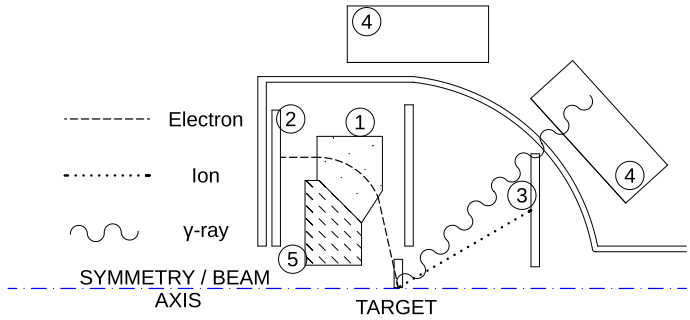

Figure 1.5: An overview of the SPICE spectrometer in TRIUMF. The labelled parts are (1) magnetic lens, (2) silicon detector for electrons, (3) silicon particle detector for heavy ions, (4) germanium detectors and (5) photon shield.

1.2 Early phases of the SAGE spectrometer

Originally, the magnetic configuration of the SAGE spectrometer included permanent magnets near the target position. The purpose of these magnets would have been the same as the electron guide magnets in the Polish design. This

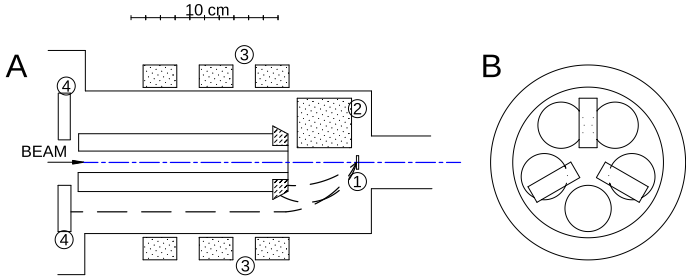

Figure 1.6: A general view of the Polish electron spectrometer. (A) A cut through of the device. The labelled parts are (1) target, (2) selector magnet, (3) electron guide magnets, (4) silicon detectors. (B) Magnet and silicon detector arrangement (other components not shown) as viewed from the target. The figure represents the original configuration shown in Ref. [14].

idea was dropped in favour of an electromagnetic solenoid constructed in tapered geometry. A working prototype with this general design was constructed from parts salvaged from SACRED [12] and was used extensively to test the feasibility of the magnetic field configuration and the effect of the magnetic field on the photomultiplier tubes of the bismuth germanate Compton-suppression shields of JUROGAMII (see section 3.5.2). The work performed with the prototype yielded a number of promising results and had a strong influence on the final design of the SAGE spectrometer. During the commissioning phase of the SAGE spectrometer several surprises were encountered and the present work introduces some of these challenges and the solution and/or explanation of how the situation was dealt with.

The present work introduces the SAGE spectrometer as it came to be. At first an overview of the physics behind the SAGE spectrometer is introduced in Chapter 2. This is followed in Chapter 3 by a description of the technical and the procedural aspects of the spectrometer. Chapters 4 and 5 are reserved for presentation of experimental cases and discussion, respectively. After reading this work, the reader should have a general understanding of the device called the SAGE spectrometer and a view of the possibilities and limitations of the device.

Chapter 2

Theory

2.1 Physics background

2.1.1 Structure of the atom

Liquid drop model

In the 1930s George Gamow proposed that the nucleus can be described as an incompressible drop of nuclear fluid made of α particles with the strong nuclear force holding the liquid drop together [18]. The model was later modified to incorporate the neutron which was discovered in 1932 [19]. The liquid drop model leads to two significant results. Firstly the average radius (R_{av}) of a spherical nucleus can be determined by the mass number A(=Z+N) with the equation

$$R_{av} = r_0 A^{1/3}, \tag{2.1}$$

where r_0 is between 1.20-1.25 fm [20]. Another major contribution of the model is to provide an estimate of the nuclear binding energy and mass as proposed by Carl Friedrich von Weizsäcker [21] in 1935. The factors affecting the nuclear binding can be summarised in an equation for the binding energy (B(Z,A))

$$\begin{aligned} B(Z,A) &= a_v A - a_s A^{2/3} - a_c Z(Z-1)A^{-1/3} \\ &- a_{sym}\frac{(A-2Z)^2}{A} + \begin{cases} +a_p A^{-3/4} & \text{Z and N even} \\ -a_p A^{-3/4} & \text{Z and N odd} \\ 0 & \text{A odd} \end{cases}, \end{aligned} \tag{2.2}$$

where a_v=15.5 MeV is the volume term, a_s=16.8 MeV is the surface term, a_c=0.72 MeV is the Coloumb term, a_{sym}=23 MeV is the symmetry term and a_p=34 MeV is the pairing term [20]. The values of the fitted coefficients and form of the terms vary between sources (see for example Ref. [22]). With this notation the semi-empirical mass formula becomes

$$M(Z,A) = Zm_H + Nm_n - B(Z,A)/c^2 \tag{2.3}$$

where m_H is the atomic mass of a hydrogen atom, m_n the neutron mass, c speed of light and M(Z,A) is the atomic mass of the nucleus in question.

2.1.2 Spherical shell model

The next attempt to describe properties of the nuclei came in the form of the shell model [23]. In the model ,"shells" are filled in order in accordance with the Pauli exclusion principle with proton and neutron shells filled separately. The particles move nearly unperturbed in an effective mean field generated by the other nucleons. Several different approximations of the mean field have been used, the simplest being the square well and harmonic oscillator potentials. However, these simple potentials do not reproduce the shell gaps that correspond to the magic numbers. The more realistic Woods-Saxon potential coupled with spin orbit splitting reproduces the magic numbers exactly [24, 25]. The difference between nuclear potentials is shown in figure 2.1. A common

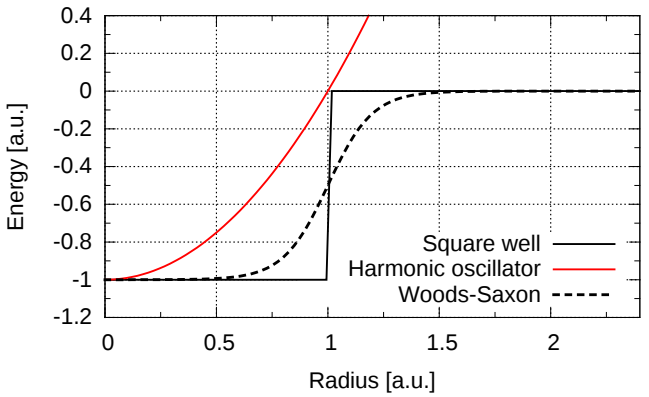

Figure 2.1: A general behaviour of different nuclear potential approximations.

way to parametrize the Woods-Saxon potential (V(r)) is

$$V(r) = -\frac{V_0}{1 + Exp[(r - R_{av})/a]} \tag{2.4}$$

where R_{av} is given by equation 2.1 with r_0=1.25 fm, V_0=50 MeV. The parameter a is the so-called diffuseness parameter [26], equal to 0.6 fm. The Schrödinger equation with a Woods-Saxon potential can be solved in three dimensions and the resulting level energies are shown in figure 2.2. The states are marked according to the orbital angular momentum ℓ in the infinite well case. The first five ℓ values (0 to 4) are labelled s, p, d, f, g. The following ℓ states are labelled in order of increasing energy.

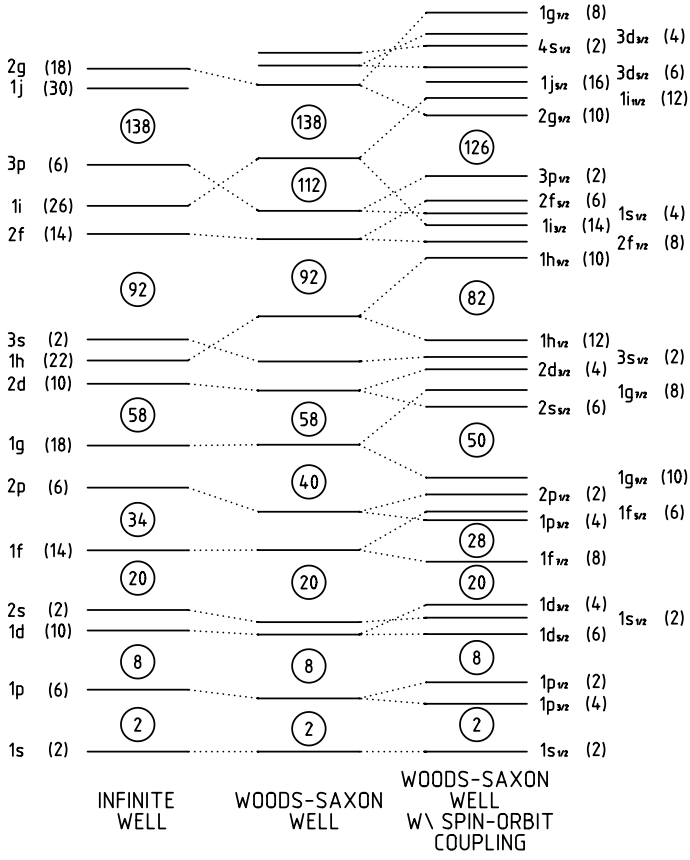

Figure 2.2: Single-particle states calculated with different potential models. The Woods-Saxon potential is as described in equation 2.4. The maximum number of protons or neutrons per state is in parentheses. The closed shell magic numbers are circled. The figure is reproduced from [26].

Spin-orbit coupling

The spin-orbit potential has a form -$V_{so}(r)\mathbf{l}\cdot\mathbf{s}$ where l is the orbital angular momentum and s is the spin of a nucleon moving in the potential well. As the spin s equals to 1/2 the total angular momentum j can have values j=$\ell\pm1/2$. Now the expectation value of $\mathbf{l}\cdot\mathbf{s}$ is

$$\langle\mathbf{l}\cdot\mathbf{s}\rangle = \frac{1}{2}[j(j+1)-\ell(\ell+1)-s(s+1)]\hbar^2. \tag{2.5}$$

Substituting for j and s leads to (when $\ell\neq0$)

$$\langle\mathbf{l}\cdot\mathbf{s}\rangle = \begin{cases} \frac{1}{2}\ell\hbar^2, & j=\ell+1/2 \\ -\frac{1}{2}(\ell+1)\hbar^2, & j=\ell-1/2 \end{cases} \tag{2.6}$$

When the spin-orbit potential is added to the Woods-Saxon potential the single-particle states shift as shown in figure 2.2. As a result the commonly accepted magic numbers 2, 8, 20, 28, 50, 82, and 126 are reproduced [27]. In this case, the spectroscopic notation used to label the states (rightmost levels in figure 2.2) changes such that the total angular momentum j is included as a superscript. The degeneracy of the resulting states becomes 2j+1.

2.1.3 Deformed nuclei

In the vicinity of the closed shells the mean field can be described by a spherical potential. When moving away from closed shells the nucleus can deform and it is more convenient to present the shape of the nucleus as a sum of spherical harmonics as described for example in refs. [20, 22, 28]. Commonly the surface of a deformed nucleus can be described by

$$R(\Omega,\varphi) = R_{av}\left[1+\beta Y_{20}(\Omega,\varphi)\right], \tag{2.7}$$

where Ω,φ are the angles of the radius vector, R_{av} is defined by equation 2.1 and Y_{20} is the spherical harmonics function. Note that equation 2.7 describes only the cases with axial symmetry. The deformation parameter β is given by the equation

$$\beta = \frac{4}{3}\sqrt{\frac{\pi}{5}}\frac{\Delta R}{R_{av}}, \tag{2.8}$$

where ΔR is the difference between major and semi-major axes [20] of the ellipsoid. When $\beta<0$ the nucleus is said to have oblate deformation and with $\beta>0$ prolate deformation. A visualisation of these nuclear shapes is shown in figure 2.3.

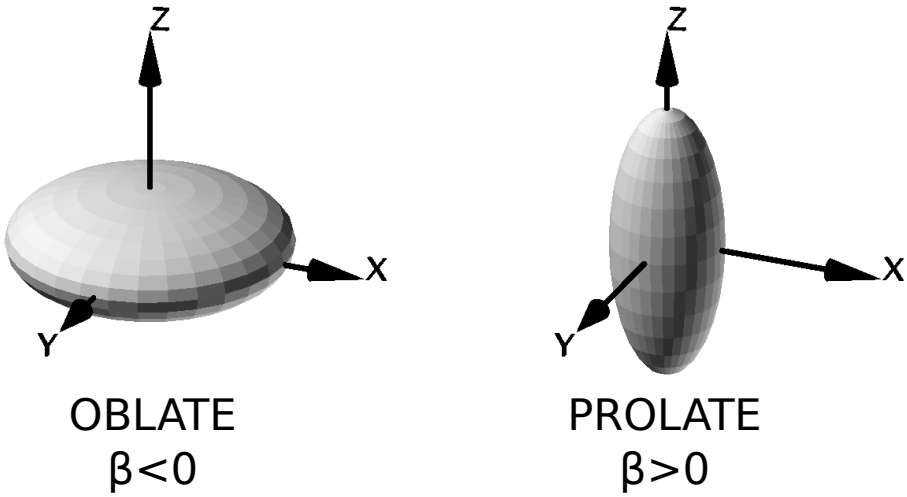

Figure 2.3: Oblate and prolate deformed nuclear shapes. Note that the z axis is commonly selected as the symmetry axis.

2.1.4 Nilsson model

The deformed shell model is often called the Nilsson model [29]. The general features of the model can be derived without calculations via a few simple assumptions. Firstly one assumes a single-particle shell model potential with a deformation of β, and secondly an attractive nuclear force with a short range. The energy of the single-particle orbit is now dependent on the orientation of the orbit compared to nuclear orientation (z axis). Schematically this can be seen from figure 2.4.

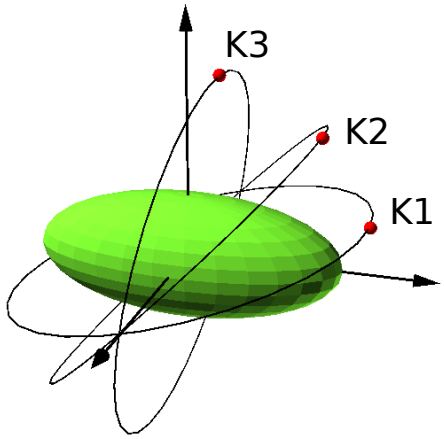

Figure 2.4: An example of single-particle orbits with different angle with respect to the symmetry axis in a prolate deformed nucleus.

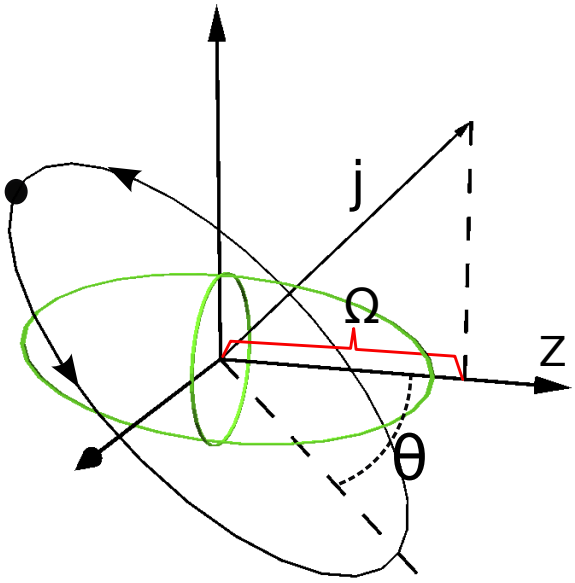

Figure 2.5: A schematic representation of relation between total angular momentum j, projection Ω and angle of orbital plane θ.

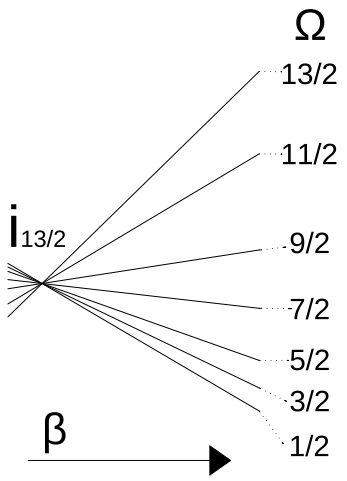

Figure 2.6: A schematic representation of Ω splitting with prolate deformation.

The orbit K1 will have a lower energy than orbit K2, which in turn will have a lower energy than orbit K3 in the case of prolate deformation. The orientation can be specified by the projection of the total angular momentum (j) on the symmetry axis, labelled as Ω. The classical orbits can be assumed to correspond to different Ω values, for example j=13/2 with Ω=1/2...13/2. As seen in figure 2.5 the orbital plane angle with respect to the symmetry axis can be approximated from j and Ω by θ=$\sin^{-1}(\Omega/j)$. If prolate deformation (β >0) is considered simple conclusions about the evolution of the energies of the single-particle orbits can be made. Orbits with small Ω are "closer" to the nuclear surface and are drawn lower in energy, orbits with large Ω are "further" from the surface thus higher in energy. Such conceptual ideas can describe the main features of the so-called Nilsson diagrams, which plot the single-particle energies as a function of deformation parameter. As an example, the variation of single-particle energies of $i_{13/2}$ orbits with different Ω is shown in figure 2.6. Based on a fundamental quantum mechanical rule that levels with same quantum numbers cannot coincide, meaning that states with the same Ω and parity repel each other, the full schematic Nilsson diagrams can now be drawn. More detailed Nilsson diagrams are shown for example in the appendices of Ref. [31]. Note that it is common for tabulations of the properties of Nilsson states to be made as a function of $\epsilon \approx 0.95\beta$ with orbit labels of $\Omega^{\pi}[Nn_z\Lambda]$, where π refers to parity, N to the principal quantum number of the major shell, n_z to the number of nodes in the wave function in the z-direction and Λ the component of the orbital angular momentum in the z-direction. By definition Ω=Λ±1/2.

2.1.5 Rotational nuclei

The rotational energy of a quantum mechanical rotating object is given by

$$E(I) = \frac{\hbar^2}{2\mathcal{J}} I(I+1) \tag{2.9}$$

where I is the angular momentum (spin) and $\mathcal{J}$ the moment of inertia of the nucleus. If the rotor is ideal the moment of inertia is constant, but in general for atomic nuclei it is found that this is not the case. The energy level sequence given by equation 2.9 is called a rotational band. The rotational behaviour of nuclei can be presented through three different moments of inertia. The static

($\mathcal{J}$), kinematic ($\mathcal{J}^{(1)}$) and dynamic ($\mathcal{J}^{(2)}$) moments of inertia. The kinematic moment of inertia is defined as [32]

$$\mathcal{J}^{(1)}(I) = \hbar^2 I \left[\frac{dE(I)}{dI}\right]^{-1}, \tag{2.10}$$

and the dynamic moment of inertia

$$\mathcal{J}^{(2)}(I) = \hbar^2 \left[\frac{d^2E(I)}{dI^2}\right]^{-1}. \tag{2.11}$$

Samuel M. Harris proposed that $\mathcal{J}^{(1)}$ is a variable of the nuclear angular velocity (ω) and can be expressed as

$$\mathcal{J}^{(1)}(\omega) = \mathcal{J}_0 + \mathcal{J}_1\omega^2 \tag{2.12}$$

where $\mathcal{J}_0$ and $\mathcal{J}_1$ are the so called Harris parameters [33]. If some of the energies of the states in the rotational band can be determined, the Harris parameters can be used to extrapolate energies of unknown states. For E2 transitions $\omega \approx E_\gamma/2\hbar$ and $\mathcal{J}^{(1)} \approx (I - 1/2)/\omega(I)$ [34]. E_γ is the energy difference between the initial state and the final state ($E_\gamma = E_i - E_f$). This leads to the expression

$$I = \mathcal{J}_0\omega + \mathcal{J}_1\omega^3 + 1/2 \tag{2.13}$$

where I is the spin of the initial state from which the transition proceeds.

2.1.6 Angular momentum and parity selection rules

Based on the classical theory of electromagnetic radiation changes in the nucleus can be divided into magnetic (M) and electric (E) transitions depending in which field the change happens. In addition, in both cases the resulting transition can be characterized by a multipole order 2^L where L=1 for dipole, 2 for quadrupole and so on. The multipolarity (L) of the transition is governed by selection rules defined by equations 2.14 and 2.15.

$$|I_i - I_f| \leq L \leq I_f + I_i \tag{2.14}$$

$$\begin{aligned} \pi_i &= \pi_f \quad \text{even E ; odd M} \\ \pi_i &= -\pi_f \quad \text{odd E ; even M} \end{aligned} \tag{2.15}$$

where I_i, π_i and I_f, π_f are the angular momenta and parities of the initial and final nuclear states , respectively,and L is the multipole order of the transition.

2.1.7 Transition probabilities

In addition to the excitation energy of a nuclear state, the half life can also be deduced. The half life ($t_{1/2}$) can be expressed as

$$t_{1/2} = \frac{ln2}{\lambda_{fi}}, \tag{2.16}$$

where λ_{fi} is the transition probability. Commonly electromagnetic transition probabilities are expressed in terms of the Weisskopf units (Wu.) based on Weisskopf single-particle estimates as shown in table 2.1. The basic assumption of the Weisskopf estimate is that the transition is due to a single proton moving from one shell model state to another. A transition probability much less than 1 Wu. indicates a poor matching between the initial and final state wavefunctions and a transition probability much more than 1 Wu. indicates that more than one nucleon is taking part in the transition.

Table 2.1: Weisskopf single-particle estimates (λ_W) for the most common transitions. L is the multipole order of the transition and the transition energy E should be given in MeV. A is the mass number of the nucleus in question.

EL	$\lambda_W[1/s]$	ML	$\lambda_W[1/s]$
E1	$1.0 \times 10^{14} A^{2/3} E^3$	M1	$3.2 \times 10^{13} E^3$
E2	$7.3 \times 10^{7} A^{4/3} E^5$	M2	$2.3 \times 10^{7} A^{2/3} E^5$
E3	$34 \times A^2 E^7$	M3	$11 \times A^{4/3} E^7$
E4	$1.1 \times 10^{-5} A^{8/3} E^9$	M4	$3.3 \times 10^{-6} A^2 E^9$

Another typical way to introduce transition probabilities is with reduced transition probabilities as shown in table 2.2.

Table 2.2: Transition probabilities presented in terms of the reduced transition probabilities B(ML), B(EL). Units for B(ML), B(EL) are $(\mu_N/c)^2 fm^{2L-2}$ and $e^2 fm^{2L}$, respectively. Transition energy E should be given in MeV.

EL	$\lambda[1/s]$	ML	$\lambda[1/s]$
E1	$1.6 \times 10^{15} E^3 B(E1)$	M1	$1.8 \times 10^{13} E^3 B(M1)$
E2	$1.2 \times 10^{9} E^5 B(E2)$	M2	$1.4 \times 10^{7} E^5 B(M2)$
E3	$5.7 \times E^2 B(E3)$	M3	$6.4 \times E^7 B(M3)$
E4	$1.7 \times 10^{-4} E^9 B(E4)$	M4	$3.9 \times 10^{-6} E^9 B(M4)$

2.1.8 Transition probabilities in the collective model

The collective motion of a group of nucleons can lead to large disturbances in the electromagnetic field of the nucleus, which can lead to higher probabilities of γ-ray emission. Primarily, E2 transitions are affected as they are related to the nuclear quadrupole moment. As an example, reduced transition probability of an E2 transition is

$$B(E2 : I_i \rightarrow I_f) = \frac{5}{16\pi} Q_0^2 \mid \langle I_i K_i 20 \mid I_f K_f \rangle \mid^2, \tag{2.17}$$

where Q_0 is the intrinsic quadrupole moment, K is the projection of the total angular momentum onto the symmetry axis and $\mid \langle I_i K_i 20 \mid I_f K_f \rangle \mid$ is a Clebsch-Gordan coefficient [35]. An expression for Q_0 is given, for example, in Ref. [20]

$$Q_0 = \frac{3}{\sqrt{5\pi}} R_{av}^2 Z \beta_2 (1 + 0.16\beta_2), \tag{2.18}$$

where R_{av} is given by equation 2.1. The equation for Q_0 can be approximated further after applying equation 2.1. Now:

$$Q_0 = \frac{3}{\sqrt{5\pi}} (r_0 A^{1/3})^2 Z \beta_2 (1 + 0.16\beta_2) \xrightarrow[0.16\beta \ll 1]{r_0 \sim 1.25} \approx 1.18 A^{2/3} \beta_2 Z. \tag{2.19}$$

Combining equations 2.17 and 2.19 and substituting this into the expression for $\lambda(E2)$ from table 2.2 yields

$$\lambda(E2) \approx 3 \times 10^7 E^5 A^{4/3} \beta_2^2 Z^2 \frac{1}{5} \quad [1/s], \tag{2.20}$$

for K=0, I=2 transitions with I_i=I and I_f=I-2. If equation 2.20 is compared to the Weisskopf estimate for E2 transition probability from table 2.1 the collective model gives transition probabilities larger by an approximate factor of $Z^2\beta_2^2$ for a given E and A.

2.2 Internal conversion

Internal conversion is a process that competes with γ-ray emission. Electromagnetic multipole fields generated by the nucleus interact with atomic electrons causing one of them to be ejected. It is worth noting that contrary to β emission, the electron is not created in the decay process but an existing electron is ejected from an atomic orbital. The energy of the ejected electron (E_i) is defined by equation 2.21

$$E_i = \Delta E - B_i, \tag{2.21}$$

where ΔE is the transition energy and B_i the binding energy of the atomic orbital (i=K,L,M...). The binding energy values, can be found in the appendices

of Ref. [31] (published originally in Ref [36]). The ratio of transition rate due to internal conversion to that from γ-ray emission is described by the internal conversion coefficient (ICC, α). The ICC can be defined via transition probabilities (Ref. [20]) or count rates (Refs [37, 38]). The basic formulation for total ICC (α_T) is therefore

$$\alpha_T = \frac{\lambda_e}{\lambda_\gamma} \text{ or } \frac{T_e}{T_\gamma}, \tag{2.22}$$

where λ_e and λ_γ are the transition probabilities as defined by the exponential decay law for electron and γ-ray emission, respectively, and T_e and T_γ are the electron and γ-ray emission rates respectively. Naturally the total internal conversion coefficient (α_T) is a sum of partial conversion coefficients (α_i i=K,L,M...) representing the individual atomic shells and α_π representing the pair conversion coefficient. By using the λ notation of equation 2.22 the internal conversion coefficient and total decay probability (λ_t) are connected by the relation

$$\lambda_t = \lambda_\gamma(1 + \alpha_T) = \lambda_\gamma(1 + \alpha_K + \alpha_L + \alpha_M ... + \alpha_\pi). \tag{2.23}$$

Non-relativistic approximations for the internal conversion coefficients are given by equations 2.24 and 2.25.

$$\alpha(EL) \cong \frac{Z^3}{n^3}\left(\frac{L}{L+1}\right)\left(\frac{e^2}{4\pi\epsilon_0\hbar c}\right)^4\left(\frac{2m_ec^2}{E}\right)^{L+5/2}, \tag{2.24}$$

$$\alpha(ML) \cong \frac{Z^3}{n^3}\left(\frac{e^2}{4\pi\epsilon_0\hbar c}\right)^4\left(\frac{2m_ec^2}{E}\right)^{L+3/2}, \tag{2.25}$$

where Z is the atomic number of the atom, n is the principal quantum number of the electron orbital and L is the multipole order. The factor $e^2/4\pi\epsilon_0\hbar c$ is the fine structure constant with a value$\approx$1/137, m_e is the electron mass and E is the transition energy in MeV. As an example, M1 and E2 internal conversion coefficients are calculated for samarium (Z=62) and shown in figure 2.7. Later in the text ICC values are calculated by means of a more modern BrIcc internal conversion calculator [38].

2.2.1 Mixing ratio

As shown by the parity and angular momentum selection rules the transition type and multipole order is ambiguous. For example if I_i=3$^-$ and I_f=2$^+$ the possible transition types are E1,M2,E3,M4 and E5. As can be seen from the Weisskopf estimates, usually the lower multipole orders dominate. For the most common case with competing ML and E(L+1) transitions the ICCs and mixing ratio (δ) have the relation

$$\alpha = \frac{\alpha_{ML} + \delta^2\alpha_{E(L+1)}}{1 + \delta^2}, \tag{2.26}$$

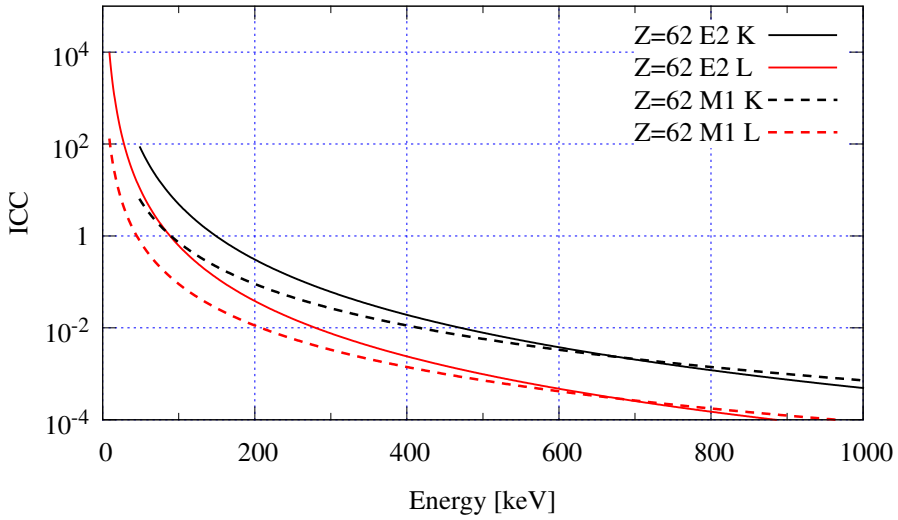

Figure 2.7: Internal conversion coefficients for M1 and E2 type transitions for Z=62 calculated using equations 2.24 and 2.25.

where δ^2 is defined as

$$\delta^2 = \frac{N(E(L+1))}{N(ML)} \overset{Exp}{\Longrightarrow} \frac{\alpha_{ML} - \alpha_{exp}}{\alpha_{exp} - \alpha_{E(L+1)}}, \tag{2.27}$$

where α_{Exp} is the measured conversion coefficient, α_{ML} and $\alpha_{E(L+1)}$ are the calculated conversion coefficients for pure ML and E(L+1) transitions and N(E(L+1)) and N(ML) are the number of E(L+1) and ML type transitions, respectively [37, 38].

Single-particle estimate of the mixing ratio

An estimation of the magnitude of the mixing ratio can be derived from Weisskopf estimates [39]. A single "Weisskopf unit" for the absolute value of the mixing ratio can be calculated with equation

$$|\delta(E2/M1)| = 1.521 \times 10^{-3} E_\gamma A^{2/3}, \tag{2.28}$$

where E_γ is in MeV.

2.2.2 E0 transitions

When the spin and parity of the initial and final states are the same, equations 2.14 and 2.15 show that E0 transitions are possible. Furthermore in the case where the final and initial states have zero spin the only possible transition is E0. Usually E0 transitions proceed through internal conversion but electron-positron pair (e^-, e^+) production is possible if the transition energy is greater than twice the electron rest mass. A simultaneous emission of two γ-rays between the 0^+ states is possible but very unlikely [40]. The transition probability for an E0 transition ($\lambda(E0)$) is given by the expression [38]

$$\lambda(E0) = \frac{1}{\tau(E0)} = \lambda_{ic}(E0) + \lambda_{\pi}(E0), \tag{2.29}$$

where $\tau(E0)$ is the partial mean life of the initial state for E0 decay. The quantities $\lambda_{ic}(E0)$ and $\lambda_{\pi}(E0)$ are the transition probabilities for internal conversion and pair production, respectively. In the following $\lambda_{\pi}(E0)$ will be omitted due to the negligible relative contribution for the low-energy transitions and heavy nuclei discussed in this work. With this simplification $\lambda_{ic}(E0)$ is given by the expression

$$\lambda_{ic}(E0) = \rho^2(E0)\Omega_{ic}(E0), \tag{2.30}$$

where $\rho(E0)$ is the monopole transition strength and $\Omega_{ic}(E0)$ is a total electronic factor [41]. The monopole matrix element is related to $\rho(E0)$ through the equation

$$\rho(E0) = \frac{\langle f|M(E0)|i\rangle}{eR_{av}^2}, \tag{2.31}$$

where e is the electron charge and R_{av} is the nuclear radius defined by equation 2.1. Now the reduced E0 transition probability (B(E0)) is

$$B(E0) = \rho^2(E0)e^2R_{av}^4 \tag{2.32}$$

where $B(E0)$ is the square of the E0 matrix element. The ratio between E0 and E2 reduced transition probabilities (X(E0/E2)) is defined as [42]:

$$X(E0/E2) \equiv \frac{B(E0)}{B(E2)} = \frac{\rho^2(E0)e^2R_{av}^4}{B(E2)}. \tag{2.33}$$

For K conversion electrons

$$X(E0/E2) = 2.54 \times 10^9 \times A^{4/3} \times q_K^2(E0/E2)\frac{\alpha_K(E2)}{\Omega_K(E0)}E_{\gamma}^5, \tag{2.34}$$

where E_{γ} is the transition energy in MeV, $q_K^2(E0/E2)$ is the ratio between E0 and E2 K conversion rates [43], $\alpha_K(E2)$ the K conversion coefficient for a pure E2 transition and $\Omega_K(E0)$ is the electronic factor [41]. With calculated

electronic factors, the monopole strength may be obtained using the partial mean life of the E0 transition ($\tau(E0)$)

$$\rho^2(E0) = \frac{1}{[\Omega_K(E0) + \Omega_{L1}(E0) + ... + \Omega_\pi(E0)] \times \tau(E0)}. \tag{2.35}$$

Alternatively, if the E2 transition rate $\lambda_\gamma(E2)$ is known, $\rho^2(E0)$ can be obtained from the expression

$$\rho^2(E0) = q_K^2(E0/E2)\frac{\alpha_K(E2)}{\Omega_K(E0)} \times \lambda_\gamma(E2). \tag{2.36}$$

An expression for $\rho^2(E0)$ for the quadrupole deformed rotor (Ref. [44]) is

$$\rho^2(E0; n_\beta = 1 \rightarrow n_\beta = 0) = \frac{B(E2; 0^+_{gsb} \rightarrow 2^+_\beta)4\beta_0^2}{e^2 r_0^4 A^{4/3}}, \tag{2.37}$$

where β_0 is the static quadrupole deformation of the ground state, $r_0 = 1.2$ fm, B(E2) in units of e^2fm^4.

E0/M1/E2 mixing

For transitions with between states of the same spin and parity (I≠0), the factor $q_K^2(E0/E2)$ can be expressed by means of

$$q_K^2(E0/E2) = \frac{N(E0)}{N(E2)}, \tag{2.38}$$

where N(E0) and N(E2) are the intensities of the converted E0 and E2 components. The K-shell conversion coefficient (α_K) is related to the $q_K^2(E0/E2)$ value and can be calculated from

$$\alpha_K = \frac{\alpha_K(M1) + \delta^2(E2/M1)\left[1 + q_K^2(E0/E2)\right]\alpha_K(E2)}{1 + \delta^2(E2/M1)}. \tag{2.39}$$

The conversion coefficient α_K is related to monopole transition strength with equation 2.36. Equation 2.39 can be used to calculate $q_K^2(E0/E2)$. Substituting α_K with the experimentally measured α_K^{exp} and rearranging gives

$$q_K^2(E0/E2) = \frac{\alpha_K^{exp}(1 + \delta^2(E2/M1) - \alpha_K(M1))}{\delta^2(E2/M1)\alpha_K(E2)} - 1. \tag{2.40}$$

2.2.3 Shape coexistence

The deformation-dependent splitting of single-particle orbit energies described with the Nilsson orbitals (section 2.1.4) results in up- and down-sloping orbit energies. Due to gaps in the level energies, configurations with spherical,

prolate or oblate shape can be formed with similar energies. The quadrupole interactions make it possible that states with similar spin and parity interact and the resulting mixed states get repulsed. A schematic representation of this two-state mixing is shown in figure 2.8. The magnitude of the mixing (b) can be calculated with the formula

$$\delta E = b^2 \Delta E_p, \tag{2.41}$$

where δE is the energy difference between unperturbed and perturbed states and ΔE_p is the energy difference between the two perturbed states [45].

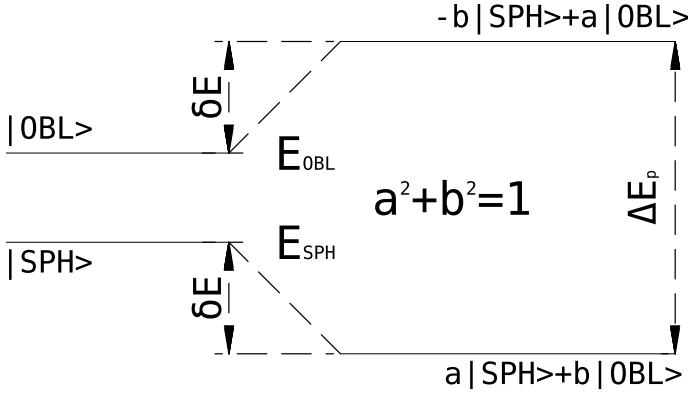

Figure 2.8: A schematic representation of two-state mixing between spherical and oblate shapes. Figure is adopted from Ref. [46].

E0 transitions in the coexistence model

E0 transitions between states of the same spin and parity but with different shapes are allowed only if the states are mixed. If the mixing is between spherical and oblate (or prolate) shapes the monopole transition strength can be calculated from [47]

$$\rho(E0) \approx \frac{abk\beta_2^2}{eR_{av}^2}, \tag{2.42}$$

where a and b are the mixing amplitudes ($a^2+b^2 = 1$) and β_2^2 is the deformation parameter of the deformed configuration and R_{av} is defined by equation 2.1. The coefficient k can be calculated with equation [46]

$$k = \frac{3}{4\pi} ZeR^2 \left[1 + \frac{4\pi^2}{3} \left(\frac{a}{R_{av}} \right)^2 \right], \tag{2.43}$$

where a is the nuclear surface diffuseness parameter with a typical value of $\sim$0.63. A more general form for ρ^2(E0) given by Ref [44] is

$$\rho^2(E0) = \left(\frac{3Z}{4\pi}\right)^2 a^2(1-a^2)[\Delta(\beta_2^2)]^2, \tag{2.44}$$

where $\Delta(\beta_2^2)$ refers to difference of the β_2 deformation parameter between the two different configurations. In a strong mixing situation ($a \sim 1/\sqrt{2}$) the transition strength has the form

$$\rho^2(E0) = \frac{1}{4}\left(\frac{3}{4\pi}\right)^2 Z^2(\beta_1^2 - \beta_2^2)^2. \tag{2.45}$$

2.3 γ-γ angular correlations

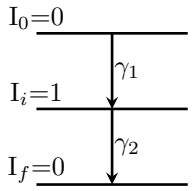

Figure 2.9:
A decay cascade.

One method to determine the multipole order of measured γ-ray transition the angular distribution of the radiations is to measure an angular distribution or an angular correlation of the emitted radiation [20]. Assume a cascade where the first γ-ray (γ_1) occurs between states I_0 and I_i, and the second between I_i and I_f. Illustration of the decay cascade is shown in figure 2.9. The I_i state includes all the possible m-substates $m_{i\in\pm\Delta I}$ and the final level has only one sublevel m_f. The resulting γ-rays emitted from neighbouring m-substates will have an energy deviation of $\Delta E{=}\mu B/I_i$ where μ is the magnetic moment and B is the strength of the external magnetic field. The energy deviation is usually much smaller than the typical γ-ray detection resolution of 2 keV. If the energy splitting would be observable the characteristic radiation patterns between m_i and m_f states would be seen. As only the mixture of the states is observed the usual assumption is that the substates are equally populated. The general form of the angular distribution (W(θ)) is then

$$W(\theta) = \sum_{m_i} p(m_i) W_{m_i \to m_f}(\theta) \tag{2.46}$$

where $p(m_i)$ is the relative population of the m_i state. If the m-substate populations are equal $W(\theta) \propto constant$. By observing the preceding γ-ray we can set the reference angle to zero. Now $p(0) = 0$ and resulting $W(\theta) \propto 1 + cos(\theta)^2$ where θ is the angle between γ_1 and γ_2. In general the angular correlation has the form

$$W(\theta) = 1 + \sum_{k=1}^{L} a_{2k} cos(\theta)^{2k}. \tag{2.47}$$

The value of the parameter a_{2k} depends on the mixing ratio δ, I_i and I_f and are tabulated in Refs [48, 49, 50]. Tabulated values are given for the Lagrange polynomial of the form

$$W(\theta) = 1 + A2 \cdot P_2(cos(\theta)) + A4 \cdot P_4(cos(\theta)), \tag{2.48}$$

where P_2 and P_4 are the second and fourth order Lagrange polynomials. The electron-γ coincidences also exhibit angular dependencies and devices relying on this feature have been used to probe the nuclear properties. See for example Ref. [51]. In principle, when measuring electron-γ coincidences the angular correlation effects should be taken into account. However, in the present work the effects of electron-γ angular correlation are neglected as they should not have a significant effect on the results obtained.

2.4 Detection limits

In some cases the detected number of counts in a peak is very small and cannot be reliably distinguished from background. In such cases an estimation of the expected peak intensity can be given by the minimum detectable activity (MDA), formulated by Currie [52]. The MDA value depends on a critical level L_c given by the equation

$$L_c = k\left(\frac{R_b}{T_s} + \frac{R_b}{T_b}\right)^{1/2} \xrightarrow{T_s=T_b} k\left(\frac{2R_b}{t}\right)^{1/2}, \tag{2.49}$$

where R_b is the background count rate, T_b is the background counting time and T_s sample counting time. k is the number of standard deviations above the mean expected net count rate of zero when no activity is present at which the critical level is specified to lie. If the background is determined from the same measurement T_b=T_s=t. The critical level represents the net count rate that confirms the presence of the activity. Assuming same probabilities for false positive and false negative detection the low limit of detection L_d can be given as

$$L_d = \frac{k^2}{t} + 2L_c. \tag{2.50}$$

In equation 2.50, k is usually taken to be 1.645 corresponding to a 90% confidence level and usually $k^2 \ll$t. Now equation 2.50 can be simplified to

$$L_d \approx 2L_c = 4.65\left(\frac{R_b}{t}\right)^{1/2} \tag{2.51}$$

Denoting the number of counts for low limit detection with N_d and the number of background counts with N_b equation 2.51 can be expressed as

$$N_d = 4.65(N_b)^{1/2}. \tag{2.52}$$

Finally the maximum number of counts with the given background (MDA$\times$t) is N_d/ϵ where epsilon is the corresponding detection efficiency. The detection limits are used in the ^{154}Sm and ^{194}Po analyses (sections 4.1 and 4.4) when the peak areas cannot be fitted or integrated.

Chapter 3

Experimental apparatus and techniques

This chapter introduces the development of new methods related to the analysis and interpretation of the data collected with the SAGE spectrometer along with a description of the device itself. The first section (section 3.1) gives an overview of the newly developed SAGE spectrometer followed by short presentations of the surrounding infrastructure (sections 3.2 to 3.4). The individual components of SAGE are then introduced and discussed in sections 3.5 to 3.7. In the experimental apparatus section (sections 3.8 and 3.9) a number of methods and processes related to experiments with SAGE are introduced. Related to the development of SAGE, section 3.10 deals with possible origins of electron background and section 3.11 discusses the alignment of the electron distribution on the detector in order to maximize the total electron count rates. The radial filtering (section 3.12) and add-back algorithms (section 3.14) are tools to improve the overall quality of the data. The time gate selection method (section 3.16) introduces a systematic method to select the correct time gate for coincidence counting. The Doppler correction (section 3.13) and the dead layer definition (section 3.15) are used to find the correct energy for γ-rays, electrons and heavy ions measured with the SAGE spectrometer.

3.1 A general description of SAGE

As in-beam nuclear spectroscopic studies have been conducted in heavier and heavier elements a clear challenge has arisen. The strong dependence of the internal conversion coefficients on atomic number Z (see equations 2.24 and 2.25)

means that the spectroscopic information measured via γ-ray spectroscopy starts to grow more sparse as information is lost with the undetected conversion electrons. An example of the dependence of the ICC on Z is given in figure 3.1. Especially in heavy deformed nuclei the lowest lying 2^+ to 0^+ transitions have proven to be difficult to measure as the energy of these transitions is below 100 keV, resulting in very high conversion coefficients (see for example Ref. [53]). In order to enable measurement of highly converted transitions

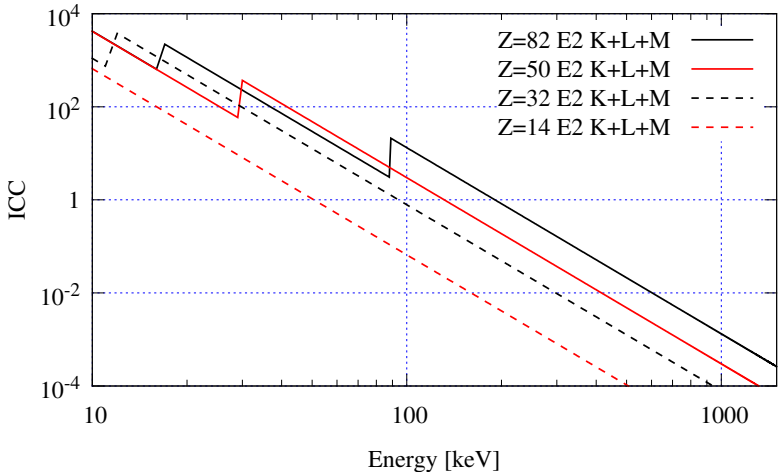

Figure 3.1: Evolution of total ICC for an E2 type transition for group 14 metals.

an electron spectrometer has been coupled with the JUROGAMII germanium detector array [54]. This system allows simultaneous detection of γ-rays and internal conversion electrons, and the combination is known by the acronym SAGE - *S*ilicon *A*nd *GE*rmanium [55, 56]. The main components of the system are shown in figure 3.2. The operational principle is that the beam from the K130 cyclotron [57] first passes next to the electron detector and goes through the main and upstream coils into the target chamber. Photon radiation generated by interaction of the beam with the target is detected by JUROGAMII (section 3.2) and electrons are transported upstream along helical paths with the aid of solenoidal magnets (section 3.5.1). A high voltage (HV) barrier filters low energy electron background (section 3.5.6) and a segmented Si detector is used to observe the electrons (section 3.5.3). If the experiment requires more sophisticated measurement methods SAGE is used in conjunction with the gas filled recoil separator RITU (section 3.3) and the focal plane spectrometer GREAT (section 3.4), in order that various tagging methods can be used.

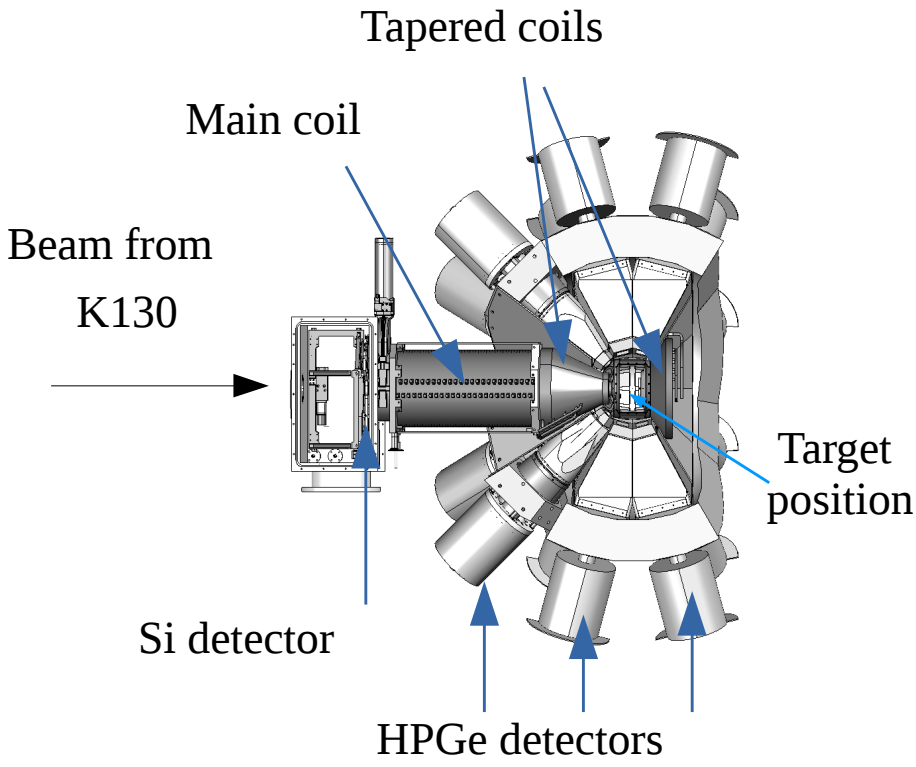

Figure 3.2: A schematic image of the SAGE spectrometer viewed from the side. The individual components are introduced in detail in the text.

3.2 The JUROGAMII germanium array

The JUROGAMII array consists of 15 Phase 1 [58] or GASP [59] detectors and 24 Clover [60] detectors arranged in 4 rings. The rings are at angles of 75.5°, 104.5°, 133.6° and 157.6° compared to the primary beam vector. The first two rings (75.5° and 104.5°) are instrumented with Clover detectors and the other two with GASP/Phase 1 detectors. In the SAGE configuration, 5 of the Phase 1 detectors at backward angles (157.6°) are removed in order to accommodate the magnetic coils. The general structure of the array is shown in figure 3.3. All of the detectors are surrounded with bismuth germanate (BGO) shields allowing Compton suppression and the front faces of the detectors are covered with X-ray absorbers made of sheets of tin (0.1 mm) and copper (0.5 mm). The absolute photo peak efficiency in the SAGE configuration measured with

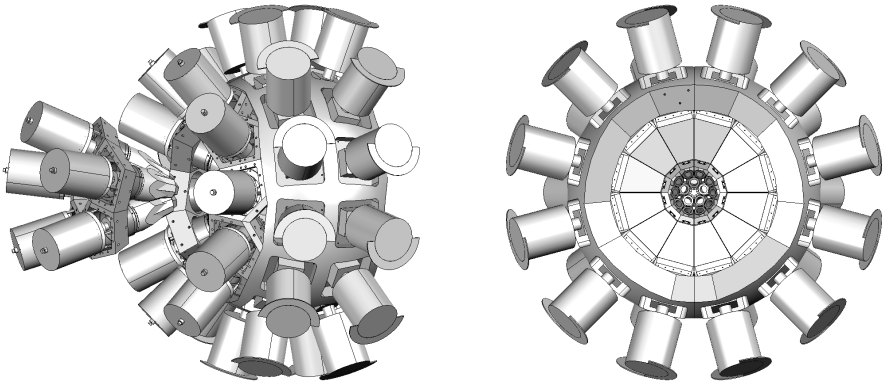

Figure 3.3: The JUROGAMII array of Compton suppressed germanium detectors. Left: A view from the side with the backward ring (157°) Phase 1 detectors pulled back. Right: A view from the downstream/RITU side.

^{133}Ba and ^{152}Eu sources is shown in figure 3.4. Note that the labels beginning with S refer to experiment identification numbers used in JYFL.

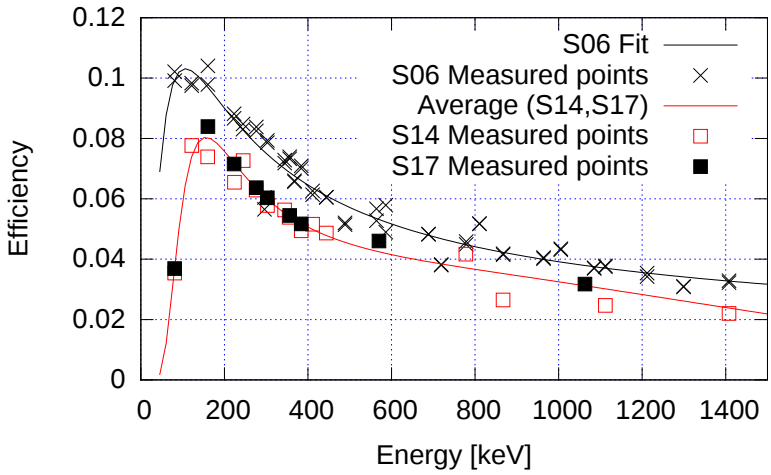

Figure 3.4: Absolute JUROGAMII efficiency with X-ray absorbers (S14, S17) and absorbers removed (S06). A typical measurement error is 2%.

3.3 RITU - Recoil Ion Transport Unit

The gas-filled recoil separator RITU [61, 62] is used to separate fusion products from the primary beam and to focus ions formed in fusion-evaporation reactions on the focal plane. RITU has three quadrupole magnets that are used for focusing and one dipole magnet used to separate ions according to their magnetic rigidity arranged in a QDQQ configuration starting from the target. RITU is filled with helium meaning that in typical cases the pressure within the volume from the target chamber to the focal plane is between 0.1 and 1 mbar. Charge-exchange reactions of the ions with the He filling gas results in the ions following a trajectories according to the average charge state in the gas. This results in a higher transmission when compared to vacuum-mode devices. A schematic view of RITU is shown in figure 3.5.

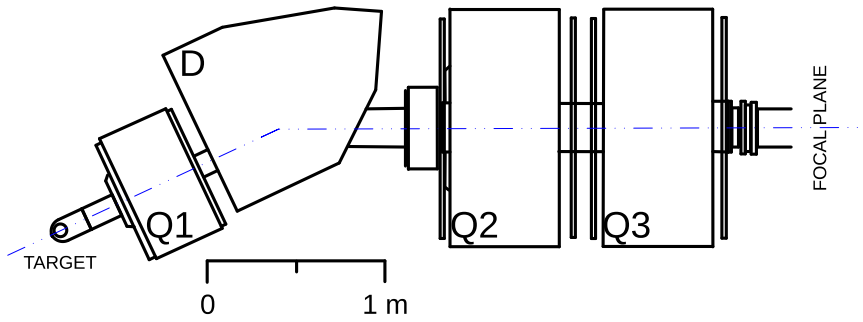

Figure 3.5: An overview of the RITU magnetic configuration.

3.4 The GREAT spectrometer

After RITU separates and focuses the ions of interest to the focal plane the GREAT (Gamma-Recoil-Electron-Alpha-Timing) spectrometer [63] is used to study the kinematics and decay of the recoils. A schematic representation of the GREAT spectrometer is shown in figure 3.6. The multi-wire-proportional counter (MWPC) is used to record recoil energy loss. Recoils are implanted into two double-sided-silicon-strip detectors (DSSDs) mounted side-by-side that record the position of the implanted recoil and the energy, position and time of all decay events. The dimensions of the DSSDs is 60×40mm with 1mm pitch and thickness 300μm. There are 60 strips in the horizontal (x-) direction and 40 in the vertical (y-) direction with the y-strips facing the beam. The time difference between events recorded in the MWPC and the DSSD gives

time-of-flight (ToF) information which is, together with energy loss information (ΔE) from the MWPC, used to identify components of the transported beam. An example of a ToF-ΔE matrix is shown in figure 3.7. As the implanted ions decay, silicon pin detectors arranged in a box geometry around the DSSD are used to detect escaped alpha particles and electrons. Planar and Clover germanium detectors are used to measure γ rays emitted during the decay process.

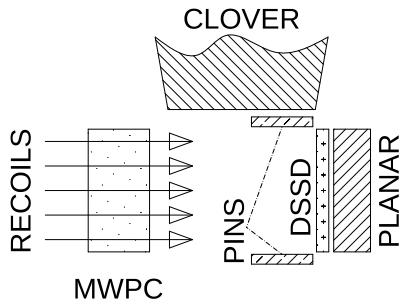

Figure 3.6: A schematic representation of the GREAT spectrometer, viewed from the side.

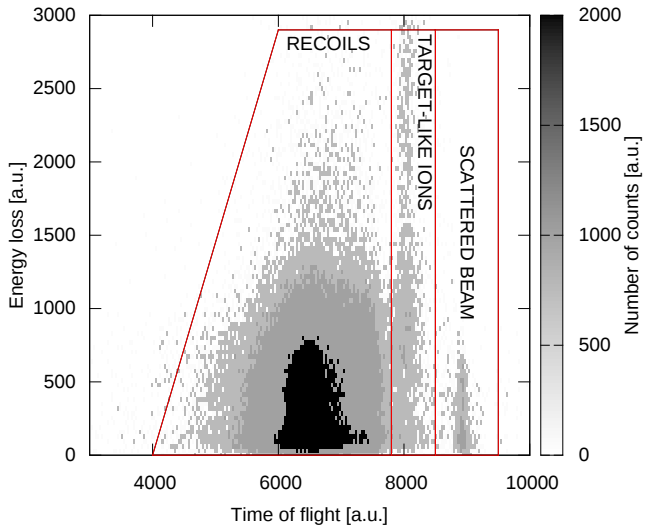

Figure 3.7: An example of a ToF-ΔE matrix taken from the reaction ^{28}Si+^{170}Yb used to study ^{194}Po (section 4.4). Note that for visualization purposes only a fraction of the data is used.

3.5 Components of the SAGE spectrometer

3.5.1 Generation of the magnetic field

In the early stages of the SAGE project the use of permanent magnets for electron transport was considered. This idea was soon rejected and more traditional although uncommonly shaped electromagnetic solenoids were chosen based on extensive simulations. A set of three magnets (shown in figure 3.8) is used to generate the magnetic field needed to transport electrons from the target position to the Si detector. Two of the magnets are tapered in order to fit within JUROGAMII and to retain the highest possible γ-ray detection efficiency. The main coil and upstream tapered coil are tilted at an angle of 3.2° to the primary beam axis so that the magnetic axis and primary beam axis meet at the target position but the heavy ion beam does not need to pass through the centre of the Si detector. The solenoid magnets are connected in series and one power source with a maximum power of 100 kW (100 V, 1000 A) is used to feed the current through the magnets.

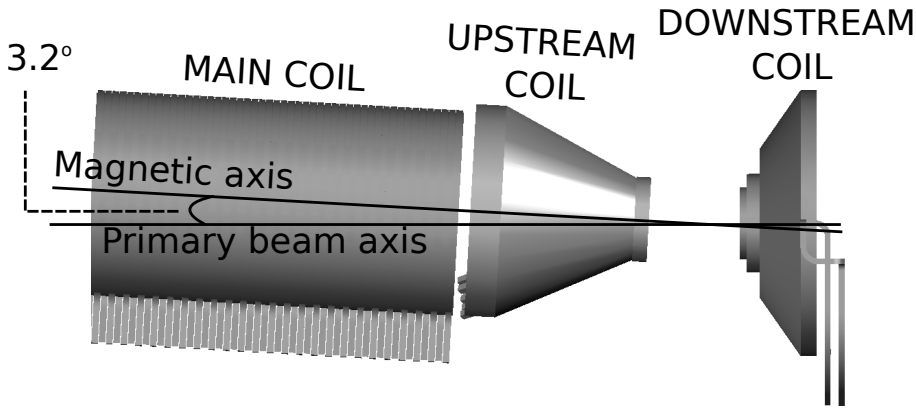

Figure 3.8: The electromagnetic coils of SAGE as viewed from above. The main coil along with the upstream coil are tilted at an angle of 3.2° with respect to the primary beam axis.

Measured and simulated axial magnetic fields generated by the magnets, with a current through the coils of 700 A, are shown in figure 3.9. Simulated values

are calculated with OPERA 3D [64] and RADIA [65] software packages. The magnetic pocket created by the gap for the target chamber is clear, and another minimum is created by the support structures. Note that the target position is not located at the magnetic minimum. The magnetic field (B) inside a long solenoidal magnet can be calculated with the equation

$$B = \mu_0 \frac{N}{L} I, \tag{3.1}$$

where μ_0 is the magnetic constant ($4\pi \times 10^{-7}$ [N/A^2]), N the number of loops in the solenoid, L the length of the solenoid and I the current through one loop in amperes. The main coil has 5×50 loops and length of 0.5 m, with 700 A current this yields a magnetic field strength of 0.44 T that is only slightly stronger than the corresponding measured value shown in figure 3.9.

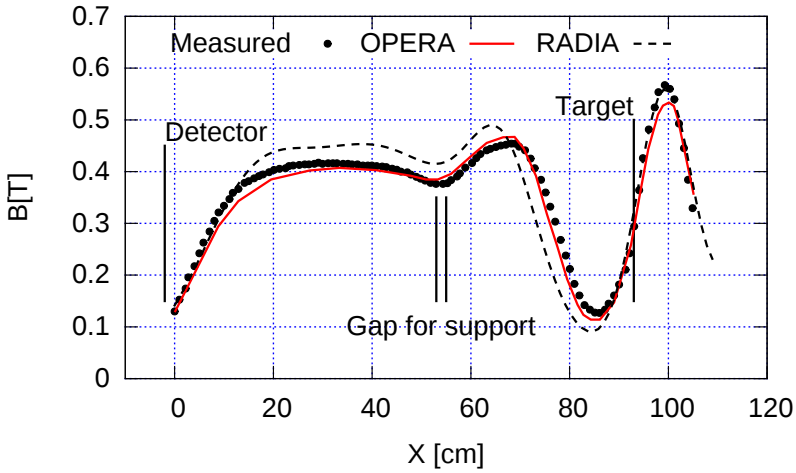

Figure 3.9: Axial magnetic field profile with 700 A current, measured with an AlphaLabs Inc. M1ST gaussmeter. Simulated values with OPERA 3D [64] and RADIA [65] software packages. Errors of the measured points are roughly ±1 cm for the position and ±0.01 T in the measured magnetic field.

Cooling of the SAGE magnetic coils

The SAGE magnetic coils are water cooled, with water flowing at the rate of 70 l/min, through the conductors via an 5 or 6 mm diameter circular cavity. In normal running conditions with a coil current of 800 A the coil temperatures are below 40°C. With the maximum design current of 1000 A the temperature of the innermost loop of the downstream tapered coil rises to close to the 50°C that is considered the upper limit for the epoxy coating. A thermal image

showing the temperatures of the coils and conductors with 600 A current is shown in figure 3.10.

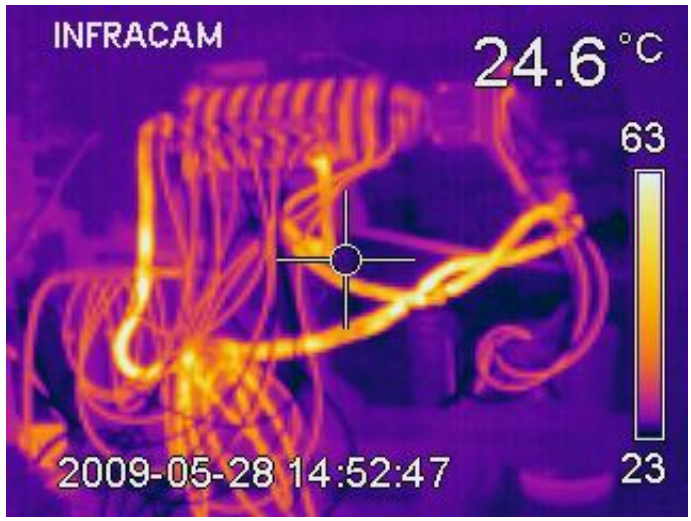

Figure 3.10: Thermal image of SAGE with 600 A of current applied on the coils. The hottest parts are the current carrying cables, at a temperature of approximately 60°C. The current carrying cables shown in this image were later changed to thicker ones lowering the cable temperatures close to 30°C.

3.5.2 Magnetic shielding

During experiments when JUROGAMII is closed the tapered coils lie very close to the bismuth germanate (BGO) shields around the Phase 1 detectors. The photomultipliers (PMTs) in the BGO shields and to a lesser extent the Phase 1 detectors are sensitive to magnetic fields. The measured response of one of the BGO shields with the original 4 mm shield plates is shown in figure 3.11 with and without the SAGE magnetic field. The general behaviour of the PMT signal as a function of stray magnetic field is shown in figure 3.12. Note that usually the photomultiplier is set to give a 1 V/MeV signal. In order to reduce the effect of the stray field, additional shielding was constructed around the coils. The original design of the magnetic shields is shown in figure 3.13.

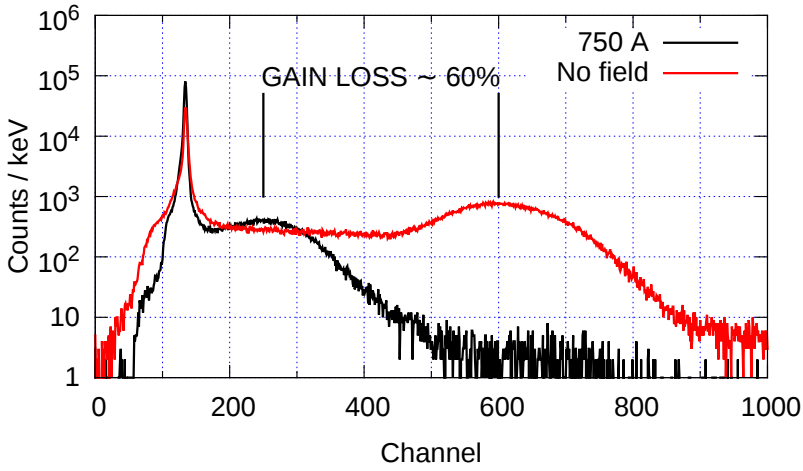

Figure 3.11: Spectrum from BGO shield in stray magnetic field.

After the shielding was mounted the closest of the BGO photomultiplier tubes (PMTs) was still affected by the magnetic field but in a recoverable manner. The loss of amplification could be corrected with tuning the signal threshold in such a way that the peak-to-total ratio of the HPGe detector installed in conjunction with the BGO shield in question showed no effect when measured with a ^{60}Co source.

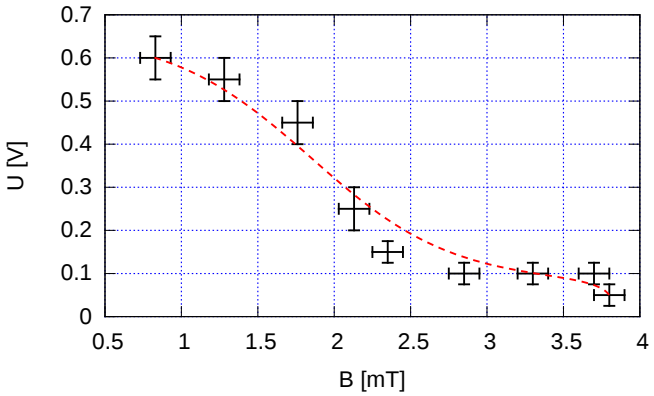

Figure 3.12: Signal from Phase 1 BGO shield photomultiplier tube as a function of stray magnetic field. The signal is generated with the 662 keV γ-rays from a ^{137}Cs source and measured with an oscilloscope. The line through the points is to guide the eye.

In the original design all the magnetic shield components were made from 4 mm thick soft iron plates. The tapered sections are attached to the JUROGAMII frame and split open with the frame. The octagonal part was designed to envelop the main coil. The main coil shield was later modified so that the lowest plate remained as a part of the support structure while the remainder were stacked on top of the coil. This modification was made in order to guide the electron distribution to the center of the detector (see section 3.11.2). In addition the tapered plates over Phase 1 detectors are layered with two 0.5 mm layers of sheet metal in order to protect the BGO shields and Phase 1 detectors. It has been noted that some of the Phase 1 detectors that are equipped with Canberra made pre-amplifiers are sensitive to the magnetic field, causing bias shutdown when the magnetic field is applied. The effect of the magnetic shielding on the magnetic field itself is not fully measured as it is very difficult to access the relevant parts of the device when it is fully assembled. Effect at the magnetic minimum (x∼86 cm in figure 3.9) near target position is known. The measured axial field drops from 0.13 T to 0.12 T when the magnetic shields are fully applied.

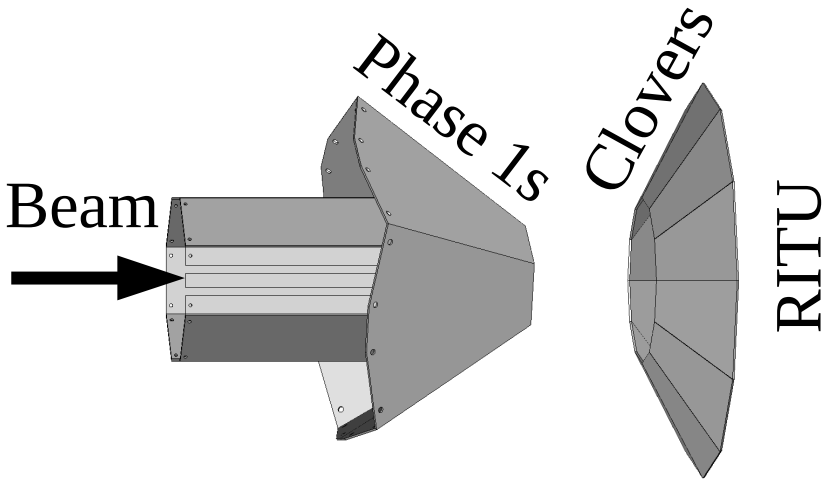

Figure 3.13: Magnetic shielding plates in the original design configuration.

3.5.3 The SAGE silicon detector

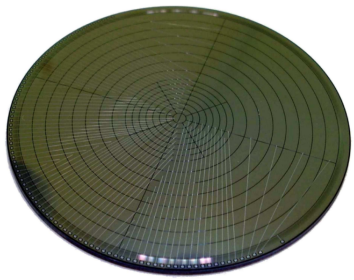

Figure 3.14: A photograph of the detector. The signal strip wires and the detector segmentation are clearly visible. Figure is taken from Ref [66].

The Si detector used to observe internal conversion electrons in SAGE is shown in figure 3.14. The detector is divided into 90 individual segments in order to obtain a more even distribution of count rates over the segments. A more detailed view of the segmentation and size of the detector is shown in figure 3.15. Detector is located at distance of 96 cm from target resulting solid angle of ∼1.3 msr. The detector is 1 mm thick with metallization on both sides. Bias for the detector is fed through the rear side and the signals are carried from the segments with strip wires running on the surface of the detector. According to the manufacturer of the detector (Micron semiconductor LTD) the full depletion (FD) voltage is 150 V and the typical total leakage current is 1 μA. The detector is mounted on a printed circuit board (PCB) that is shown in figure 3.16. The measured detector drain current as a function of bias voltage is shown in figure 3.17. The measurement was performed with the final bias feed through configuration (see figure 3.18) and was limited to 100 V due to concerns with the bias source. For the same reason a bias voltage of 90 V is typically used during experiments. As can be seen from figure 3.17 90 V lies on the I-V curve plateau but the shape of the I-V curve with lower temperatures indicates that a higher bias voltage could be used.

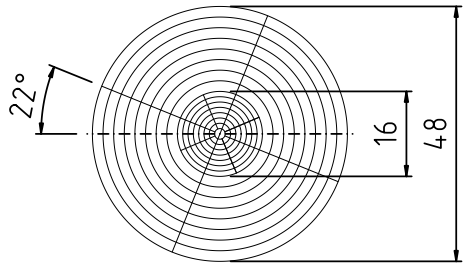

Figure 3.15: The segmentation and dimensions of the SAGE Si detector as seen from the target. The quoted dimensions have units of mm and degrees. The tilt of the detector is a design feature to shorten the signal wires.

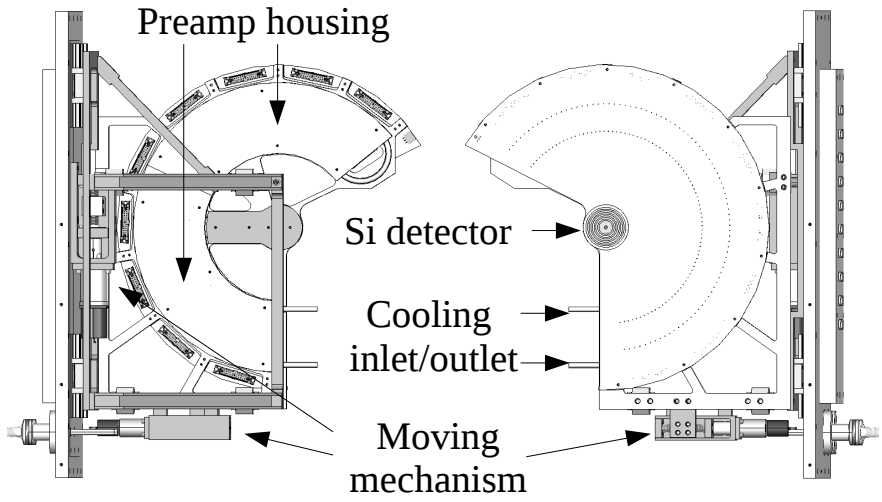

Figure 3.16: The PCB and detector mounting mechanism. Left image is from behind, right in front.

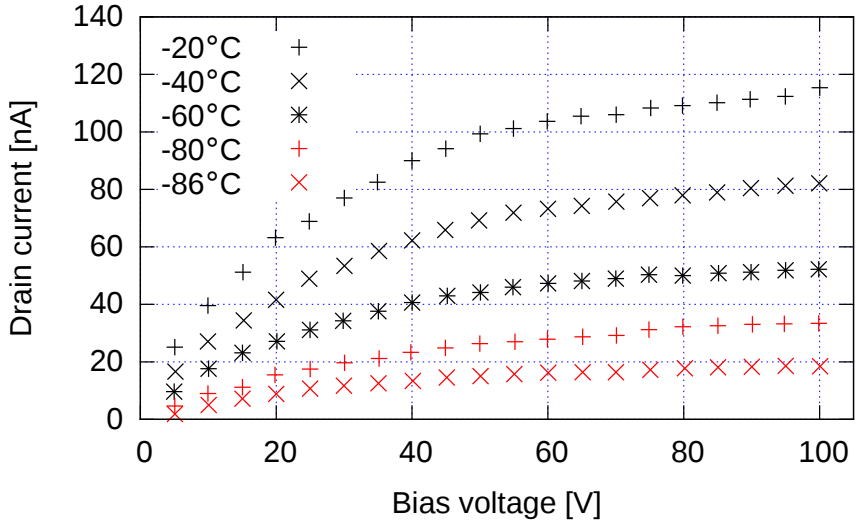

Figure 3.17: Detector drain current as a function of bias voltage. Error in the temperature is in order of ±1°C, in voltage ±1 V and in current ±2%. The lowest reliably achievable cooling temperature during experiments is -80°C resulting to a detector temperature approximately -25°C.

Originally the PCB housing, the detector and pre-amplifiers were mounted on a movable structure allowing ±5mm movement in the detector plane direction. The moving mechanism was disabled as the original cooling circuit pipes were not rated to temperatures the new cooling unit (JULABO FP89-ME) achieves [67]. The new cooling circuit is made from rigid copper pipes. The PCB houses 90 equidistantly placed CAEN A1422 preamplifiers with a gain of 400mV/MeV and the power filtering circuits for each segment. The signal path from individual segments to the pre-amplifier is made as short as reasonably possible. Bias to the detector was originally fed through a 10 MΩ bias resistor but this was later changed to 100 kΩ along with addition of a 22 MΩ ground resistor. The difference between the biasing schemes is shown in figure 3.18.

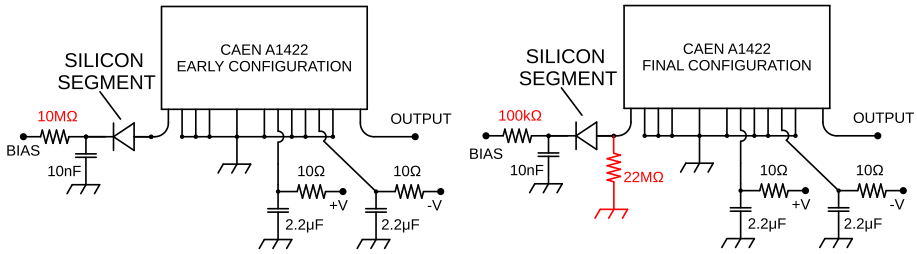

Figure 3.18: The different biasing schemes of the SAGE detector. The differences are highlighted in red (lighter colour).

From the PCB the signal is carried out from the vacuum chamber to a custom built gain-and-offset box (GO-box), that provides a gain factor ×1 or ×2 and DC offset. The GO-box output also provides impedance matching to the input of the LYRTECH/NUTAQ ADC (50 Ω). The acceptable input to the LYRTECH/NUTAQ analogue to digital converters (ADC) is ±1.1V.

3.5.4 Electronics and data acquisition system

The Total Data Readout (TDR) [68] acquisition system is used to collect experimental data. At the time of the measurements in this work the system was divided into two main sections, a "digital side", incorporating the JUROGAMII and SAGE Si-detector channels, and the "analogue" side with channels from the focal plane. On the digital side the signals from the GO-boxes are fed to 14-bit 16-channel LYRTECH/NUTAQ VHS-ADC digitiser cards. The amplitude of the signal is extracted in the digitiser cards with the aid of the Moving Window Deconvolution [69] (MWD) algorithm. The signal amplitudes determined are timestamped with 10 ns resolution based on a digital CFD with a clock signal from a 100 MHz metronome unit.

On the analogue side the signals are fed to VXI ADC cards via shaping amplifiers. Timing information and individual ADC triggers are generated in parallel with a conventional TFA and CFD chain. The timing information is also used to detect pile-up events. If a second event happens within a set time window events are marked and can be rejected later during the signal processing. From the ADC cards the data is passed to a VME collator that time-orders the data from the VXI ADC cards and further to a PC-based merge system that collects the data, from both the analogue and digital side, together. The merge time-orders the data from the streams before passing it to a filter program that can be set to collect only the data that meets pre-set conditions. For example, in the study of ^{154}Sm only events with fold 2 (two coincident detections of γ-rays and/or electrons) or more were collected. The filter unit sends the data stream to online analysis computers and to data storage. A block diagram of the data acquisition system is shown in figure 3.19. In addition, a number of Time-to-Amplitude converters (TACs) are used if timing resolution below 10 ns is needed, for example in the MWPC-DSSD ToF. These are not shown in the block diagram. Most of the data analysis shown in this work was performed with the GRAIN software package [70] that is also used for online sorting on the computers of the data acquisition system.

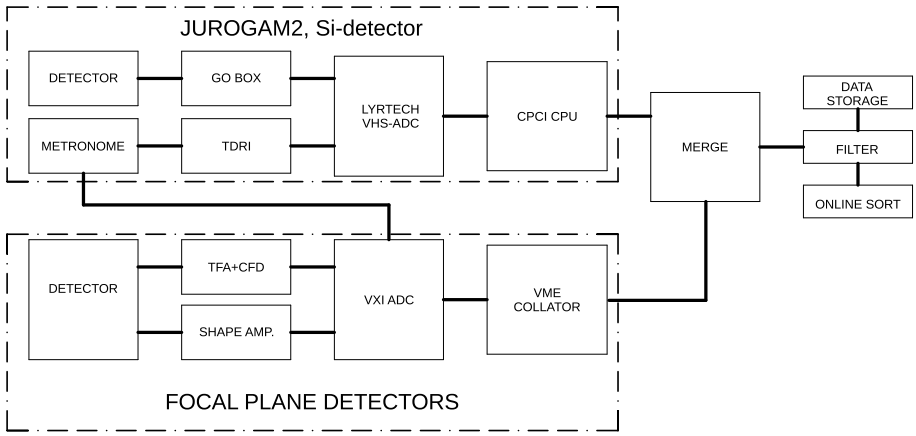

Figure 3.19: A simplified block diagram of the electronics and data acquisition system.

3.5.5 Vacuum system

The pumping scheme normally used with SAGE in conjunction with RITU is shown in figure 3.20. Due to the fragile nature of the carbon foils (C-foils) separating the helium gas filling RITU from the high voltage region, the standard procedure to pump the system down takes roughly one hour as the pump-

ing speed is initially limited to 1 mbar/s. Experience has shown that higher pumping speed can result in failure of the carbon foils.

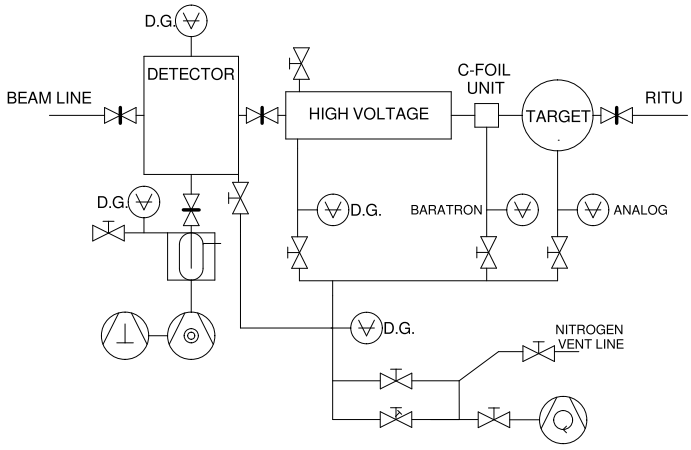

Figure 3.20: The standard pumping scheme with RITU.

The carbon foil unit used to separate the high voltage and target chamber volumes is shown in figure 3.21. The $50\mu g/cm^2$ carbon foils glued on both ends of the unit have been shown to be able to hold the HV volume at 10^{-7} mbar pressure while the target chamber is at a pressure of around 1 mbar. With certain beams the carbon foils are shown to generate γ-ray background radiation. In order to reduce the negative effects an optional pumping method was developed. The modified vacuum system is shown in figure 3.22. The main difference to the original setup is that the two-C-foil holder is replaced with two single foil units up- and downstream of the target position. In this configuration both of the foils are hidden in the beam tubes and do not have a direct line of sight to the germanium detectors. Thus the detected γ-ray background should be much lower. This moves the target from the 1 mbar helium gas to an intermediate pressure (10^{-2} mbar) volume when used with RITU. The helium gas is known to cool the target allowing more intense beam in some cases, but based on the target cooling model introduced by Antalic [71] this drop in pressure is not critical.

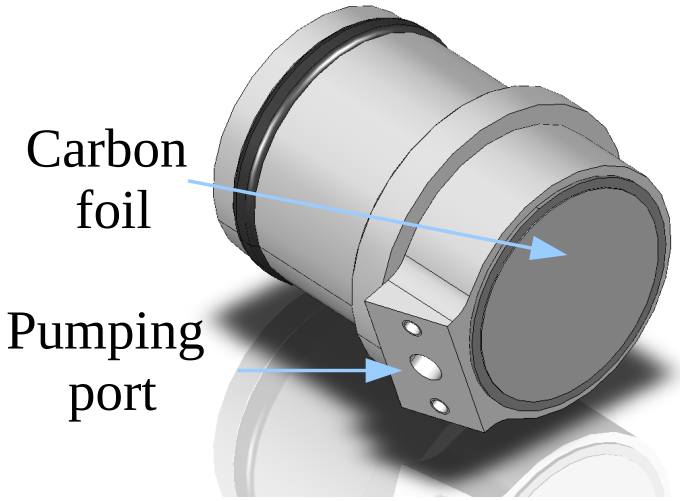

Figure 3.21: The carbon foil unit. Thin, $50\mu g/cm^2$ carbon foils are glued on both ends of the unit.

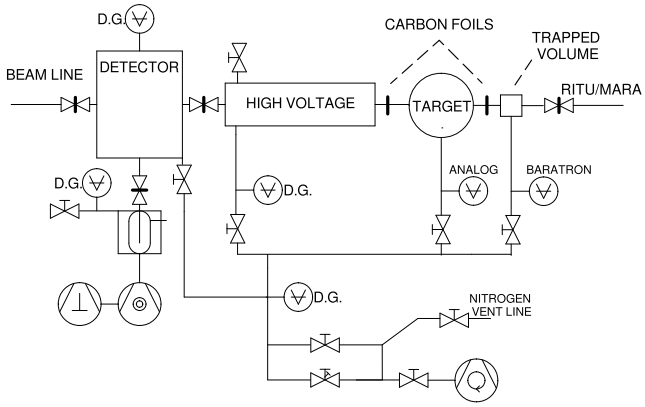

Figure 3.22: Optional pumping scheme.

The optional pumping system requires a new part (shown in figure 3.23) that allows venting/pumping of the volume between downstream carbon foil and the RITU gate valve. The dimensions of the part are such that the RITU acceptance is not limited. Pumping and venting through the capillary pipes must be done with care. Normally SAGE can be pumped at a rate of 1 mbar per second, but the thin capillary pipes limit the pumping/venting speed to 0.3 mbar per second.

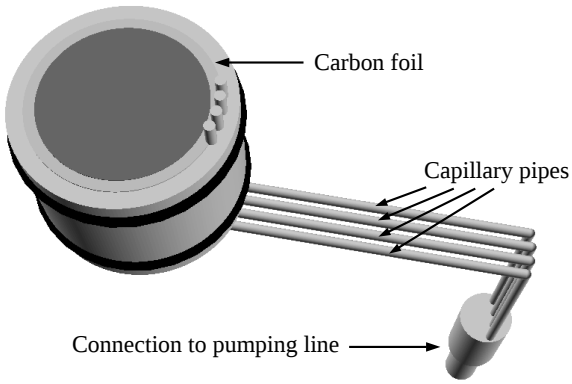

Figure 3.23: Adapter part allowing venting of the volume between downstream carbon foil and RITU gate valve.

3.5.6 High voltage barrier technical details

The high voltage barrier designed to repel low energy δ electrons is shown in figure 3.24. A cut through the longitudinal axis with dimensions is shown in figure 3.25. The aluminium sleeve protects the NORYL insulator from wear and tear. High voltage is fed to the inner core from a high voltage source through a resistor chain (total 5 $G\Omega$) and the connection to the inner core is made via a horse shoe connector as shown in figure 3.26. Effectively the HV circuitry can be described with a RC-circuit as shown in figure 3.27.

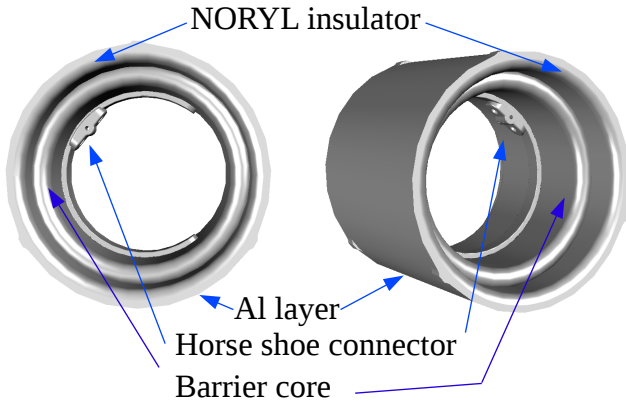

Figure 3.24: The main parts of the HV barrier showing the outermost Al layer, the NORYL insulation and the barrier core. The outermost aluminium layer protects the NORYL insulator from physical harm and the small bulges on the outer layer prevent forming of trapped volumes.

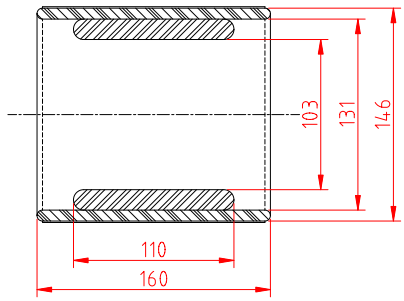

Figure 3.25: A cross-sectional diagram of the HV barrier. Dimensions are in millimetres.

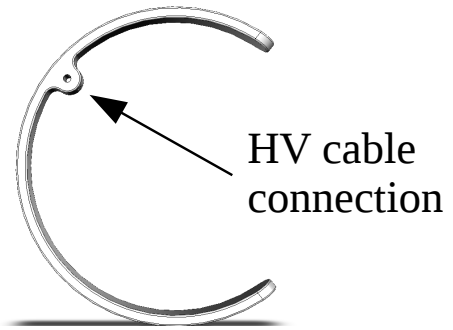

Figure 3.26: Rendering of the horse shoe connector.

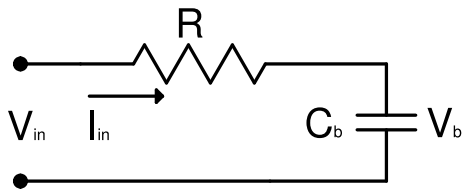

Figure 3.27: Simplified circuit diagram of the HV barrier.

(a) The HV barrier installed as originally planned.

(b) The HV barrier with a cable guide.

Figure 3.28: The HV barrier positioning.

The high voltage source (Glassman EH50N2 [72]) has an internal monitor for the feed voltage (V_{in}) and drain current (I_{in}). The barrier capacitance

($C_{b,meas}$) was measured to be approximately 8 pF when installed in SAGE. Figure 3.28a shows the original high voltage barrier position along with the cable path. In the early experiments the cable was damaged either by ion beam or by discharge through the insulating sleeve. In order to ensure that the cable will not interfere with the beam, the cable guide shown in figure 3.28b was added. The calculated value for the capacitance $C_{b,calc}$ using an open ended cylindrical geometry is 73.47 pF. The leakage current (I_{in}) is very low and just at the limit of the internal measurement system of the HV source. The measured leakage current behaviour for both the original and the new barrier is shown in figure 3.29. The leakage current values below -20 kV are below the measurement threshold of the system and ignored in the fit. The drain current

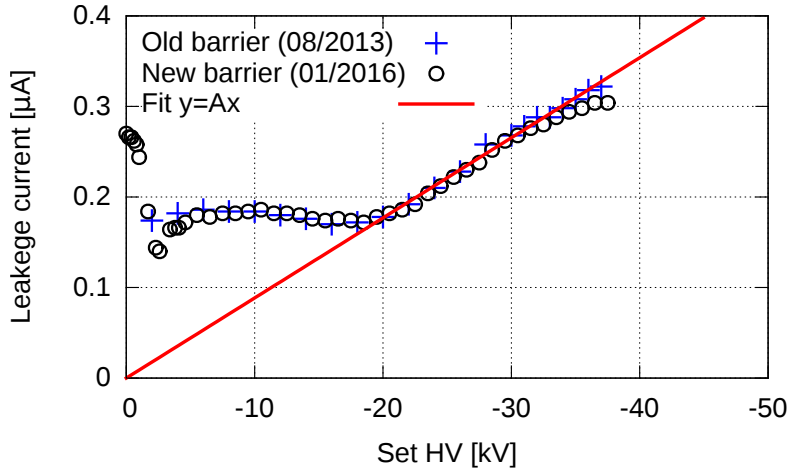

Figure 3.29: HV barrier leakage (I_{in}) current as a function of set high voltage (V_{in}). Fit parameter A=-8.95×10^{-12} when the set high voltage is in volts and I_{in} in amps. Errors in voltage are in order of ± 1 kV and in drain current ±2%.

leads to resistive losses in the resistor chain. The voltage over the RC circuit is governed by the function

$$V_{in} = V_R + V_b = I_{in}R + \frac{Q_b}{C_b}. \tag{3.2}$$

V_R is the resistive voltage drop, V_b is the common voltage over capacitances and Q_b is the collected charge. Therefore with a typical HV barrier setting of -30 kV the resistive drop in the effective barrier voltage V_b is 500 V. The original HV barrier survived roughly 15 week long experiments before succumbing to scarring from excessive sparking. The damage caused by sparking is shown in figure 3.30. The carbon residue deposited on the Noryl part is extremely

difficult to remove and and it is likely the original barrier needs to be decommissioned or rebuilt with a new NORYL part.

Figure 3.30: The downstream edge of the original HV barrier showing damage from excessive sparking.

3.6 Calculation of the effective HV barrier height

The effect the HV barrier on incident electrons has been a topic of several non-conclusive discussions. Here the effective barrier height is calculated in order to shed light on the observations by means of calculations based on fundamental physical principles. Simulations addressing this same topic are presented in Refs [**?**, 86].

3.6.1 Reference case - Point charge

The electric field generated by a point charge is known to be

$$E_{point} = \frac{kQ}{s^2}, \tag{3.3}$$

where k=$1/4\pi\varepsilon$, Q is the total charge and s is the distance between the reference point and the point charge [73]. For the future reference Q is the charge that is just able to repel an electron with energy E_e originating from distance s_{max}. Now by definition the work done by the electric field on an electron approaching directly is

$$W = \int_0^{s_{max}} qEds = E_e, \tag{3.4}$$

where q is the electric charge of the electron.

HV barrier approximation.

On the basis of superposition the SAGE HV barrier can be approximated with a charge carrying ring and when the component along the radial symmetry axis is considered, the geometry can be further reduced to a point charge located off axis. When the geometry is taken into account the electric field component along the radial symmetry axis is

$$E_{ring} = \frac{kQ}{(R^2 + s^2)} \times cos(tan^{-1}(R/s)), \tag{3.5}$$

where R is the charge offset from the radial axis that equals the average radius of the SAGE HV barrier core (58.5 mm, see fig 3.25). The geometry is shown in figure 3.31. The collected charge (Q_b) can be estimated by using equation 3.2 and HV leakage current measurement shown in figure 3.29

$$Q_b = \frac{V_{in} - I_{in}R}{C_b} = \frac{V_{in} - (-8.95 \times 10^{-12} \cdot V_{in})R}{C_{b,meas}}. \tag{3.6}$$

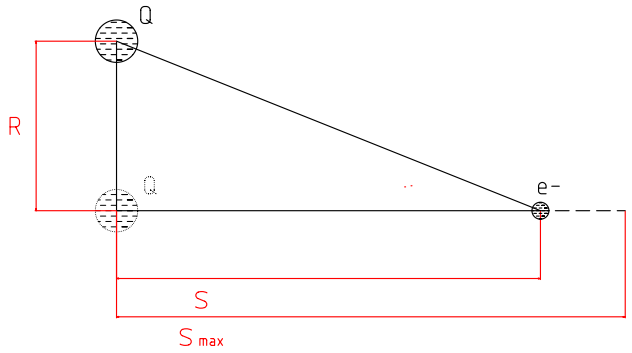

Figure 3.31: Geometry for the barrier height calculation. Reference position drawn with dots.

Here the resistance (R) is 5 GΩ and the capacitance ($C_{b,meas}$) is measured to be 8 pF. A direct comparison of the work done by the different electric fields by integrating over r is difficult due to the $1/r^2$ behaviour in the point charge case. One path to circumvent this problem is to use relative values. The ratio between field components is

$$\begin{aligned} H_{eff}(s)_{ring} &= \frac{E_{ring}}{E_{point}} \\ &= \frac{s^2}{(R^2+s^2)} \cdot cos(tan^{-1}(R/s)). \end{aligned} \tag{3.7}$$

Numeric integration over s gives the effective height of the barrier shown in figure 3.32. If the range (s) is large the effect of the geometry that is prominent when s<20 cm fades away and there would be no practical difference. However the dimensions of SAGE dictate that electrons cannot originate from "infinity". The distance between the HV barrier and the target position is approximately 0.5 m giving an effective barrier height of 0.8. Experimentally this can be approximated by "zero pass" voltages, i.e. finding the barrier voltage that blocks all the incoming electrons with a certain energy. In figure 3.33 "zero pass" voltages are approximated from electron peak areas measured with different HV barrier voltages. Efficiency and energy calibrations of SAGE are usually made using an open ^{133}Ba electron source, which has electron lines at 45, 75 and 124 keV.

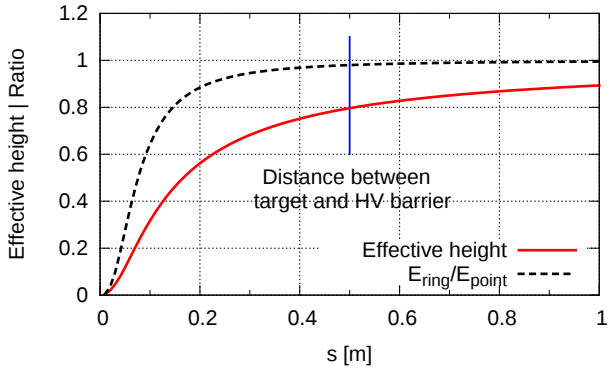

Figure 3.32: Effective height of the HV barrier and the ratio between electric fields in the direction of symmetry axis.

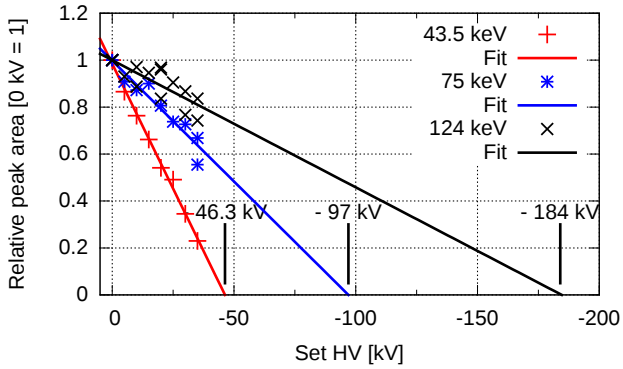

Figure 3.33: Relative transmission of conversion electrons as a function of voltage applied to the HV barrier. The "zero pass" voltages are derived from linear fits. Note that in the 45 keV case the energy losses in the source window are taken into account resulting in a electron energy of 43.5 keV. Errors in voltage are approximately ±1 kV and in relative peak area ±0.03.

The measured "zero pass" voltages yield relative barrier heights of 0.94 for the 45 keV peak, 0.77 for the 75 keV peak and 0.67 for the 124 keV peak being roughly consistent with the value 0.8 given by the ring approximation. A comparison with SACRED can be made by using data from figure 5 in Ref. [12]. The measured efficiency curve with -40 kV barrier voltage shows an endpoint close to 40 keV. This is expected as the smaller bore radius of the SACRED high voltage barrier improves the barrier performance.

3.7 Electron detection efficiency

An approximation of the SAGE electron detection efficiency curve can be deduced from the magnetic and geometrical properties of the device [74]. The performance of SAGE is compared with SACRED [12], an electron spectrometer used previously at JYFL. The maximum transmission angle can be written as

$$\theta_{trans,max} = min \begin{cases} Asin\left(\sqrt{\frac{B_t}{B_{max}}}\right) \\ \\ Asin\left(\frac{B_t R_{sol}}{2(B\rho)_E}\right) \end{cases}, \tag{3.8}$$

where B_t is the magnetic field at the target position, B_{max} the maximum magnetic field, R_{sol} the inner radius of the solenoid and $B\rho$ the magnetic rigidity of the solenoid. The inner radius of the SACRED C-foil holder (17.5 mm) and the inner radius of the SAGE carbon foil holder (15 mm) are used in place of solenoid radius, as these represent the smallest apertures through which electrons must pass to be detected. The behaviour of $\theta_{trans,max}$ for SAGE in comparison to SACRED is shown in figure 3.34. The magnetic field values for SAGE are taken from figure 3.9 with B_t being the minimum at the target area. Corresponding values for SACRED are from Ref. [12]. The measured detection

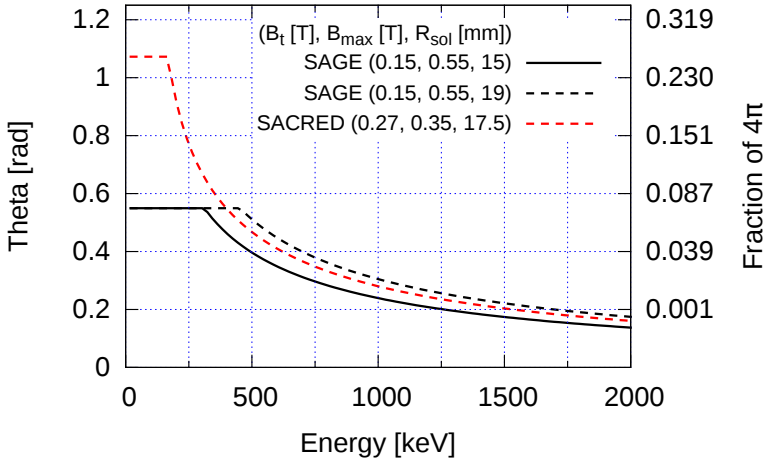

Figure 3.34: The maximum transmission angle for SAGE and SACRED as a function of electron energy. When SAGE is used without the C-foil holder R_{sol}=19mm.

efficiency values for SAGE are shown in figure 3.35 measured with ^{133}Ba and ^{207}Bi conversion electron sources. The fitted efficiency curves in figure 3.35

have the general form

$$\epsilon(E) = Exp[\sum_{i=0}^{n} a_i \times ln(\frac{E}{E_0})], \tag{3.9}$$

where a_i and E_0 are the fitted coefficients and E is the energy of the internal conversion electron. When the effect of electronics thresholds at low energies is taken into account the shape of the efficiency curve is similar to that calculated from geometrical and magnetic properties. Note that the efficiency measured during experiment S14 differs radically from the rest. The reduction in efficiency is thought to result from erroneous cabling of the coils, but the data are used later in the analysis of ^{194}Po. The relative effect of the HV barrier is

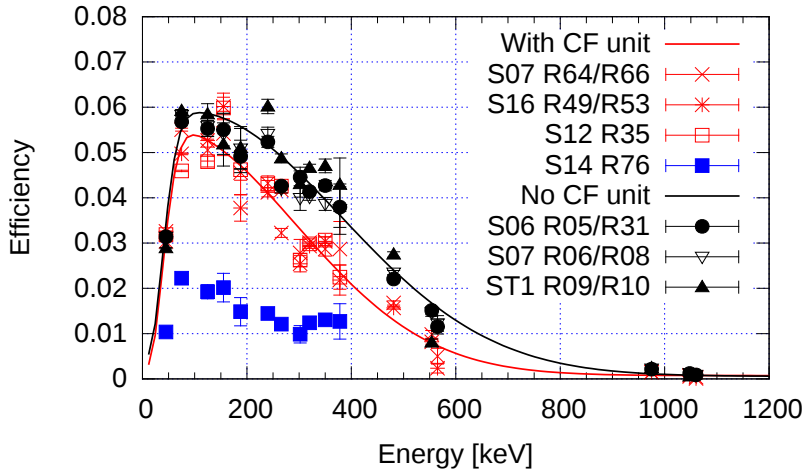

Figure 3.35: SAGE electron detection efficiency with and without the carbon foil unit (CF). No HV is applied and current through the coils is 800 A.

shown in figure 3.36 with fits having the general form

$$ratio(E,U) = 1 - Exp\left(-\frac{E - A \times U}{B^2}\right), \tag{3.10}$$

where E is the electron energy in keV, U is the set HV voltage in kV and A and B are fitted parameters.

3.8 Experimental tools

In the experiments with SAGE the main goal is to determine the excitation energies of levels in the nucleus. The level properties can be studied by exciting

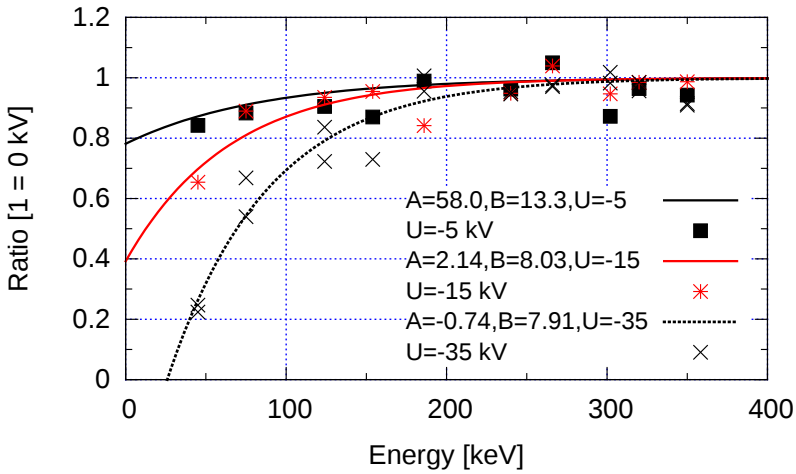

Figure 3.36: Measured SAGE electron detection efficiency with several different HV barrier voltages. Typical error in ratio is in order of ±0.02 and in energy ±2 keV.

nuclei to higher energy levels by means of nuclear reactions and studying the de-excitation to the ground state. A common method of invoking nuclear reactions is to collide two nuclei together. One of the nuclei is selected to be a stationary target, typically a thin foil of enriched material, and the other is accelerated to gain kinetic energy. The accelerated nucleus is guided to hit the target and induce a reaction. As the typical acceleration methods create a near continuous flow of accelerated particles the accelerated particle is commonly called the beam particle. The nuclear reactions employed in this work are Coulomb excitation (CoulEx) used to probe ^{154}Sm and a fusion-evaporation reaction used to study ^{194}Po. A schematic representation of Coulomb excitation and fusion evaporation reactions is shown in figure 3.37.

3.8.1 Coulomb excitation

Inelastic Coulomb scattering occurs when the beam particle passes the target nucleus close enough to cause electromagnetic interactions thus exciting one or both of the target/beam nuclei to an excited state. Excitation energy is dissipated through γ-ray emission with the most likely path being via E2 transitions in an even-even nucleus. The emitted radiation can be used to probe the low-lying excited states in even-Z, even-N nuclei and to give an estimation of the transition probabilities. Furthermore the decay process is slower than the excitation and so Coulomb excitation can be used to populate states with

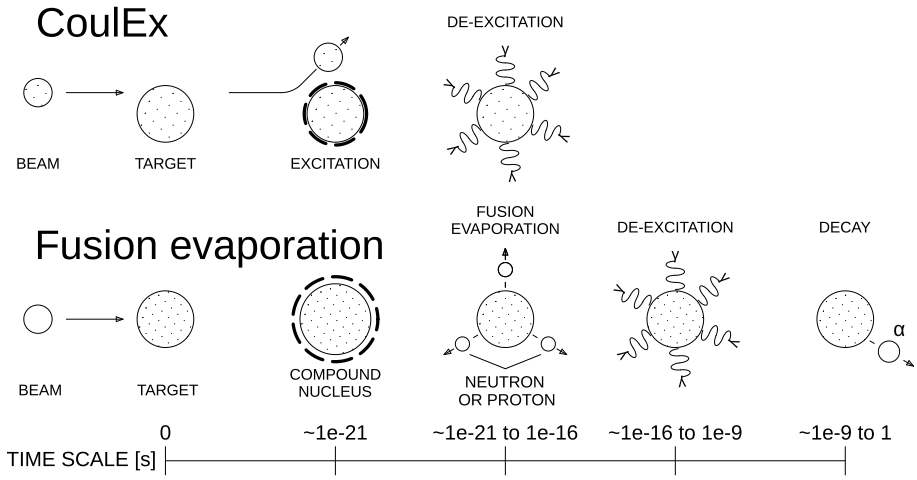

Figure 3.37: Schematic representation of Coulomb excitation and fusion evaporation reactions, used to excite nuclear levels of interest in this work.

higher excitation energy, via multiple excitation steps.

3.8.2 Coulomb excitation safe energy

As the bombardment energy increases the projectile particle penetrates deeper into the Coulomb barrier and finally with high enough energy causes direct nuclear excitation through the strong rather than electromagnetic interaction. A limit for the highest safe energy is given by Cline's "safe energy" rule [75] which states that the separation between nuclear surfaces should be greater than 5 fm. The highest safe energy in MeV can be calculated using the equation

$$E_{max} = 1.44[MeV \cdot fm]\frac{A_p + A_t}{A_t}\frac{Z_p Z_t}{1.25[fm](A_p^{1/3} + A_t^{1/3}) + 5[fm]}, \qquad (3.11)$$

where A_p, Z_p are the mass number and charge for the projectile particle respectively, $1.44 \approx e^2/(4\pi\epsilon_0)$ and A_t, Z_t mass number and charge of the target nucleus. Another way to approximate the safe energy is the Sommerfeld parameter (η) in Gaussian units given by the equation

$$\eta = \frac{Z_p Z_t e^2}{\hbar v}, \qquad (3.12)$$

where v is the relative velocity of the nuclei. In this case the reaction should fulfil the condition $\eta >> 1$ in order to be considered safe [76].

3.9 Fusion-evaporation reactions

When the projectile energy exceeds the Coulomb barrier fusion-evaporation reactions become possible. The fusion-evaporation reaction has two steps. First the projectile and target particles form a compound nucleus that can decay by emitting light particles (steps 2 and 3 in figure 3.37) such as neutrons, protons or alphas. During the fusion reaction the energy is dissipated over the whole compound nucleus and several different de-excitation paths are possible. Emission of neutrons over charged particles is generally favoured as the neutron does not have to overcome the Coulomb barrier. The evaporation process leads to distribution of fusion products with different N and Z. The nucleus of interest can be singled out by using purpose built separator devices like the gas-filled separator RITU (see details in section 3.3) and other analysis techniques such as recoil-decay tagging.

3.10 Sources of electron background

3.10.1 Target matter

In in-beam electron spectroscopy the background originates mainly from the primary beam interactions with the atomic shell electrons of the target material, creating so-called δ-electrons. Classically, the resulting δ-electrons have energies up to

$$E_\delta = 4\left(\frac{m_e}{m_b}E_k E_b\right)^{1/2} + 4\left(\frac{m_e}{m_b}E_b\right) \tag{3.13}$$

where m_e is the electron mass, E_b and m_b the energy and the mass of the bombarding particle and E_k the K binding energy of the target matter [74].

3.10.2 Other sources

Another source of electron background are electrons or positrons generated by beta-decaying nuclei. Beta-decaying nuclei can be produced as a side product in fusion evaporation reactions. Due to the reaction kinematics these reaction products can be deposited around the downstream target chamber exit of SAGE. Often the end-point energy of the beta spectrum is very high and the effect on the measured spectrum can be significant. With SAGE the target wheel blocks the majority of these events but the high energy beta particles with energy of 2.5 MeV or more can punch through the target wheel and contribute to the electron background. In addition, it is possible that background

is generated by scattered beam particles, X-rays or γ-ray photons. However, the probability to detect such events is very low due to the very small solid angle covered by the Si detector.

3.10.3 Loss processes in flight

As shown by the results from simulations in table 3.1, a significant fraction of the detected electrons have interacted with the carbon foils or the carbon foil holder. Due to the shallow incident angles between the electron trajectories and the inner surface of the carbon foil holder, forward angle scattering is favoured and the scattered electrons can pass the holder system with a high probability. According to Ref. [77] the electron backscattering coefficient with shallow angles for aluminium is 0.75 or larger and values for full energy detection in detector and number of hits in the carbon foil holder from table 3.1 indicate that the ratio between detected full energy electrons and detected scattered electrons is roughly 1. Result from further development of the GEANT4 codes[1] presented in Ref. [78] is shown in figure 3.38. The peculiar distribution of the energy losses in the inactive detector layers may contribute to the distinctive shape of the add back energy spectrum shown later in the text (section 3.14).

Table 3.1: Simulated electron energy losses in different areas in SAGE taken from Ref. [78]. A total of one million events with energy of 100 keV are simulated. Events with full energy loss within the detector are counted, any energy loss in the rest.

Volume	Number of interactions
Detector	81000
Carbon Foil Support	105000
Source	908000
Target Wheel	326000
Target Chamber	2300
Detector Chamber	0
High-Voltage Barrier	7

[1]The GEANT4 simulation is courtesy of Dr. D.M. Cox

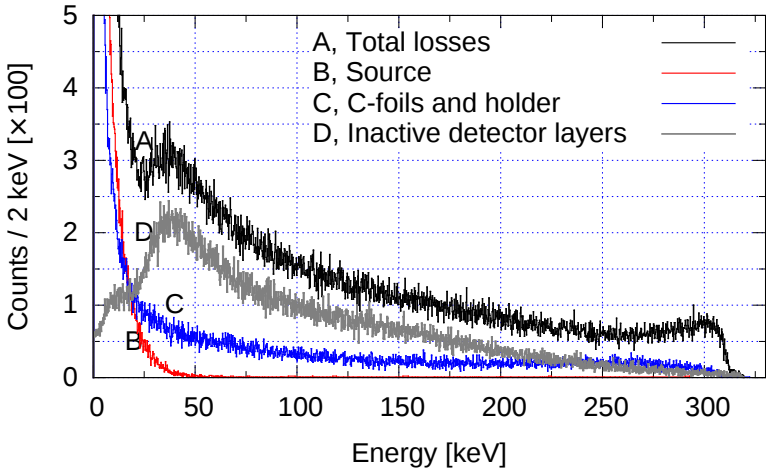

Figure 3.38: Simulated electron energy losses in various parts of SAGE. One million 320 keV electrons simulated. Roughly half of the electrons detected have left 1 keV or more energy somewhere other than in active layers of the silicon detector.

3.11 Electron distribution in Si-detector

3.11.1 Previous experience - the SACRED spectrometer

The SACRED [53, 12] electron spectrometer was built in a similar configuration to that of SAGE. A magnetic solenoidal system was used to transport electrons from the target to a Si detector and a similar HV barrier was used to filter δ-electrons. The main vacuum vessel had similar dimensions but the inner radius of the HV barrier was significantly smaller. Measurements performed with SACRED yielded an approximation for the overall count rate distribution in the detector. The general form of the electron distribution $n_e(r)$ with SACRED [66] measured during an online experiment can be approximated by the function

$$n_e(r) = \frac{a}{1 + (r/b)^3}, \tag{3.14}$$

where a,b are fitting parameters and r is the radius from the detector center point.

3.11.2 Electron distribution in SAGE

The overall normalised count rate in three different experimental cases along with a fit based on experience with SACRED is shown in figure 3.39. Note that the distribution measured with ^{133}Ba source is dominated by 45 keV conversion electrons. In the in-beam measurements (^{154}Sm Coulex, ^{160}Dy(^{32}S,xn)$^{192-n}$Pb) δ-electrons originating from atomic collisions dominate the distribution. The distribution is roughly similar to the one reported with SACRED. The shape of the general electron distribution was used to optimise the silicon detector segmentation in order to better normalise the counting rates of the individual segments. In some previous detection geometries (e.g. in SACRED), the overall performance was often limited by the count rate in a single channel.

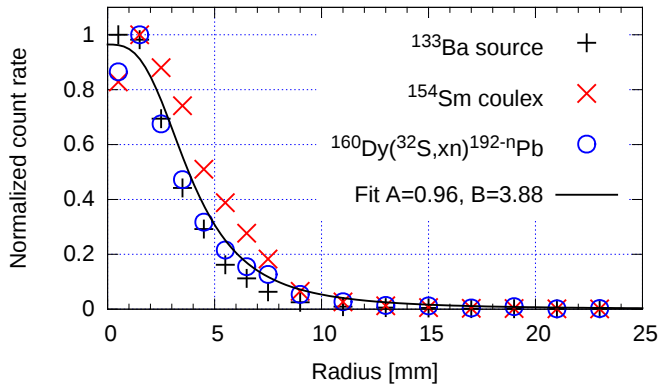

Figure 3.39: Normalised distribution of electrons in different cases with SAGE. The rate is normalised with pixel area and maximum count rate (1=max). The fit function has the same form as equation 3.14. Errors in the data points fall within the markers.

During the initial experiments the SAGE electron distribution was not properly centred. As can be seen from figure 3.41 the electron distribution was originally located roughly 6 mm down and to the left on the detector when looking from the target. The leftward shift can be explained by the offset of the main coil. According to the manufacturer the main coil center line lies 4 mm left from the planned magnetic center (offset shown in figure 3.40) line thus guiding the electrons left. The offset of the electron distribution was corrected by modifying the

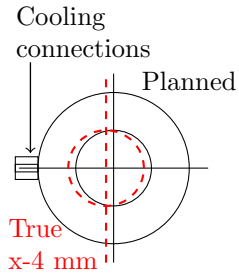

Figure 3.40: The main coil offset looking along the centre axis from the target. Not to scale.

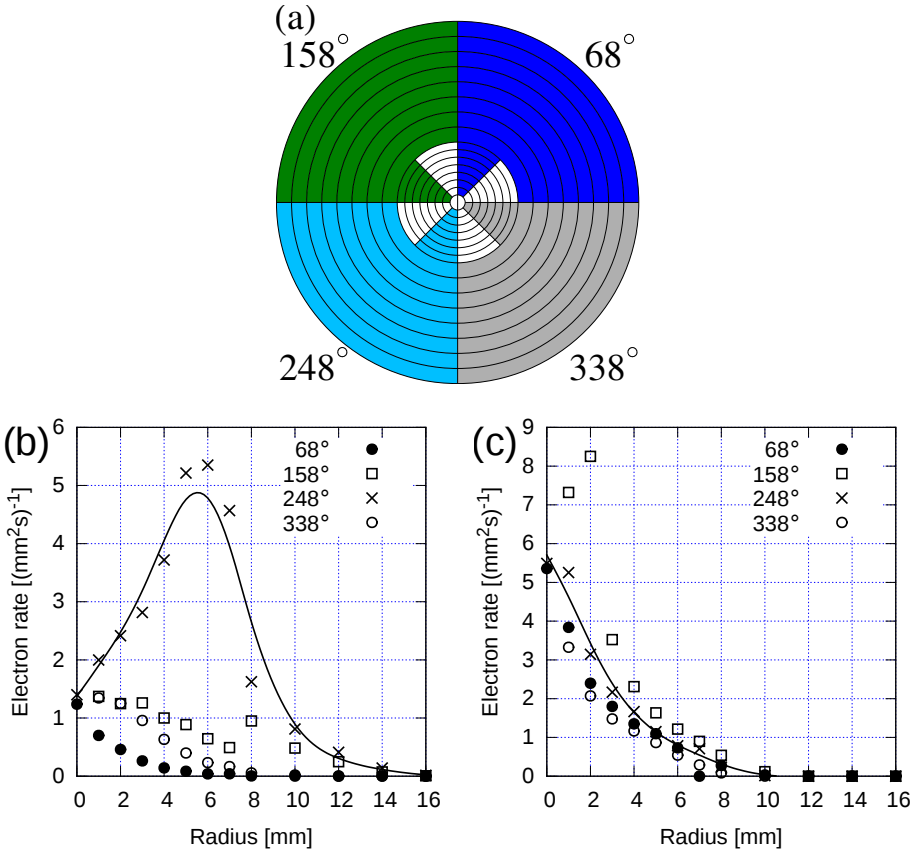

Figure 3.41: (a) Segments included in the distribution plots. The center segment belongs to both of the same hemisphere areas. Note that the detector is not rotated according to the 22° physical tilt. (b) Electron distributions before modification. (c) Electron distributions after the modification. The line drawn in (b) and (c) is a spline curve fitted to the 248° data points to guide the eye. Distribution data is the distribution of 75 keV electrons from a ^{133}Ba source. No HV applied to the barrier and with 800 A current applied to the coils. Errors for radius are ±0.5 mm for inner segments (r≤8 mm) and ±1 mm for the rest. Typical error for rate is ±3%. Errors are omitted for clarity.

magnetic shielding (see section 3.5.2) and moving the detector left. In order to accommodate the lateral movement the original beam collimator situated left of the detector looking from the target had to be redesigned for smaller bore size and the detector movement mechanism was adapted with offset pieces that allowed movement outside of the original ±5 mm range.

3.12 Radial filtering

The electrons travel towards the Si detector by following helical paths. The radius of this helical path is governed by magnetic field strength, electron velocity and the angle between the electron velocity and the magnetic field vectors. Therefore, there is reason to believe that the electron distributions as a function of energy would be well ordered and the maximum radius predictable to a certain degree. Here a method to filter spurious electrons based on their energy and detection position is introduced.

3.12.1 Energy dependence of detection radius

The relativistic formula for the Larmor radius ($R_e(E)$) is

$$\begin{aligned} R_e(E) &= \frac{\beta c\gamma m_e}{eB} = \frac{m_e c\gamma\sqrt{1-1/\gamma^2}}{eB} \\ &= \frac{m_e c\sqrt{\gamma^2-1}}{eB} = A\sqrt{(1+\frac{E}{m_e c^2})^2-1}+C \end{aligned} \tag{3.15}$$

where m_e is the electron mass, c the speed of light, β = v/c, γ=$1/\sqrt{1-\beta^2}$, E the observed energy of the electron, e the electron charge and B the magnetic field and v is the velocity component of the electron perpendicular to the direction of the magnetic field. As the direction and the strength of the magnetic field are not clearly defined near the SAGE silicon detector the last form of equation 3.15 is used as a basis for fitting, with A (=$m_e c/eB$) and C being the fitted parameters. The additional coefficient C is purely for fitting purposes.

3.12.2 Definition of the maximum radius

For future reference the maximum radius $R(E)_{max}$ is defined to be the point where the normalised count rate $d_e(r)$ drops to the background level, which in practice is zero. The general form of the fitted function is

$$d_e(r) = a \times Exp(-b(r-r_0)^2) + cr + d, \tag{3.16}$$

where a, b, c, d and r_0 are fitted parameters and r is the radius in mm. Note that the distributions for a particular energy have a slightly different shape with more prominent tail to larger radii than the total distribution and the distribution fit function (Eq. 3.16) is modified to compensate for this by adding the linear part. An example of extracting the maximum radius from electron distributions is shown in figure 3.42. The maximum radii for conversion electrons emitted from ^{133}Ba and ^{207}Bi sources are shown in figure 3.43 along with fits

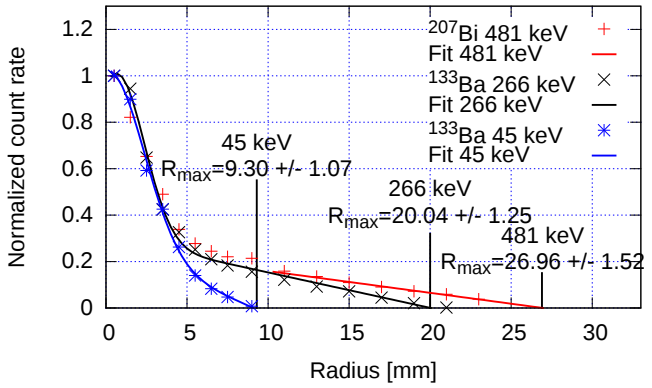

Figure 3.42: Energy gated electron distributions with maximum radii per energy extracted. The fit functions are based on equation 3.16. Errors for radius are ±0.5 mm for inner segments (r≤8 mm) and ±1 mm for the rest. Typical error for rate is ±2%. Errors are omitted for clarity.

based on equation 3.15. The maximum radius values for conversion electrons from the ^{207}Bi source are determined by extrapolating the measured distribution and have large errors. Therefore only the distribution of the 481 keV electrons is taken into account in the fitting.

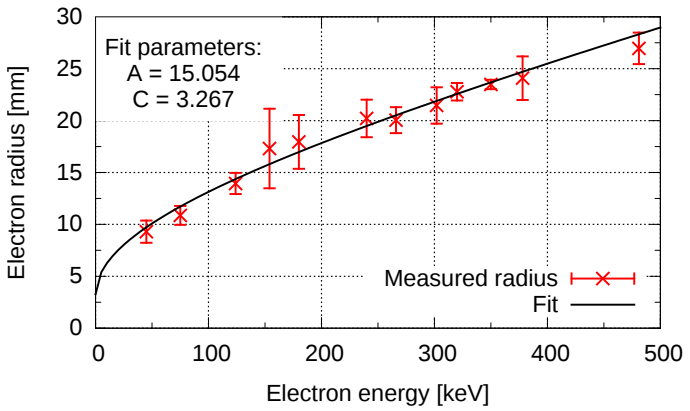

Figure 3.43: Measured values of the maximum radii as a function of energy with a fit through the data using equation 3.15.

After the $R_e(E)$ function is fitted for a certain coil current (here I_{coils}=800A) the function can be used to reject scattered, partially detected and electrons generated off-centre of the target position by simply demanding that the de-

tection radius for electrons with energy of E is smaller than $R_e(E)$ given by function 3.15 with fitted parameters. Note that the detection radius must be randomised within the segment limits in order to avoid artefacts. An example of the effect of the radial filter is shown in figure 3.44.

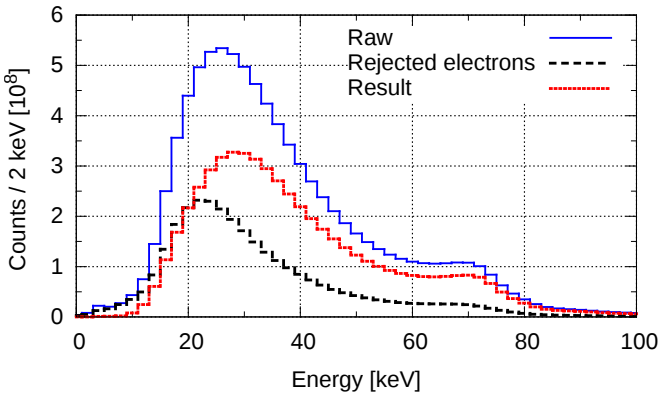

Figure 3.44: Effect of the radial filter on ^{154}Sm Coulex data shown in detail in section 4.1.

3.13 Kinematic energy correction

Electrons

If the electrons are emitted from nucleus in-flight a kinematic correction to the detected electron energy must be made. The corrected electron energy (E_e) has a form

$$E_e = \frac{E_d + m_e - \beta cos(\theta)\sqrt{E_d^2 + 2m_e E_d}}{\sqrt{1-\beta^2}} - m_e. \tag{3.17}$$

Where E_d is the detected electron energy, θ is the electron emission angle compared to the incident beam axis, m_e electron rest mass and β is the velocity of the nucleus as a fraction of c.

γ-rays

The Doppler correction for γ-rays can be deduced from equation 3.17 by setting the mass to zero. Now the corrected γ-ray energy (E_γ) is

$$E_\gamma = \frac{E_d(1 - \beta cos(\theta))}{\sqrt{1 - \beta^2}}, \tag{3.18}$$

where E_d is the detected γ-ray energy and θ is the angle at which the γ-ray was detected.

3.14 Add-back/veto method for SAGE

3.14.1 Description of the method

The range of high energy electrons in silicon far outreaches the typical segment dimensions (1×3×1mm) of the SAGE silicon detector. A number of the high energy electrons simply punch through the 1mm thick detector and deposit only a fraction of their full energy. In addition a significant fraction of the high energy electrons may scatter to an adjacent segment and thus deposit energy in two or more segments. Both the "punch through" and inter segment scatter events add to the background. The "punch through" events are unrecoverable but the inter segment scatter events can be detected and their full energy can be recovered with a simple algorithm. The outline of the add-back algorithm is presented in figure 3.45. The method is similar to that used for γ rays in Clover detectors [60]. In veto mode electron energies are not summed but the electrons are removed from the electron array.

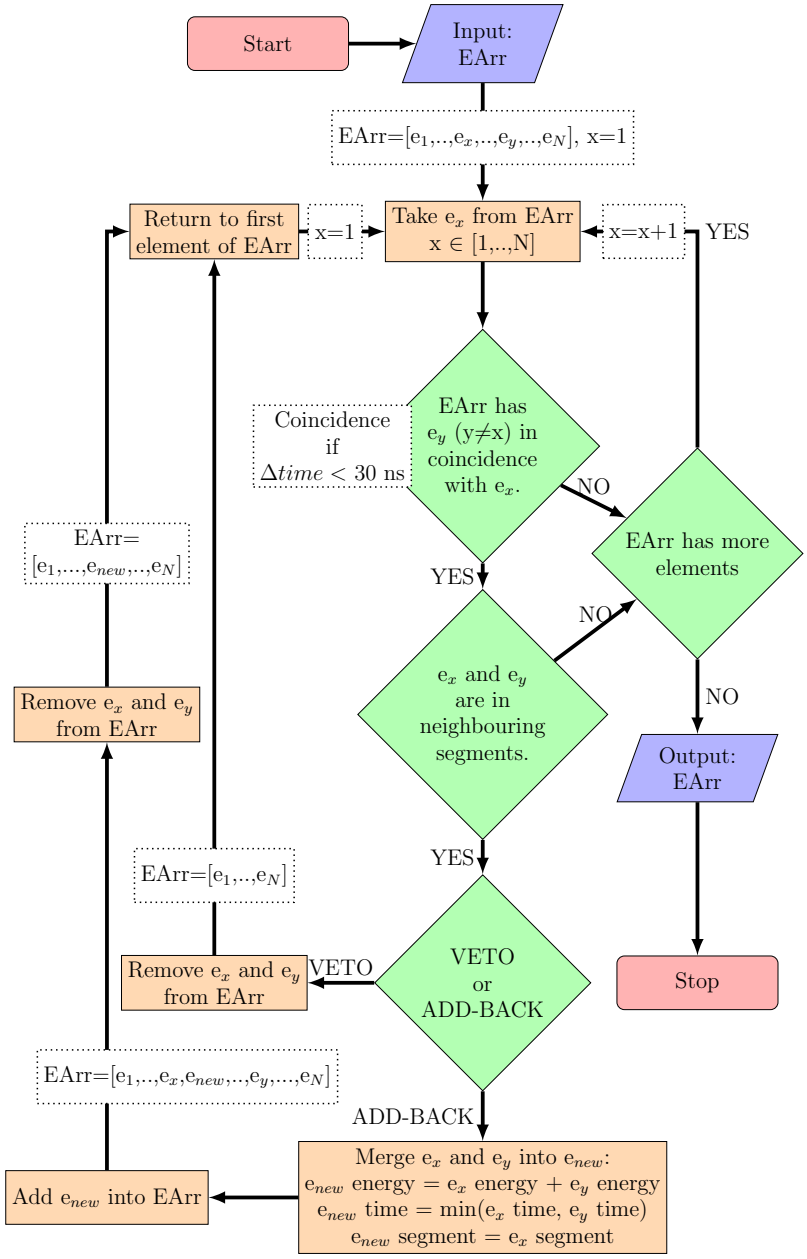

Figure 3.45: Algorithm used to execute the add-back procedure. EArr is an array containing a list of detected electrons with their energy, position and time attributes. The figure is taken from Ref. [79]. Note that *either* add-back or veto is executed.

3.14.2 Neighbouring pixels

The SAGE detector is highly segmented and there are several different ways to define the segments that should be associated within the add-back procedure. Different schemes were tested and the best was noted to be the one where all the neighbouring segments within the central region of the detector are grouped together and those with the longest common borders thereafter. The search scheme for six different pixel types is shown in figure 3.46. A very strict time gate (±30 ns) is used to determine a coincidence. A wider neighbour designation scheme shown in figure 3.47 was also tested. The results with the different search schemes are compared in the next section (figure 3.49).

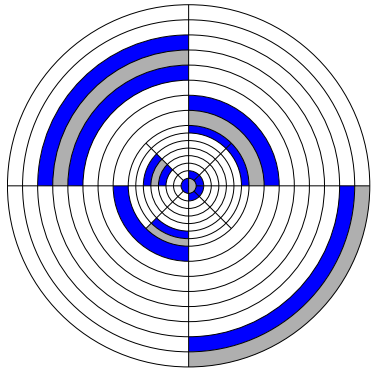

Figure 3.46: Scheme 1 add-back (AB1) search patterns for different segment types. Gray color shows the segment where the first event is detected, the adjacent blue segments are searched for coincident events.

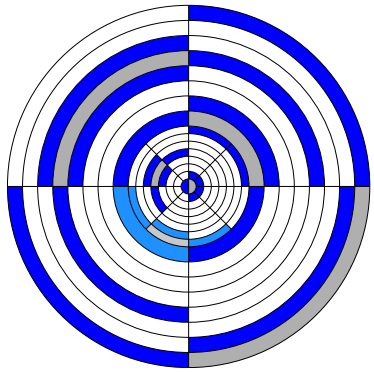

Figure 3.47: Scheme 2 add-back (AB2) search patterns for different segment types. Gray color shows the segment where the first event is detected, the adjacent blue segments are searched for coincident events. Note the shade differences near the center to differentiate two cases.

3.14.3 Source tests

Standard conversion electron sources have been used to study the efficiency and reliability of the add-back method. A double hit is defined by simultaneous detection of electrons in adjacent segments within 60ns of each other. If the summed energy of these two events passes the radial filter requirements (Sec. 3.12) the singles and sum spectra are incremented. The result obtained with a ^{207}Bi source is shown in figure 3.48. The peak areas measured with

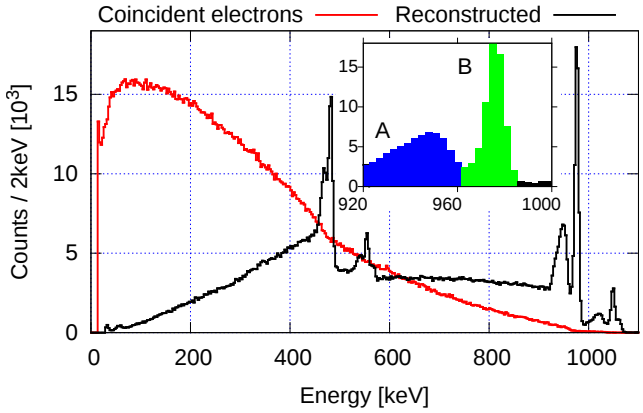

Figure 3.48: A reconstructed ^{207}Bi spectrum (black line) along with summed coincident electrons (red line). *Inset* Typical peak shape in the reconstructed spectrum. Peak A corresponds to events scattered between segments through inactive detector layers and events escaped without full energy deposition. Peak B is the full energy peak.

different add-back schemes using conversion electrons from ^{133}Ba and ^{207}Bi are shown in figure 3.49. With the ^{133}Ba source there is very little difference between the different add-back schemes but with the ^{207}Bi source the difference is clear. Such behaviour is expected based on the conversion electron energies from ^{207}Bi. Scheme 2 generates peaks with slightly higher intensities at high energies. However, the scheme 2 add-back starts to pick up full energy events and electronic noise as shown in the figures 3.50 and 3.51. These effects will be further amplified in the in-beam experiments where the count rates are much higher. Therefore, it was decided to use scheme 1 as the default option in analysis. The effect of add-back on the electron detection efficiency is shown in figure 3.52. The effect of the add-back levels around 1 MeV so that the total efficiency with add-back is twice the singles efficiency.

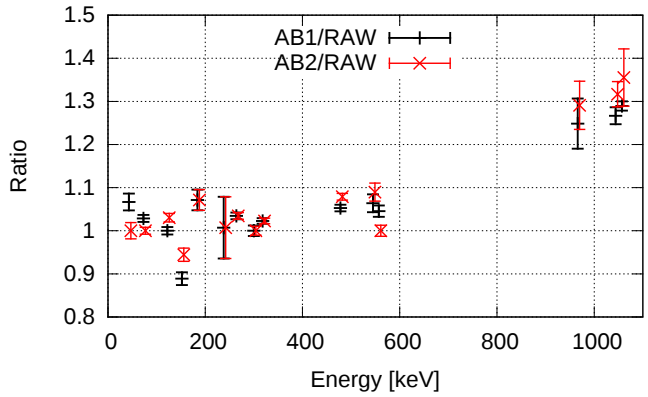

Figure 3.49: Relative peak areas from standard sources (^{133}Ba,^{207}Bi) using the add-back algorithm with different segment search schemes. Note that the energy of the points is offset by ±2 keV for clarity.

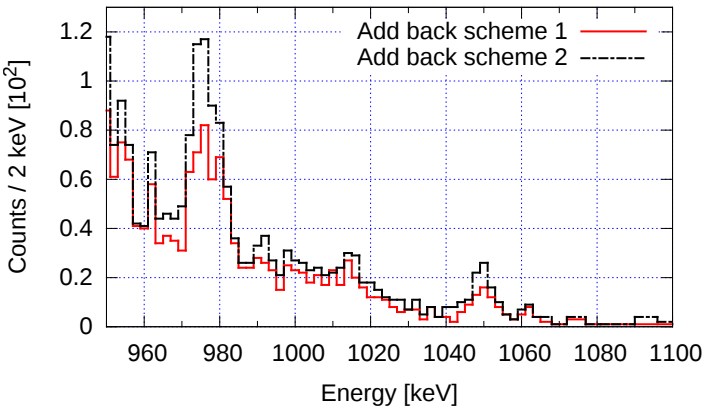

Figure 3.50: Main characteristics of ^{207}Bi coincident electrons spectrum detected by the different add-back schemes. At lower energies both histograms are featureless but scheme 2 picks up approximately 5% more events.

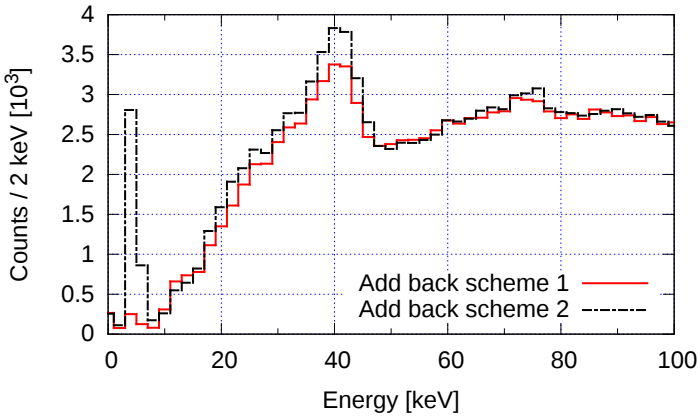

Figure 3.51: Low energy part of the ^{133}Ba coincident electrons spectrum produced by two different add-back schemes. Beyond the upper limit of the plot the spectra are almost identical.

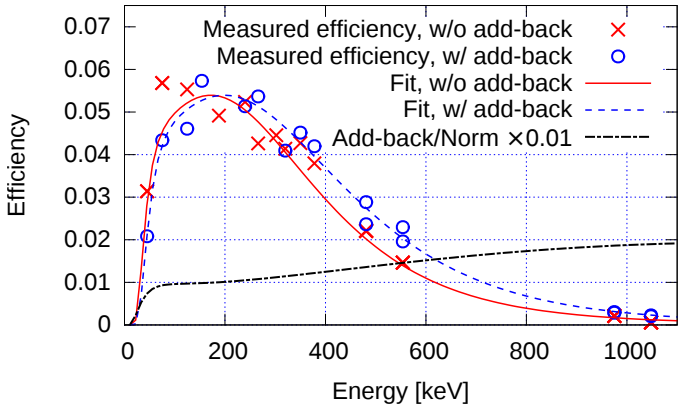

Figure 3.52: Effect of add-back procedures on the electron detection efficiency. The efficiencies were measured without the carbon foil holder or HV applied to the barrier. The radial filter is applied to the data following the add-back procedure. Typical error error in the measured point <5%. Errors are omitted for clarity.

3.14.4 Si detector segment separation

As can be seen in figure 3.48, the add-back algorithm generates a very distinctive peak shape. The presence of a full energy peak along with a low energy

peak is due to the fact that the segments are partially separated by a passive layer. In order to quantify and understand the spectra and the peak shapes, a simulation was performed. The simulation is based on known electron energy loss data from the ESTAR database [80] and the scattering is modelled with a simplified diffusion model based on Ref. [81]. The simulation parameters were calibrated so that the model reproduces the electron backscattering coefficient [77] and the "punch through" ratio estimated from ^{207}Bi spectra in this energy range. A 3×3 segment (1×3×1mm) matrix was used in the simulation. The electrons were set to hit the center segment and the consequent energy deposition to the segments was followed. If scattering between segments was detected the add-back algorithm is applied as presented for the physical case. A segment structure partially separated with an inactive silicon layer gives a result consistent with the measured data as shown in figure 3.53. The simulation suggests that an inactive layer below the segment borders extends ∼300μm down into the bulk silicon.

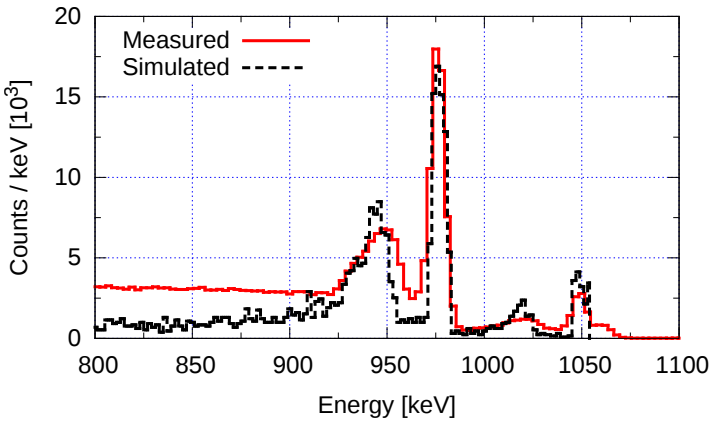

Figure 3.53: A comparison of the simulated and experimental electron peak shape generated using the add-back algorithm.

3.15 Si detector dead layers

According to the Si detector manufacturer the Si detector has a 4 keV electron cut off due to the surface metallization layers but the detailed structure of the metallization layers is not available. In order to create an approximate model of the dead layers the silicon detector response was tested with ^{148}Gd and ^{241}Am alpha-particle sources. The alpha particle sources were mounted on the target wheel and the resulting energy spectra measured. As the energy loss of an alpha particle is higher than that of an electron the measured alpha-particle energy

loss yields information concerning the dead layers on the surface of the active area of the Si detector. The linear gain function determined with electrons from ^{207}Bi source is used as a reference, and the measured energy shifts for alpha particles are shown in figure 3.54.

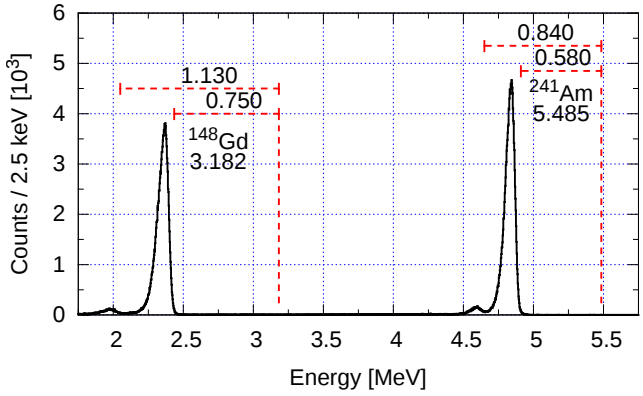

Figure 3.54: Measured alpha peaks and energy shifts from expected positions. Numbers in the figure are in MeV.

The secondary peaks are caused by the signal wires running on the surface of the detector. As the energy calibration is made with electrons the pulse height defect (PHD) for alpha particles needs to be taken into account and corrected for. An estimation of the PHD for alpha particles (and oxygen) based on Ref. [82] using protons as a reference is shown in figure 3.55. The PHD effect in Ref. [82] is calculated by using protons as a reference. Extension of this to electrons is feasible as the pulse-height versus energy behaviour is similar for electrons and protons [83]. The energy shifts due to PHD are roughly 130 keV for ^{148}Gd and 200 keV for ^{241}Am. Note that the full energy of the alpha peak is used in the PHD estimation. Energy losses due to the dead layers are then 620 keV for ^{148}Gd and 380 keV for ^{241}Am. By using the energy-range method [84] with energy loss data from NIST [85] these energy shifts correspond to aluminium dead layers of 4.82μm and 4.77μm respectively. The measured values are consistent with the simulation model presented in the work of Cox et al. [86] when differences in dead layer material are taken into account. The dead layer thickness will play a part later in the text when energy of a backscattered heavy ions is studied in section 4.3.

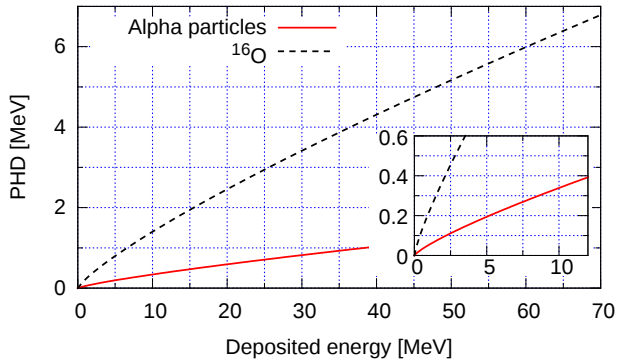

Figure 3.55: The pulse height defect as a function of measured energy for alpha particles and ^{16}O with proton as a reference. The PHD function is taken from figure 5 of Ref. [82].

3.16 Time gate selection

When coincidence measurements are performed, suitable time limits must be set to define coincident events. Normally in the case of γ-γ or γ-electron coincidences the time differences between detections are recorded and a gate is defined from the resulting histogram (see, for example, figure 3.56). When the related study is focused on relative values or there are appropriate reference points this approach is acceptable. With these elements missing the single time gate may be problematic. The long tails in the time difference spectrum result from the fact that low energy events may have a greater variation in the detection time. In order to overcome this problem, it becomes necessary to create energy-gated time difference spectra, and to produce energy dependent time gates. As seen in figure 3.57 the energy gated coincidences have a different behaviour as compared to the single gate. The energy dependent time gates can be made narrower than the single gate thus reducing the background levels and more importantly keeping the relative peak areas correct. Figure 3.57 is generated such that the full time range [-200:200]ns is cut into 20 ns slices ([-200:-180[,...,[180:200]) and a coincidence matrix is generated separately for every slice. The number of energy gated coincidences is extracted from these matrices and divided by the number of coincidences from the full time range matrix. The energy dependent time gate limits for γ-γ coincidences are visualised in figure 3.58. The gate limits form a distinctive shape and the limits can be fitted with functions of the form

$$f(E) = A1 \times Exp(\frac{B1}{\sqrt{E}}) + C1, \tag{3.19}$$

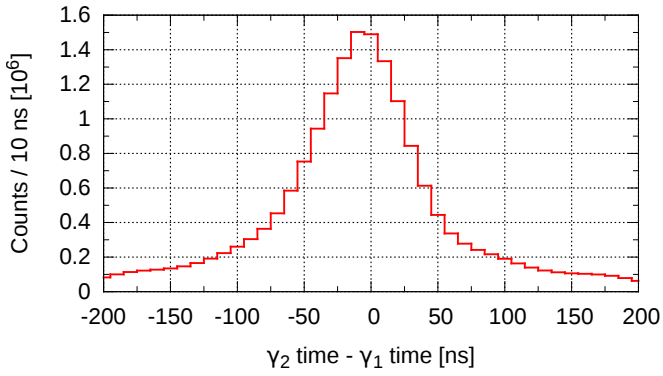

Figure 3.56: An example of a gamma-gamma time spectrum from ^{154}Sm Coulex experiment. Here a bulk gate would be placed to be [-100:80]ns.

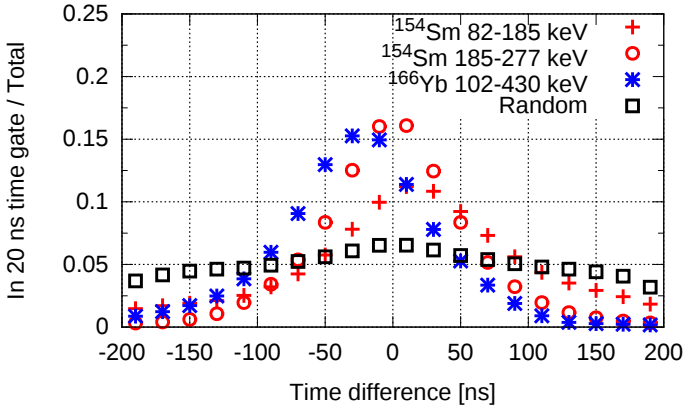

Figure 3.57: Relative contributions to time difference spectra for selected coincidence pairs. The single gate in this case would be [-100:100]ns. For example for 82-185 keV coincidence the energy dependent gate is [-60:100]ns. The error in the time difference is ±10 ns and a typical error in the ratio is ±2%.

where E is the energy in keV and A1, B1, C1 are the fitted parameters.

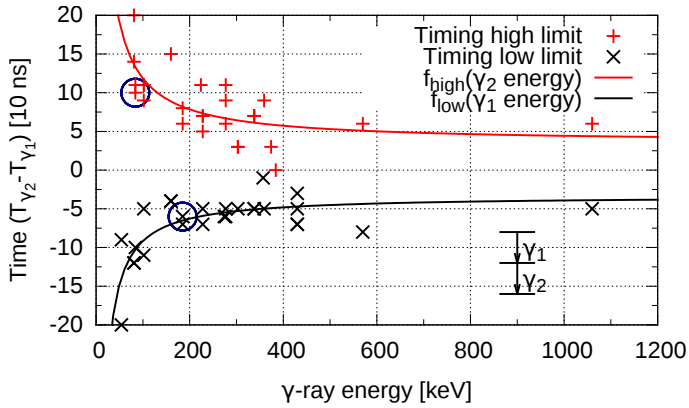

Figure 3.58: Gamma-gamma timing. The two circled points correspond to the example limits from figure 3.57 for the 82-185 keV coincidence. The error in time difference is ±10 ns and in the energy ±1 keV.

In the γ-γ coincidence data the low limit is related to de-excitation observed first and the high limit to the second in the coincidence cascade. In the γ-electron coincidence data both limits can be fitted as a function of γ-ray energy.

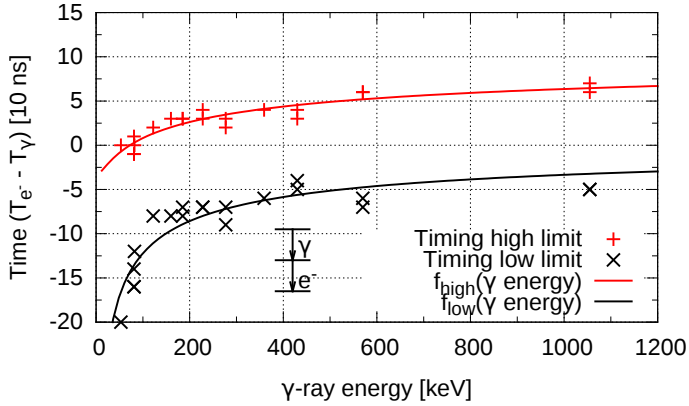

Figure 3.59: Gamma-electron timing. The error in time difference is ±10 ns and in the energy ±1 keV.

The energy dependent time gates prove to be a significant factor when the absolute conversion coefficients for ^{154}Sm are experimentally studied in section 4.1.

3.17 Angular correlation measurements

As presented in section 2.3 angular correlations can be used to determine the multipole order of a transition. The application of the angular correlation method with JUROGAMII is a fairly straightforward task. The detection angles of cascading γ rays (γ_1 and γ_2) are known based on the detector positions and the angle between the γ-rays ($\theta_{12} = \measuredangle(\gamma_1\gamma_2)$) can be calculated easily. Matrices of γ - γ coincidences with set θ_{12} limits are constructed and the number of observed coincidences are extracted from those. The numbers of coincidences are efficiency normalised to the matrix collecting events at an angle of 90°. A correlation function of

$$W(\theta)_{exp} = A0 + A2 \cdot P_2(cos(\theta)) + A4 \cdot P_4(cos(\theta)) \tag{3.20}$$

is fitted to the measured angular correlation data. Finally the measured angular correlation function is normalised to match with a known function. The normalisation step takes into account the attenuation factors and so the tabulated maximum values for A2 and A4 can be used.

^{207}Pb 1064 - 570 keV cascade

The angular correlation function of 1064 - 570 keV (M4+E5/E2) cascade from ^{207}Pb is well known and used as a standard [87]. Therefore it can be used to calibrate the angular correlation measurement. The cascade is studied from the decay of ^{207}Bi from a calibration source. The measured angular correlations are shown in figure 3.60 along with a fit according to equation 3.20, the IAEA standard and calibrated angular correlation function. The comparison to IAEA standard yields correction coefficients of 1.1 and 1.5 for A2 and A4 respectively.

In-beam data test

The angular correlation method is also tested with transitions from in-beam data. For example, an angular correlation of 276-185 keV (E2/E2) cascade from ^{154}Sm Coulex data was measured and shown in figure 3.61. As can be seen from figure 3.61 the measured angular correlation curve is reasonably close to the theoretical one and just looking to this data there is no need to apply the calibration constants. However in the Pb case the need for the adjustment is large and as the calibrated curve in ^{154}Sm case is still within errors the correction is retained in the subsequent calculations.

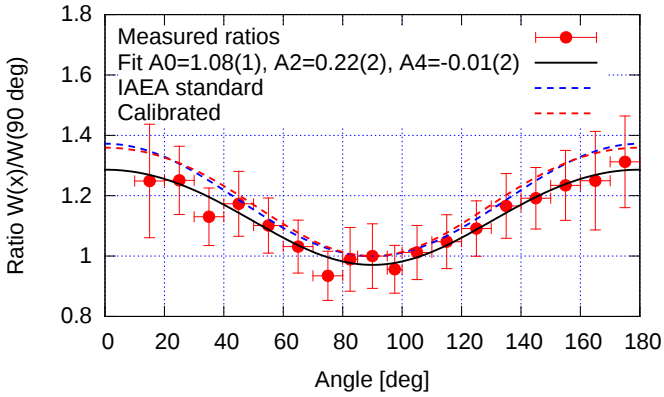

Figure 3.60: The angular correlation for the ^{207}Pb 1064-570 keV γ-ray cascade.

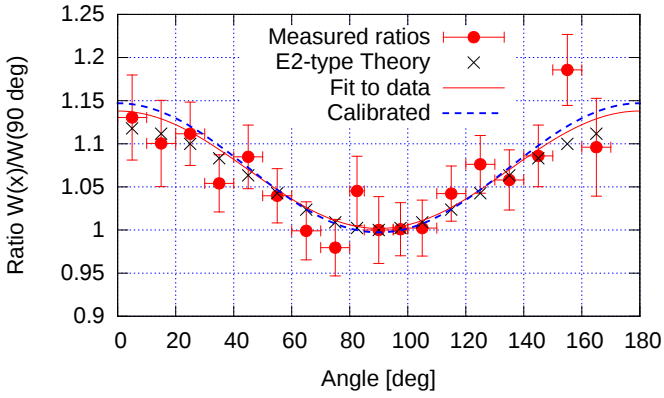

Figure 3.61: The angular correlation for ^{154}Sm 276-185 keV cascade.

Chapter 4

Experimental cases

The main purpose of the SAGE spectrometer is to provide spectroscopic information of nuclei, especially by means of γ-electron coincidences. As the experimental conditions such as reaction cross sections, beam intensities, target purities and so on vary considerably it is of interest to study the performance of the SAGE spectrometer in different cases. In the following chapter studies of ^{154}Sm and ^{194}Po are introduced as examples of different experimental conditions. In both cases the main physical information was carried by internal conversion and in both of the experiments accurate determination of absolute ICCs is crucial.

In the samarium study the rate of events counted by the JUROGAMII and Si-detector were close to the upper limits of the measurement system capabilities resulting in large numbers of false coincidences that affect the determination of ICCs. Even though in this case known transitions and ICCs can be used as a reference, a method to counter the effect of the false coincidences by means of time gating is introduced for future reference (section 3.16). The origin of the peculiar high energy background detected during the analysis is also discussed as a potential origin of electron background.

In the polonium study the recoil-decay-tagging method was used and subsequently the rate of coincident events was much more agreeable. This experiment presents a more typical experimental case. Due to the low statistics, this experiment can be considered as a benchmark that needs to be exceeded in order to gain conclusive results.

With polonium, and to a lesser extent also with samarium, a part of the experimental challenge arises from the fact that the transition mixing-ratios (see section 2.2.1) are not generally known. In these cases an attempt to extract the

mixing ratio from γ-γ coincidences has been performed but the resulting mixing ratio values are tentative. This is a definite weakness of the SAGE spectrometer and merits further investigation during the development of the spectrometer or more simply points to a need to perform separate complementary experiments.

4.1 Internal conversion coefficients of ^{154}Sm

4.1.1 Experiment details

The nuclear structure of ^{154}Sm has been recently discussed by Smallcombe *et al.* [88]. The object of the experiment was to measure internal conversion coefficients from the excited rotational bands of ^{154}Sm in order to test the hypothesis that the bands have vibrational (β-band) structure. The hypothesis is tested by measuring the $\rho^2(E0)$ value of the I-I transitions (see equation 2.36) that is expected to be between 85×10^{-3} to 230×10^{-3} [89]. Based on equation 2.44 if the difference in quadrupole deformation of the initial and final states, as well as the mixing amplitudes are the same, the value of $\rho^2(E0)$ will be the same for all I-I transitions. Therefore transitions (shown in figure 4.1) of this type are under experimental scrutiny.

Coulomb excitation with the reaction ^{154}Sm(^{16}O,^{16}O)^{154}Sm* was used to populate the excited energy levels in ^{154}Sm. Excitations up to the 12^+ state could be seen along with transitions arising from ^{152}Sm target impurities and ^{166}Yb created by sub-barrier fusion. A γ-ray spectrum showing the lowest ground state band transitions is presented in figure 4.2. An example of electron spectrum quality is shown in figure 4.3.

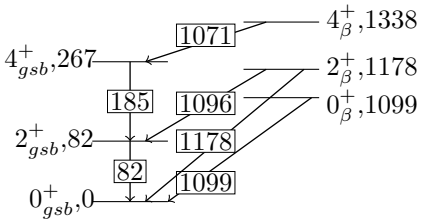

Figure 4.1: Partial level scheme of ^{154}Sm with assumed β-band to ground state band transitions. Level and transition energies are in keV.

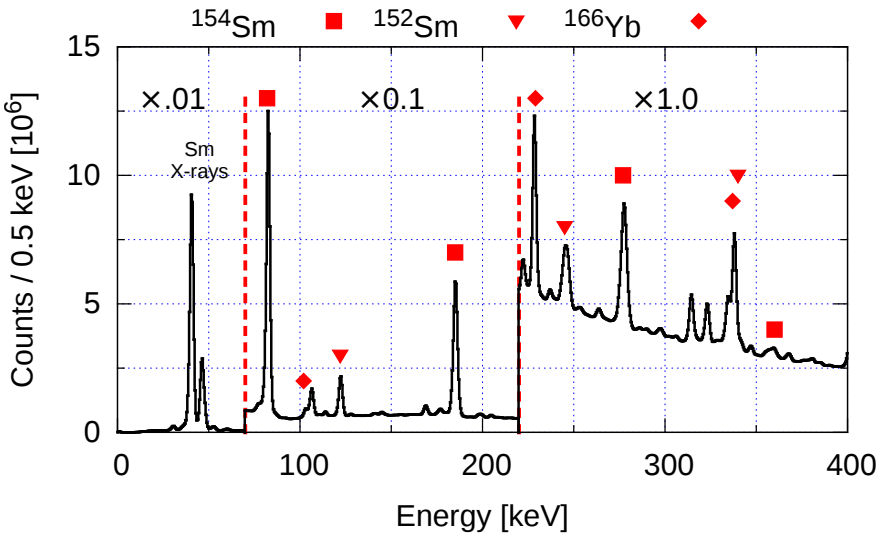

Figure 4.2: A total JUROGAMII "singles" spectrum measured during the ^{154}Sm experiment. Note that in the experiment the data recorded to disk required electron and/or γ-ray 2≤fold.

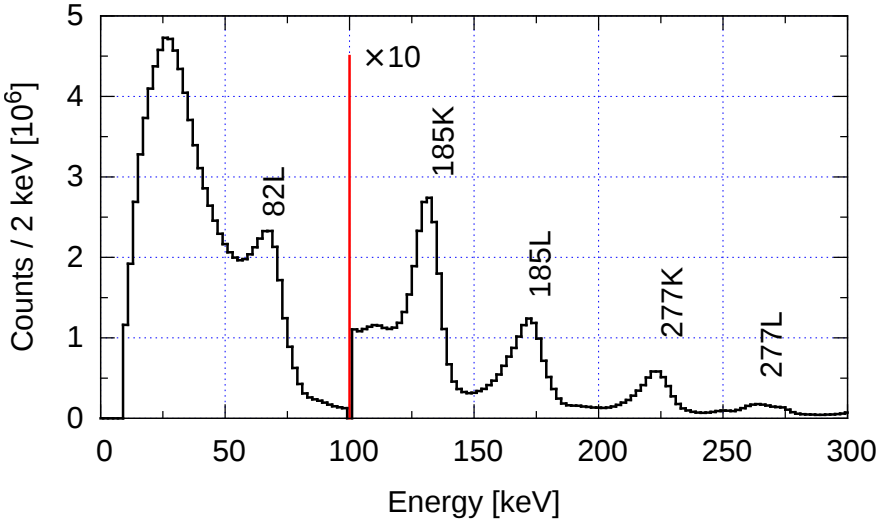

Figure 4.3: A sum of gates (82+185+277+359 keV) electron projection from γ-electron matrix showing the most prominent ^{154}Sm conversion peaks.

The various parameters related to the ^{154}Sm experiment are summarised in table 4.1. The maximum beam intensity mentioned in the table is calculated by using the method described in Ref. [71] and is taken into consideration as the measurement was performed in vacuum mode. In the previously mentioned work by Smallcombe *et al.*, the analysis of the electron-γ and γ-γ coincidence data and extraction of the internal conversion coefficients relies on the Normalised-Peak-to-Gamma (NPG) method [90]. The NPG method relies on the observation of known reference transitions and therefore can not be applied to cases where these reference points are missing. The discussion in this work relies on the same dataset as that used by Smallcombe *et al.* and the data-analysis parameters such as trigger conditions, event widths etc. are as close as reasonably possible to those introduced in Ref. [88] in order to enable direct comparison between results. Note that in the current offline analysis, the DAQ trigger condition (any event with fold two or greater) was changed such that events are created on detection of any γ-ray. This means that a specific sub-set of the original data collected are used in the analysis, events with electrons only are discarded. A partial level scheme of ^{154}Sm is shown in figure 4.4.

Table 4.1: Summary of the ^{154}Sm experiment details. Maximum beam intensity which can be tolerated by the target (Max. beam) is calculated using the procedure from Ref. [71].

Beam	Element	^{16}O	Target	Element	^{154}Sm
	Energy	65 MeV		Enrichment	99%
	Time	37 hours		Thickness	1.5 mg/cm^2
	Intensity (ave.)	20 pnA		Max. beam	85 pnA[a]
SAGE	I_{coils}	800 A	DAQ	Trigger	2≤fold (γ or e^-)
	$U_{barrier}$	-20 kV		Trig. width	±200ns

[a] RITU in vacuum (p=10^{-6} mbar).

4.1.2 Determination of the γ-ray and electron detection efficiencies

In order to attenuate the flux of X-rays originating from atomic reactions, it is usual that Sn (0.1 mm) and Cu (0.5 mm) absorbers are placed between the target and the germanium detectors of JUROGAMII. In the ^{154}Sm experiment, the absorbers were removed in order to allow more efficient detection of Sm X-rays. The absolute γ-ray detection efficiency was measured using calibrated ^{133}Ba, ^{152}Eu and ^{207}Bi sources. The resulting γ-ray detection efficiency curve is presented in figure 4.5. Note that the γ-ray detection efficiency curve deviates from the one shown in Ref. [56] due to the removal of the absorber foils of the JUROGAMII array. The efficiency curves for both γ-ray and conversion

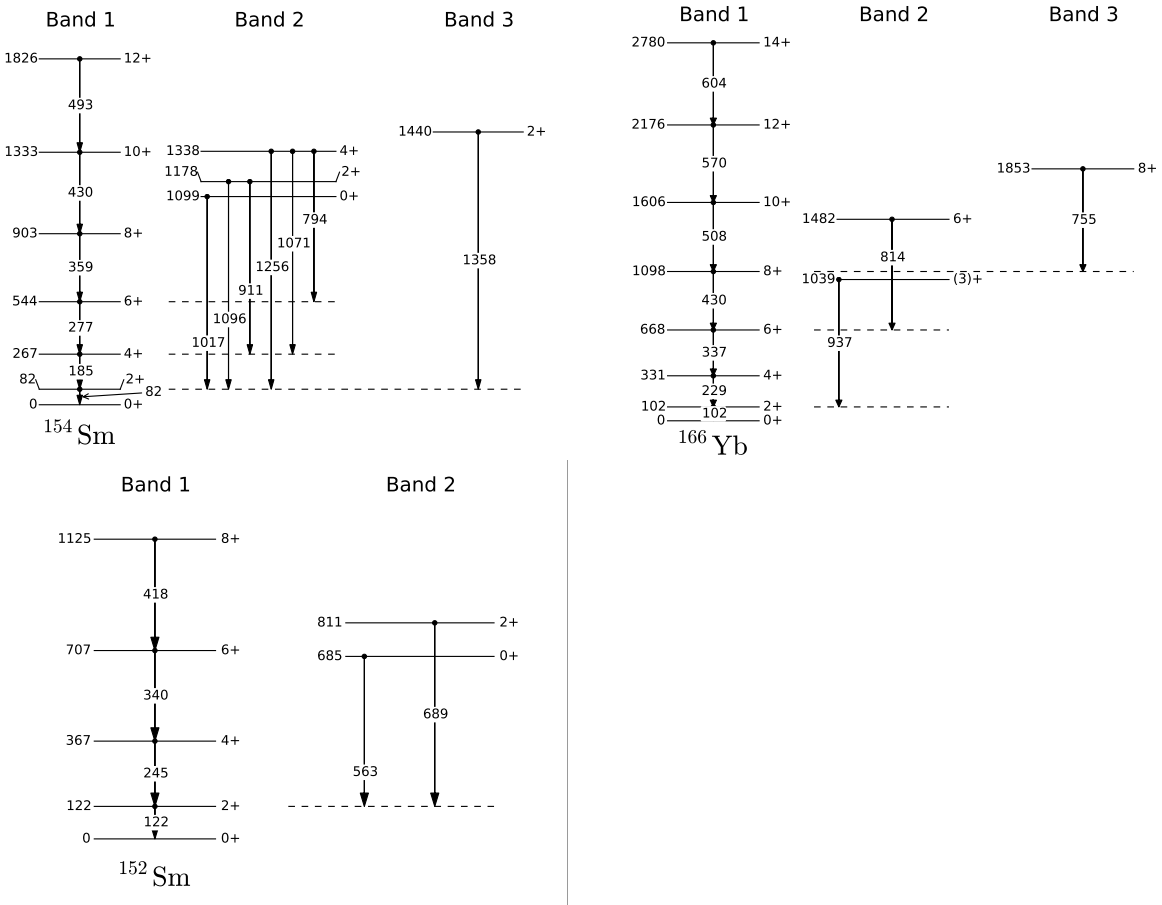

Figure 4.4: Partial level schemes of ^{152,154}Sm and ^{166}Yb. The level and transition energies are rounded to the nearest keV. Data from Ref [91].

electron data are fitted according to the function given in equation 3.9. The electron detection efficiency was determined by using calibrated open ^{133}Ba and ^{207}Bi internal conversion electron (ICE) sources. The resulting electron detection efficiency curve is shown in figure 4.5. The calibration runs during the experiment were made with no voltage applied to the HV barrier and without the C-foil holder. The HV was left off as the conversion electrons from E0 and inter band transitions have energies above 500 keV and the HV barrier should not have an effect. The effect of the HV barrier was taken into account for the efficiency fits which are an average behaviour deduced by fitting data obtained from several measurements performed following the ^{154}Sm experiment. RITU was not used and there was no need for helium gas to be present for target cooling as the target was able to withstand significantly higher beam currents than available (see table 4.1). Therefore there was no need to isolate the HV volume from RITU and the C-foil holder was not installed.

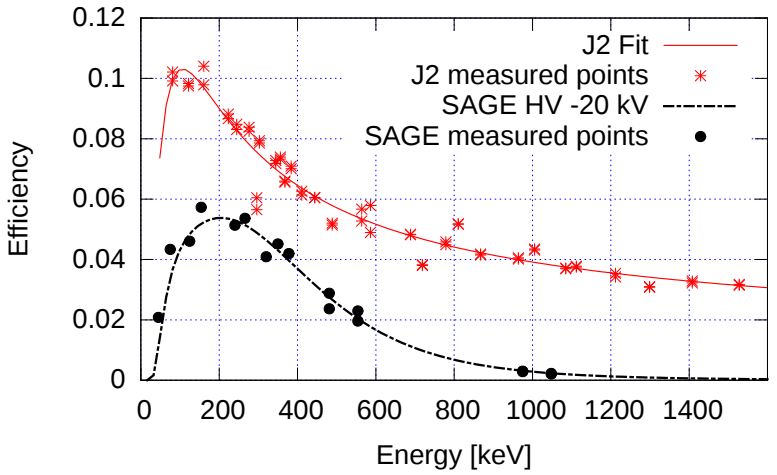

Figure 4.5: Absolute γ-ray (J2) and electron detection efficiencies (SAGE) used in the ^{154}Sm analysis. The electron efficiency curve takes into account the applied HV -20 kV. For the J2 measured points the typical error is of the order of 1% and for SAGE measured points 3%.

4.1.3 Extraction of internal conversion coefficients

In the present work the internal conversion coefficient α_{exp} is determined from

$$\alpha_{exp} = \frac{N_e \times \epsilon_\gamma}{N_\gamma \times \epsilon_e}, \tag{4.1}$$

where N_e is the number of detected electrons, N_γ is the number of detected γ-rays, ϵ_γ and ϵ_e are the detection efficiencies for γ-rays and electrons, respectively. The effect of angular correlations is neglected. All the presented ICCs are obtained from γ-γ and γ-electron matrices by gating with coincident transitions and fitting the resulting peak areas in the projected spectra. Using the data obtained in the ^{154}Sm experiment, a significant number of experimental internal conversion coefficients could be determined. The measured absolute internal conversion coefficients for ^{154}Sm, ^{152}Sm and ^{166}Yb ground state band transitions (all pure E2 character) as a function of electron energy are shown in figure 4.6.

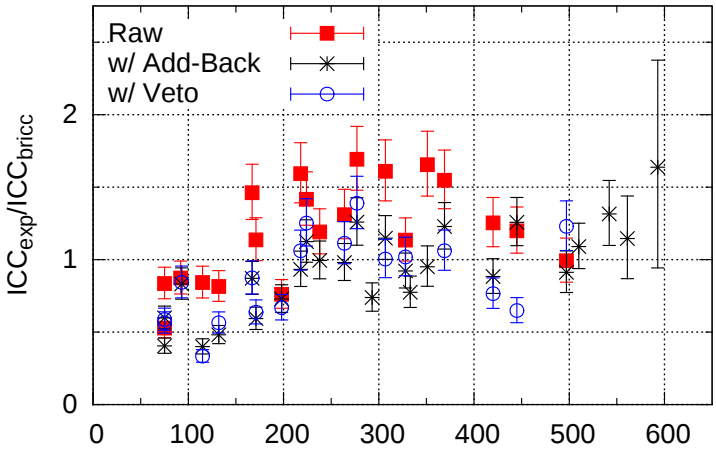

Figure 4.6: A comparison between results for internal conversion coefficients determined from raw data as well as the effect of applying add-back or the veto techniques.

The results derived from the raw (no add-back algorithm applied and/or filtered by radius) matrices differ from the reference tabulated values obtained using the BrIcc [38] conversion coefficient calculator. It can be seen that an energy independent normalisation constant would not yield agreement throughout the full energy range and without a common factor the Normalised-Peak-to-Gamma (NPG) method [92] cannot be used. After application of time gates

(see section 3.16), either add-back or veto (section 3.14) and radial filtering (section 3.12) for the electron events in the silicon detector the overall result is much more agreeable. A more detailed plot of the final result is shown in figure 4.6. As can be seen in figure 4.6 the measured ICCs below 200 keV are systematically lower than the tabulated values. The difference is thought to be the result of the interactions of the electrons with the thick target. The values deduced indicate that ^{166}Yb is less affected. The difference can arise from the fact that ^{166}Yb is produced in a fusion-evaporation reaction, meaning that ^{166}Yb has a kinetic energy of only $\backsim$6 MeV and the range in samarium of $\backsim$0.9 mg/cm^2 with a beam (^{16}O) energy of 65 MeV. This should be compared with that for inelastically-scattered ^{154}Sm which is $\backsim$4 mg/cm^2. As the beam particles pass through the target matter they lose energy and therefore the creation of sub-barrier fusion products deeper in the target matter is less likely. As the electrons emitted from ^{166}Yb travel through less target matter the energy loss is smaller and probability of the scattering is lower. Therefore it is more likely in the ^{166}Yb case that the emitted electrons contribute to the full energy peaks. According to the rule-of-thumb given in Ref [93] the optimal target thickness for measurements of conversion electrons in an energy range of 100 to 500 keV would be 0.3-0.7 mg/cm^2. This is significantly less than the 1.5 mg/cm^2 target used in this case and negative effects on the spectral quality can be expected. The relative simulated effect of the target on electron transmission is shown in figure 4.7. The simulation is performed with the same code as discussed in section 3.14.4. A point like, isotropic electron source is placed in the target at different depths and electrons emitted from the target with acceptable trajectories and energies are counted. In this case electrons with energies >90% of the full energy with less than 2 mm lateral straggling and emission angle less than θ_{max} given by equation **??** are counted. If the ICCs measured below 200 keV are corrected with the rough assumption that samarium conversion electrons originate evenly throughout the target depth and ytterbium conversion electrons just from the first half of the target, the transmission coefficients shown in table 4.2 are obtained. The transmission coefficient is an average relative transmission between the surface of the target (0.0 mg/cm^2) and the maximum emission depth, 1.5 mg/cm^2 for samarium and 0.75 mg/cm^2 for ytterbium based on the rough estimate made earlier in the text. Applying these target transmission coefficients to the measured ICCs yields values close to those calculated by BrIcc. In ^{166}Yb the analysis is further complicated by the overlap of LMN conversion lines and K conversion lines from different transitions.

Table 4.2: Approximate transmission coefficients for ICCs below 200 keV and resulting relative ICCs. All results are obtained using the add-back algorithm.

Origin	e^- energy [keV]	α_{Rel} [a]	Transmission coefficient [b]	Corrected α_{Rel}
^{152}Sm	75	0.59(7)	0.6(1)	1.0(2)
	115	0.39(5)	0.7(1)	0.6(4)
	198	0.73(9)	0.8(1)	0.9(2)
^{154}Sm	75	0.41(5)	0.6(1)	0.7(3)
	132	0.48(6)	0.7(1)	0.7(3)
	171	0.59(7)	0.8(1)	0.7(3)
^{166}Yb	93	0.83(9)	0.8(1)	1.0(2)
	167	0.87(9)	0.9(1)	1.0(2)

[a] $\alpha_{Rel} = \alpha_{exp}/\alpha_{BrIcc}$
[b] Approximated from figure 4.7

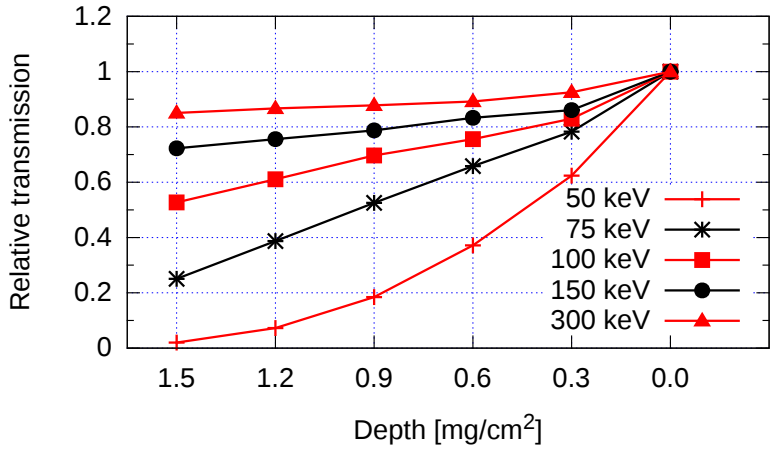

Figure 4.7: Simulated relative electron transmission through Sm target matter.

4.2 Transition strengths

The main goal of the ^{154}Sm experiment was to define conversion coefficients for the transitions connecting the proposed β-band to the ground state band (bands 2 and 1 respectively in the figure 4.4). This gives an opportunity to calculate electric monopole transition strengths ($\rho^2(E0)$) by using equation 2.36. The experimentally defined conversion coefficients for the measured mixed tran-

sitions in ^{152,154}Sm are shown in table 4.3. The results are obtained by using energy dependent time gates, either the veto (V) or add-back (AB) algorithm and radial filtering. When an upper limit is given the smaller value obtained with the different algorithms is given, the larger value is given in the normal case. The level and multipolarity assignments are as listed in NNDC [91] and the upper limits are deduced with a 90% confidence limit according to Ref [52], in cases where a proper integration or fitting of the peak could not be done.

Table 4.3: Experimental results for α_K ICCs for mixed inter-band transitions in ^{152,154}Sm using either veto (V) or add-back (AB) algorithm. The level and multipolarity assignments are as listed in NNDC [91].

Origin	γ energy [keV]	e^- energy [keV]	I_i^π	I_f^π	σL	$\alpha_{K,exp}$ (algorithm)
^{152}Sm	689	642	2_2^+	2_1^+	E0+M1+E2	0.04(2) (V)
^{154}Sm	1071	1024	4_3^+	4_1^+	M1+E2	≤0.038(1) (V)
	1096	1050	2_3^+	2_1^+	M1+E2	≤0.043(1) (V)
	1358	1311	2_4^+	2_1^+	[M1+E2]	≤0.036(1) (AB)

The parameters needed to calculate the monopole transition strengths (Eq 2.36) along with the calculated values are listed in table 4.4. Using the present data, an attempt to deduce a value of δ for the 1071 keV transition has been made, using an angular correlation method similar to that used in Ref. [94]. The measured angular correlations for 1071-185 keV cascade is shown in the figure 4.8. Note that due to the low statistics the angle bin is widened to ±10 deg from the ±5 deg used earlier. The angular correlation function (equation 3.20) is fitted to the data giving values of -0.08(8) and -0.04(9) for the parameters A2 and A4 respectively. With the calibration constants from section 3.17 the final results are $A2_{exp}$=-0.09(9), $A4_{exp}$=-0.1(2). Due to the low statistics also a fit only through angles less than 100° is made to give an estimation of the upper limits for the coefficients. From the restricted fit $A2_{exp}$=-0.29(5) and $A4_{exp}$=-0.4(2). Theoretical values for A2 and A4 based on Ref. [48] are

$$\begin{aligned} A2 &= \frac{1}{1+\delta^2}(0.5 + 2\delta \cdot 0.382 + \delta^2(-0.301)) \\ A4 &= \frac{1}{1+\delta^2}(\delta^2(-0.601)) \end{aligned} \tag{4.2}$$

with the assumption that attenuation effects are corrected by the calibration. The parameter space given by equation 4.2 is shown in figure 4.9. The deduced value of δ is found where both A2 and A4 parameters are produced correctly. From figure 4.9 a value of -0.65(15) can be extracted for the δ with parameters from the full fit. Parameters from the restricted fit yields δ a value of -1.0(2). As the angular correlation data is rather tentative, a mixing ratio of δ=1 is

adopted as in Ref. [95]. Now the monopole transition strength for the 1071 keV transition can be calculated. The comparison between literature values for monopole transition strengths and of those deduced in this work are shown in table 4.5.

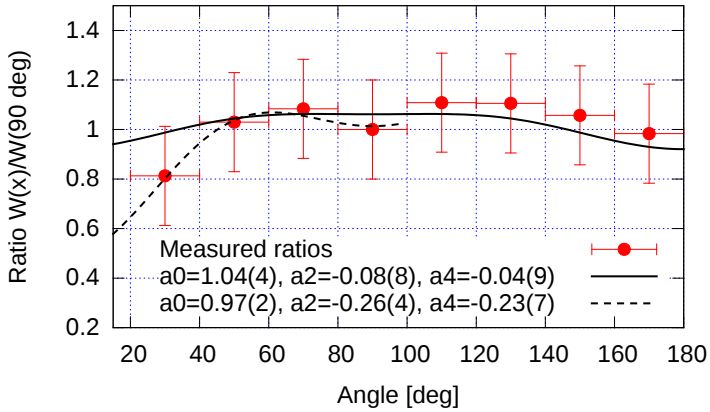

Figure 4.8: Measured angular correlations for the 1071-185 keV cascade. The solid line is a fit through the whole data, the dashed line is a fit through angles less than 100°. Note that due to the low statistics the angle binning is widened to ±10°.

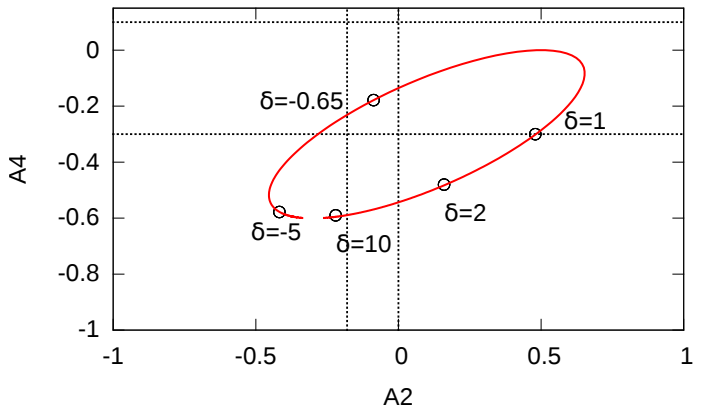

Figure 4.9: The A2 and A4 parameters as a function of δ. Lines indicate the experimentally deduced parameter limits from the full fit in figure 4.8 ($A2_{exp}$=-0.09(9), $A4_{exp}$=-0.1(2)).

Table 4.4: The monopole transition strengths and the parameters needed for the calculation. The most recent literature values are given.

Origin	γ [keV]	α_K Exp.	α_K[a] M1	α_K[a] E2	$\Omega_K(E0)$[a] ($\times10^{10}$)[1/s]	δ	$\lambda_\gamma(E2)$ ($\times10^{10}$)[1/s]	$\rho^2(E0)$ [10^{-3}]
^{152}Sm	689	.04(2)	.00826	.00479	2.29	8^{+6}_{-3}[b]	8.8[c]	140(80)
^{154}Sm	1071	≤.038(1)	.00286	.00183	3.56	-0.65(15)[d]	5(2)[e]	≤180(90)
	1071	≤.038(1)	.00286	.00183	3.56	-1.0(2)[d]	5(2)[e]	≤100(30)
	1071	≤.038(1)	.00286	.00183	3.56	1[f]	5(2)[e]	≤100(5)
	1096	≤.043(1)	.00271	.001746	3.65	-30(21)[e]	6.8(9)[e]	≤76(14)
	1358	≤.036(1)	.001648	.00114	4.68	-19(10)[e]	89(9)[e]	≤67(9)

[a]Calculated with BrICC [38].[b]From Ref. [96].[c]From Ref [91].[d]This work.[e]From Ref [94].
[f] Adopted value.

Table 4.5: Experimental results for ^{152,154}Sm monopole transition strengths compared with literature values.

Origin	γ energy [keV]	$\rho^2(E0)$ [10^{-3}] Exp.	Ref. [97]	Ref. [88]	Ref. [98]
^{152}Sm	689	140(80)	69(6)	56(14)	-
^{154}Sm	1071	≤100(5)[a]	-	$8.2^{12.0}_{-8.2}$	-
	1096	≤76(14)	-	≤9.4(15)	<6.3
	1358	≤67(9)	-	-	2.9[b]

[a] The smallest value from table 4.4 presented. [b] From figure 5 of Ref. [98].

Summary of the ^{154}Sm ICC results

As can be seen from figure 4.6 and table 4.2 the presented data processing methods, add-back/veto and time gate selection, do improve the absolute ICC measurement reliability. On the other hand they reduce overall statistics and have an adverse effect on the determination of ICCs from weak transitions such as are presented in table 4.5, where in many cases only an upper limit for the ICC could be given. Overall, the present analysis does not radically improve on the work done by Smallcombe [88] in the case of extracting ICCs from very weak transitions but on the other hand the present work provides a tool set for absolute ICC determination from γ-electron coincidence data in general. The monopole transition strengths measured in the present work do not bring additional information on the question of the β-band assignment but the values are, at least, roughly consistent with literature values i.e. no anomalously small or large upper limits were deduced.

4.3 ^{154}Sm low gain test

During the initial ^{154}Sm experiment an unexpected number of overflow events, that is events that exceed the maximum detection energy of the ADCs, were recorded in the SAGE silicon spectra. As can be seen in figure 4.10 the number of these events exceed that expected from the shape of the measured spectrum. As the reaction used in the experiment should not create alpha- or high energy β-emitters these events were suspected to be backscattered beam (^{16}O) particles. The fraction of beam that scatters to the silicon detector, calculated using the Rutherford backscattering (RBS) formula [20], is 1.1×10^{-9}. With the measurement time (37 hrs) and average intensity (20 pnA) from table 4.1, the expected number of backscattered ions is $\sim5.4\times10^{7}$. This is somewhat lower than the number of events calculated from the measured spectrum (2×10^{8}). As the integration takes into account all events above 1.7 MeV, the measured number of backscattered events is expected to be larger than the calculated number. The source of the overflow events was investigated further by imple-

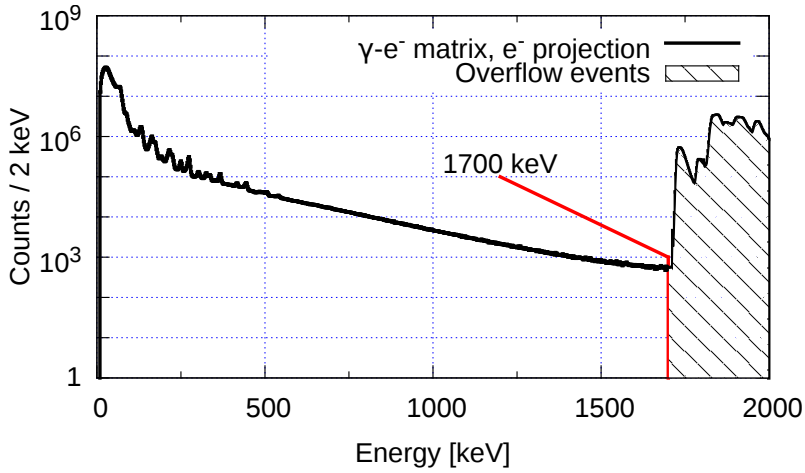

Figure 4.10: A silicon detector spectrum showing the overflow events recorded during ^{154}Sm experiment. Integration over the shaded area yields 2×10^{8} events.

menting voltage dividers in the Si detector signal chain for the outer segments (59-90) and repeating the experiment with the same beam (^{16}O) but different targets and beam energies. The dividers were designed to attenuate the signal by a factor of 10 but in fact the full energy range changed from 2.5 MeV to a maximum of 40 MeV based on the measured energy distributions of backscattered oxygen. The measured gain reduction is thought to be larger than expected due to inactive detector layers and pulse height defects. Both effects hindered the detection of alpha particles (used for calibration) more

than electrons thus lowering the apparent gain. The energy loss of 40 MeV ^{16}O ions in the detector dead layer (5μm aluminium, see section 3.15) is roughly 8 MeV. Combined with PHD of ∼4 MeV (from figure 3.55) this leads to an apparent energy of 28 MeV. For 20 MeV ^{16}O ions the losses arising from dead layers and PHD are 9 MeV and 2.5 MeV respectively. The effects of the dead layers and the PHD were taken into account when the energies of the heavy ions were deduced. The test run was made in two parts. The first part of the experiment ran with a bombarding energy of 35 MeV, the aim of which was to confirm that the high-energy events were backscattered beam particles. The second part ran with an energy of 65 MeV as in the original experiment, in order to test gating the electron spectra with the high-energy events. The lower-energy limit for the K130 cyclotron is 2 MeV/u and as a result the 35 MeV part of the test, with ^{16}O having an energy of 2.2 MeV/u, could be ran only with a beam intensity of 10 pnA. The expected ratio of detected RBS particles for 35 MeV beam on samarium is 2.3×10^{-9}. With a measurement time of 17.8 hrs and an average beam intensity of 10 pnA the number of backscattered events should be 9×10^{6}. This is rather close to the value given by the measurement (6.5×10^{6}). As seen in figure 4.11 the "overflow" events behave like backscattered beam particles. The distributions change their position as expected. The energy distribution of the scattered particles corresponds to the calculated distribution from a 1.1 mg/cm^2 ^{154}Sm target. The identification of backscattered ^{16}O was further confirmed when the beam energy was changed, resulting in a corresponding shift in the energy of the backscattered particles. For diligence, the target used in this test experiment was subjected to an investigation similar to that presented in appendix A.1, revealing that changes in the target are negligible and the presented effects can not be the result from target degradation. By selecting events in coincidence with backscattered ^{16}O, the events arising from sub-barrier fusion such as ^{166}Yb can be removed. A normalized γ-ray projection coincident with backscattered ^{16}O ions is shown in figure 4.12. After demanding the coincidence, the contribution from ^{166}Yb (102, 228, 338, 430 and 507 keV peaks) is significantly smaller compared to that from ^{154}Sm (82, 185 and 277 keV). However, the peak areas for samarium are significantly reduced. In the raw projection of the γ-e^- matrix the peak area of the 185 keV transition is on the order of 10^8 but in the gated projection only on the order of 10^3. Since the statistics obtained in the short test run were rather low, the data were not analysed further. However, with a longer run and improved detection system demanding a coincidence with scattered particles could produce exceptionally clean data for the extraction of ICCs. This effect has been considered to be utilized by instrumenting SAGE with coincidence detectors based on plastic fibre optic cables [99]. These cables would be placed around the silicon detector to monitor backscattered ions.

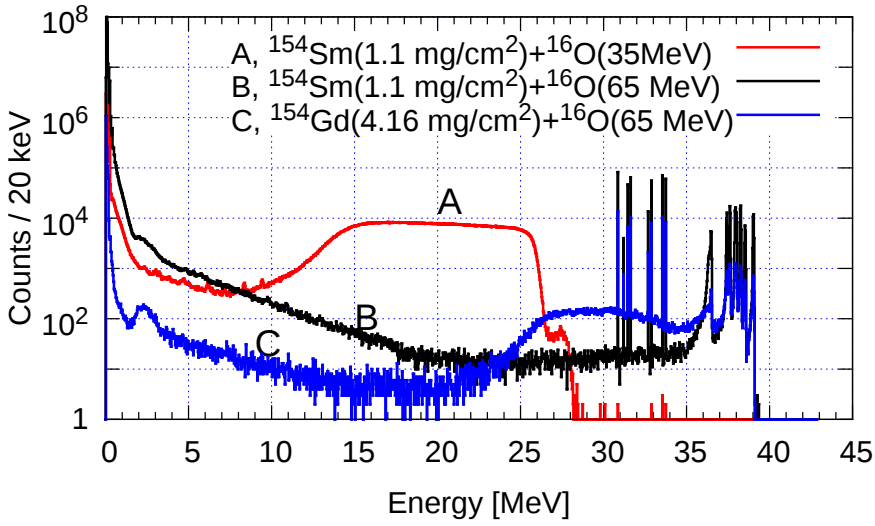

Figure 4.11: Raw silicon detector spectra measured with 35 and 65 MeV beam energies. Note that integration over the backscatter distribution resulting from ^{16}O@35MeV+^{154}Sm reaction gives 6.5×10^6 events.

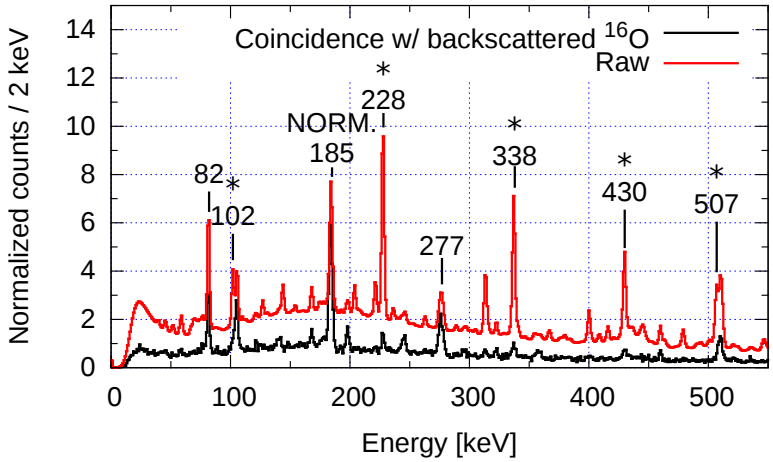

Figure 4.12: A γ-ray spectrum gated with high-energy events compared with the projection of an electron-gamma matrix, normalised with the 185 keV γ-peak intensity. Peaks arising from ^{166}Yb are marked with asterisk. Result from the ^{16}O@65MeV+^{154}Sm reaction.

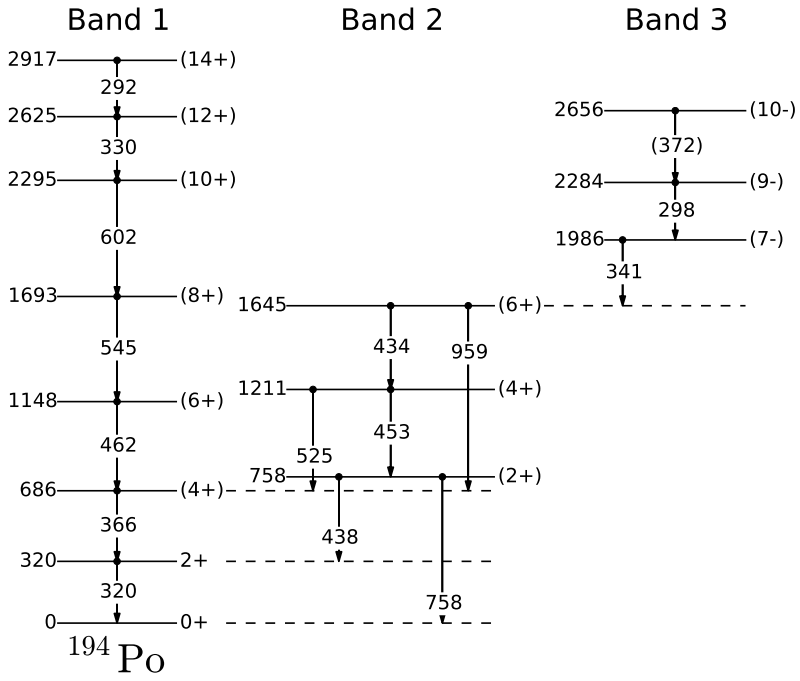

Figure 4.13: Partial level scheme of ^{194}Po. Level and transition energies are taken from Ref. [91] and rounded to nearest value in keV.

4.4 E0 transitions in ^{194}Po

4.4.1 Introduction

In the neutron-deficient polonium isotopes close to the neutron mid-shell of N=104, it is expected that there is a co-existence of spherical and oblate intruder states at low excitation energy. This picture has been supported by a large number of experimental and theoretical studies over the last decade or so (see Refs. [100, 101] for reviews). It is expected that ^{194}Po has a low-lying 0_2^+ band head state that may feed the 0_1^+ ground state through a fully converted E0 transition. In the theoretical work of A. M. Oros [45] the 0_1^+ ground state is expected to be spherical and the first excited 0^+ state to be oblate. It is, however, expected that the oblate structure should become yrast, forming the ground-state band, with the spherical structure forming an excited band. In the work of Oros [45] the level energy of the excited 0_2^+ state is expected to be ~ 240 keV (the value is extracted from figure 13 of Ref. [45]) thus placing the 0_2^+ level energy below the 2_1^+ level. According to the level systematics shown

in figure 4.14 the excited 0_2^+ state should be found between approximately 520 and 310 keV, lying close to or above the 2_1^+ level energy.

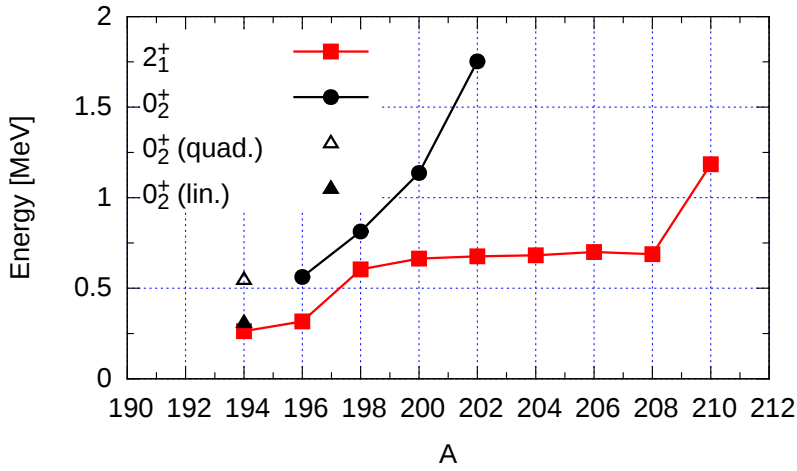

Figure 4.14: Level systematics for even-mass $^{192-210}$Po isotopes with two extrapolated possibilities for the 0_2^+ level at 194 mass. Values are normalised to the 0_1^+ ground state at 0 MeV. The quadratic (quad.) fit is through all of the 0_2^+ points, linear (lin.) only through the two adjacent points.

In the work of K. Helariutta [46] the nature of the bands in ^{194}Po (Bands 2 and 3 in figure 4.13) were investigated using γ-ray spectroscopy. Based on the estimate of unperturbed 2_1^+–0_1^+ transition a deformation parameter of $\mid \beta \mid \sim 0.17$ was deduced for the oblate intruder band (Band 1 in figure 4.13). In the work of T. Grahn [102, 103] the lifetimes of the 4_1^+ and 2_1^+ levels of Band 1 were measured with recoil distance Doppler-shift lifetime measurements allowing the deformation parameter to be deduced as $\sim$0.17. A recent paper by B. Andel [104] describes a measurement performed at GSI with SHIP where several new γ-rays (209, 248, 362, 494 and 847 keV) originating from isomeric states of ^{194}Po were found. In addition to these studies, ^{194}Po has been studied at JYFL through ICE spectroscopy using the SACRED [12] electron spectrometer. The experiment with SACRED is unpublished with some results available online [105]. The main result was the measured ^{194}Po electron spectrum shown in figure 4.15. The data measured with SACRED show an unknown electron doublet at $\sim$120 keV that was speculated to be due to an E0 transition. The possible origin of this doublet and other peaks in the spectrum are discussed later in this chapter. The experiment introduced here incorporates electron spectroscopy, focal plane measurements and prompt γ-ray detection, allowing collection of both alpha-tagged electrons and γ-rays. In principle, this should be sufficient to reveal the position of the proposed 0_2^+ band head. A summary

of the experimental parameters in the latest experiment with SAGE is shown in table 4.6. A partial level scheme of ^{194}Po is shown in figure 4.13.

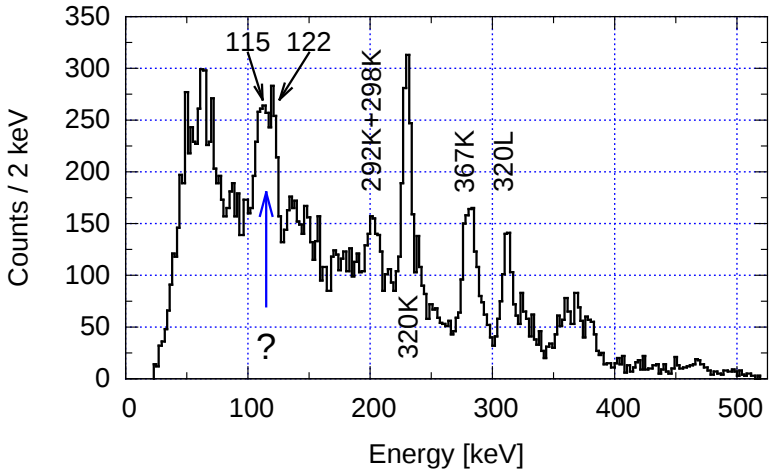

Figure 4.15: A ^{194}Po electron spectrum measured with SACRED. The doublet with unknown origin is pointed out. Figure is reproduced from Ref. [105]

Table 4.6: Summary of the ^{194}Po experiment. Maximum beam which can be tolerated by the target (Max. beam) is calculated using the procedure from Ref. [71].

Beam	Element	^{28}Si	Target	Element	^{170}Yb
	Energy	150 MeV		Enrichment	∼90%[a]
	Beam on target	125 hours		Thickness	320(80) μg/cm^2
	Intensity (ave.)	20 pnA		Max. beam	1 pμA[b]
SAGE	I_{coils}	800 A	DAQ	Trigger	DSSD OR
	$U_{barrier}$	-25 kV			

[a] Based on the γ-ray spectra. [b] RITU He pressure 0.33 mBar.

4.4.2 Experimental details

Recoil decay tagging

In the present measurement the recoil-decay tagging (RDT) methods [106, 107, 108] was used to select prompt ^{194}Po γ-rays and electron. In RDT studies, the data is filtered such that prompt data (SAGE Si and JUROGAMII) is stored to disk if it falls within $\pm 2.5\mu$s of an event from any detector in the focal plane. In the offline sorting the logical OR of timing signals from the DSSD is used to create events of width $\pm 2\mu$s around the triggering event. The first step of the RDT process is to use the time-of-flight (ToF) and energy loss (ΔE) data obtained from the MWPC to create a recoil gate. The ToF-ΔE matrix acquired in this measurement is shown in figure 4.16. The recoil gate is used to separate the true fusion products from scattered beam and target-like ions. The events with identified recoils are stored in a temporary data structure called the "tagger" in the offline sort. If an alpha particle is subsequently detected either in the same or neighbouring pixel in the DSSD as the recoil, the recoil and alpha particle are said to be correlated. Furthermore, the alpha particle can be demanded to have a certain energy and the spectrum of prompt events extracted from such events is called an alpha-tagged spectrum.

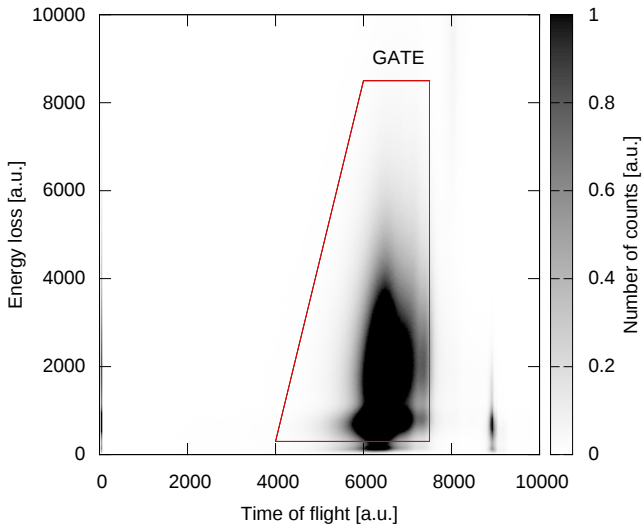

Figure 4.16: A measured time-of-flight versus energy loss matrix from the ^{194}Po experiment. The shape of the distribution is deformed due to issues in the MWPC. The approximate ToF-ΔE gate used in the analysis is shown.

Due to issues with the MWPC the ToF-ΔE distribution has an irregular shape. However, the distribution is not critical as the lower limit can be still set to cleanly select fusion products. An ion passing the recoil gate is labelled as a

fusion product. The recoil time is used to define time gates between prompt events and recoil detection. With a condition that an ion passes the recoil gate the resulting recoil-γ-ray time and recoil-electron time matrices are shown in figures 4.17 and 4.18 respectively. In the recoil-decay tagged spectra shown in this work, the correlation between a ^{194}Po alpha decay and the recoil must be made within a 1.6 s search time (see figure 4.19 for an example correlated alpha spectrum). When creating the γ-γ and γ-electron matrices the events must fall within an interval of [-100:100]ns. The effect of applying the recoil gate, prompt time gates and further the recoil-decay tagging is shown in figure 4.20 for prompt γ-rays and in figure 4.21 for electrons. The resulting γ-γ and γ-electron matrices are very clean. For example, based on γ-γ coincidences the amount of ^{195}Po versus ^{194}Po in the recoil gated matrices is $\sim$0.5 and in alpha-tagged matrices $\sim$0.02.

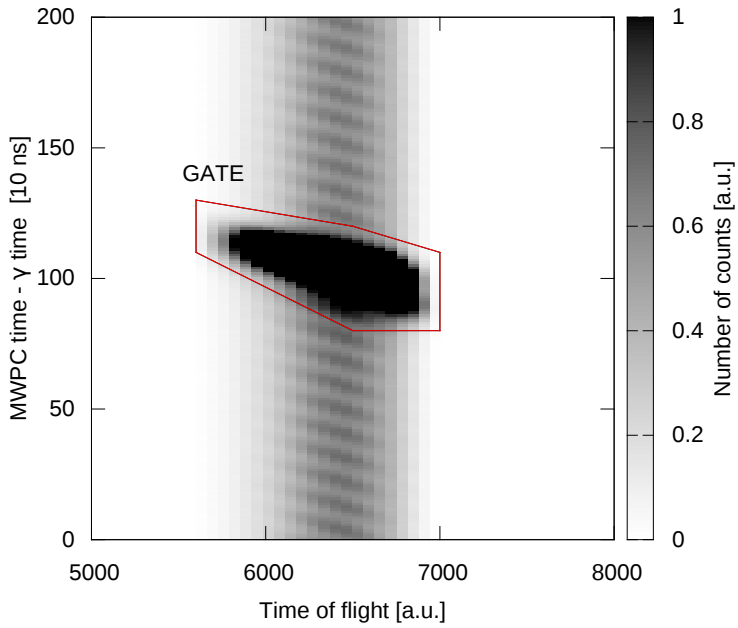

Figure 4.17: Matrix showing measured ToF (MWPC-DSSD) versus MWPC time minus γ-ray time. The γ-ray-recoil time gate used is outlined approximately.

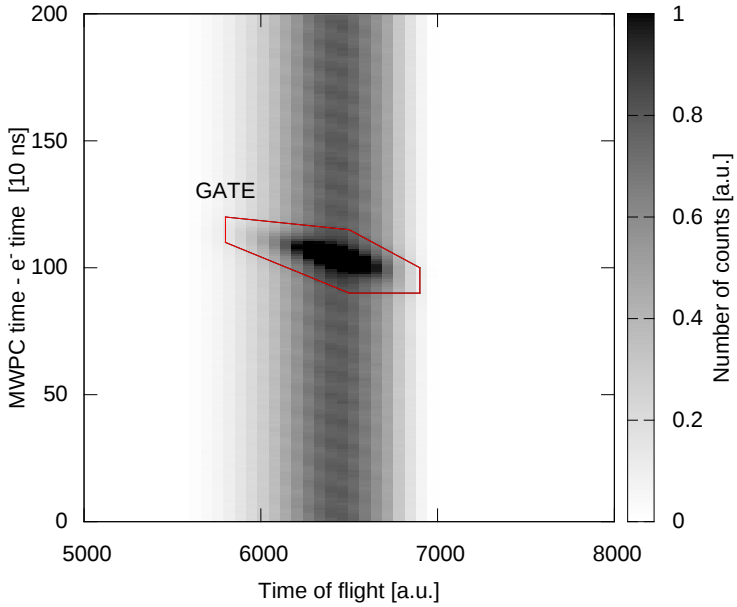

Figure 4.18: Matrix showing measured ToF (MWPC-DSSD) versus MWPC time minus electron time. The recoil-electron time gate used is outlined approximately.

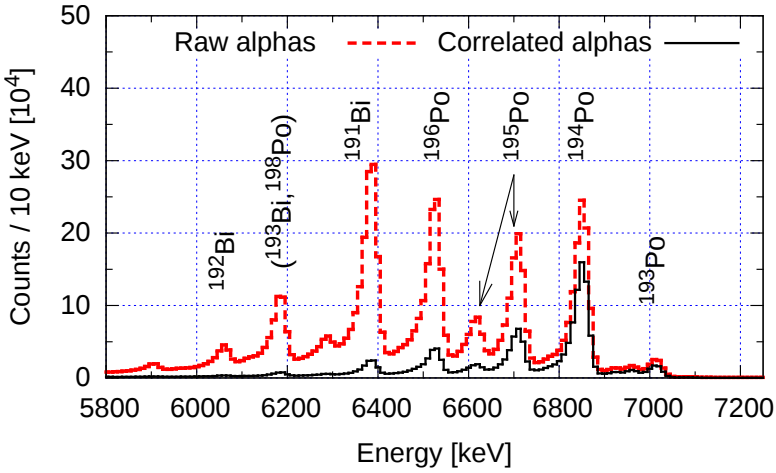

Figure 4.19: Raw alpha particle energy spectrum compared to correlated alpha spectrum with a correlation time of 1.6 s.

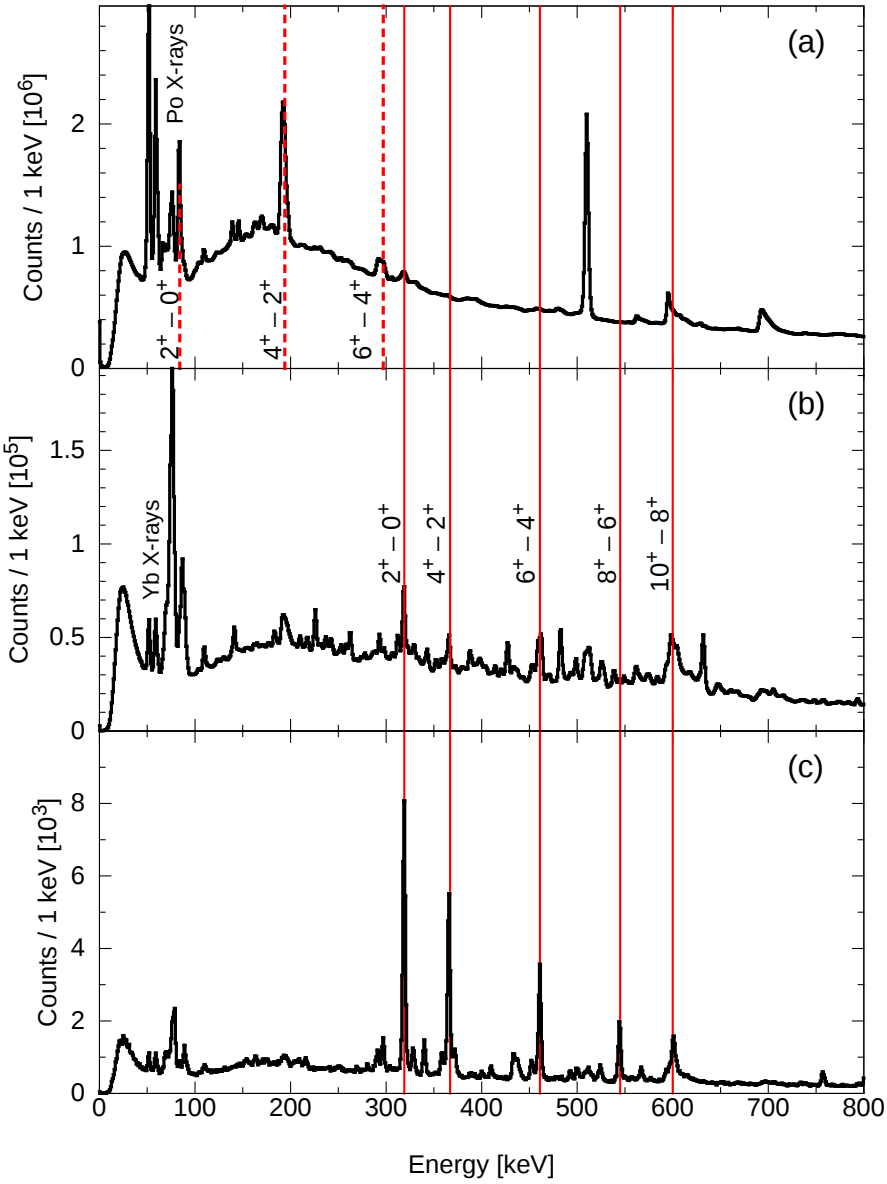

Figure 4.20: Effect of recoil gating and recoil-decay tagging on the prompt γ-ray spectra from the ^{28}Si+^{170}Yb reaction. (a) Raw (b) Addition of recoil and recoil-gamma time gates. (c) As in (b) but with ^{194}Po alpha-tagging. Dashed lines indicate Coulex from ^{170}Yb target, full lines mark the ^{194}Po ground state band.

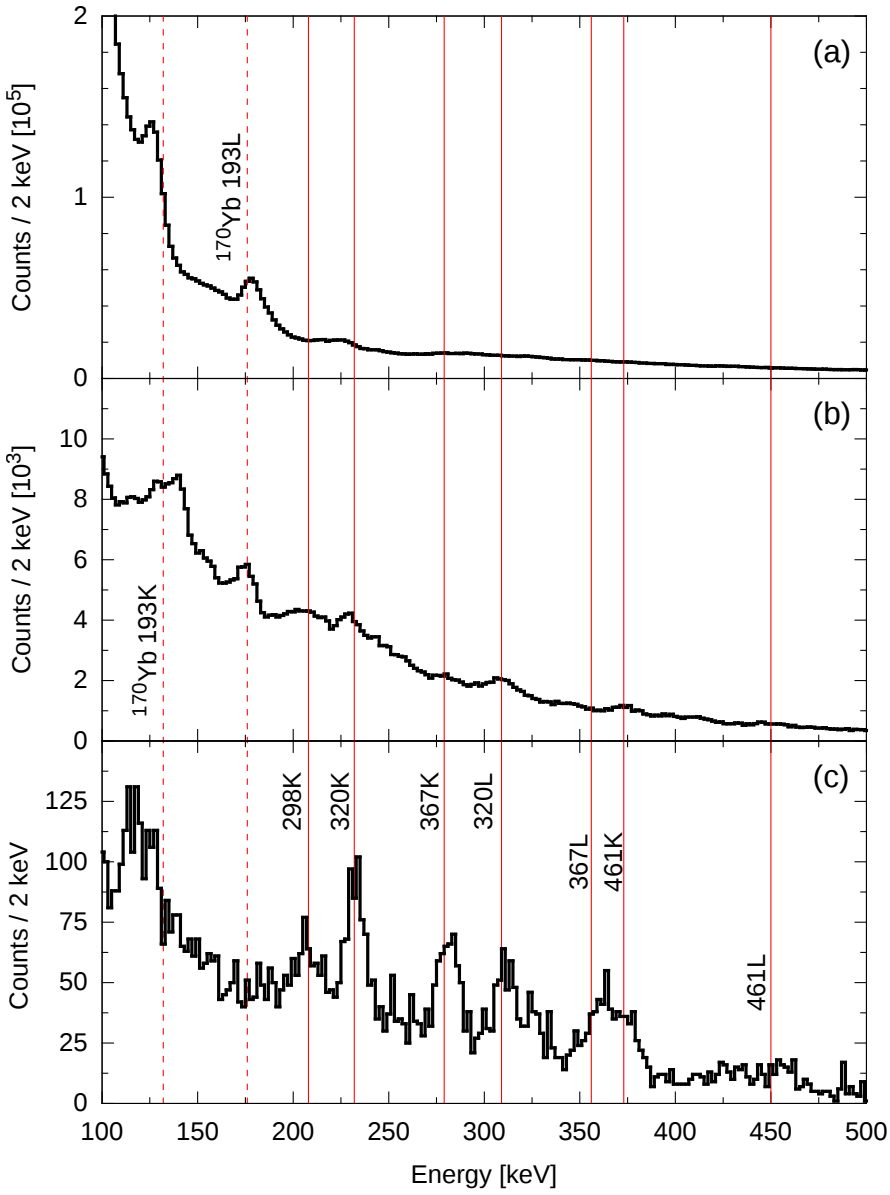

Figure 4.21: Effect of recoil gating and recoil-decay tagging on the prompt electron spectra from the ^{28}Si+^{170}Yb reaction. (a) Raw (b) Addition of recoil and recoil-gamma time gates. (c) As in (b) but with ^{194}Po alpha-tagging. The dashed lines mark conversion from ^{170}Yb ground state band transitions, full lines conversion peaks originating from ^{194}Po ground state band.

Electron detection efficiency

The measured efficiency calibration points and fit through the points is shown in figure 4.22. The analysis of electron data collected for the calibration revealed a comparatively low electron detection efficiency. In addition the calibration points measured before and after the experiment differ in an uncharacteristic manner. It is believed that there may have been an issue with the current feed for the downstream coil during the experiment, which may have reduced the electron detection efficiency. In addition, in the data measured before the experiment the source position is roughly 4 mm away from the magnetic axis based on the measured electron distribution. A similar offset in the electron distribution is present in the in-beam data but electron distribution measured after the experiment is well-centred. Consequently, the efficiency data measured at the beginning of the experiment is used in the data analysis presented.

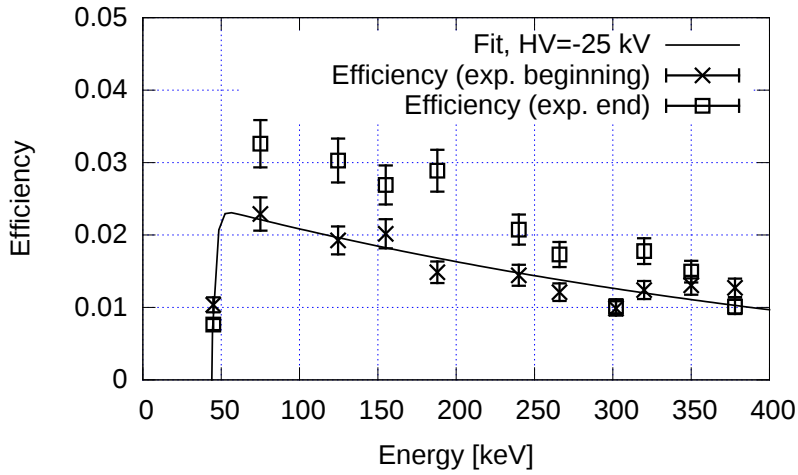

Figure 4.22: Electron detection efficiency before and after the ^{194}Po experiment with I_{coils}=800 A.

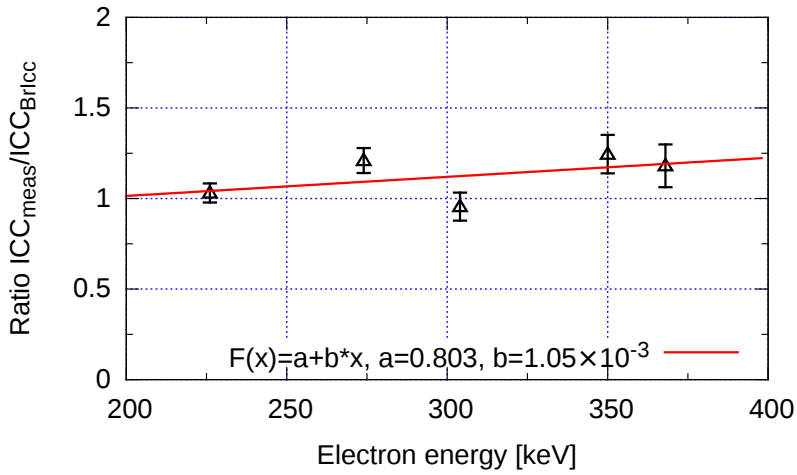

Figure 4.23: Ratios between measured ICCs and calculated values from Ref. [38] for ^{194}Po ground state band transitions.

Internal conversion coefficients

In order to check the validity of the deduced electron efficiency curve and the procedure for determining absolute internal conversion coefficients, the ICCs for the ^{194}Po ground state band E2 transitions were measured. Due to low statistics in the alpha tagged γ-γ and γ-electron matrices these were deduced from alpha tagged γ-ray and electron singles spectra. As can be seen from figure 4.23 the behaviour of the relative conversion coefficient α_{rel} ($=\alpha_{meas}/\alpha_{BrIcc}$) is similar to that with ^{154}Sm raw matrices (see figure 4.6) but closer to unity in general. Example spectra used to extract these coefficients is shown in figure 4.24. The fit shown in figure 4.23 shows a correction coefficient (CF) that is used to scale the measured ICCs to the correct value. Based on the behaviour shown in figure 4.6 the correction factor is assumed to have a constant value of 1.25 between 400 and 500 keV electron energies that are under study later in the text.

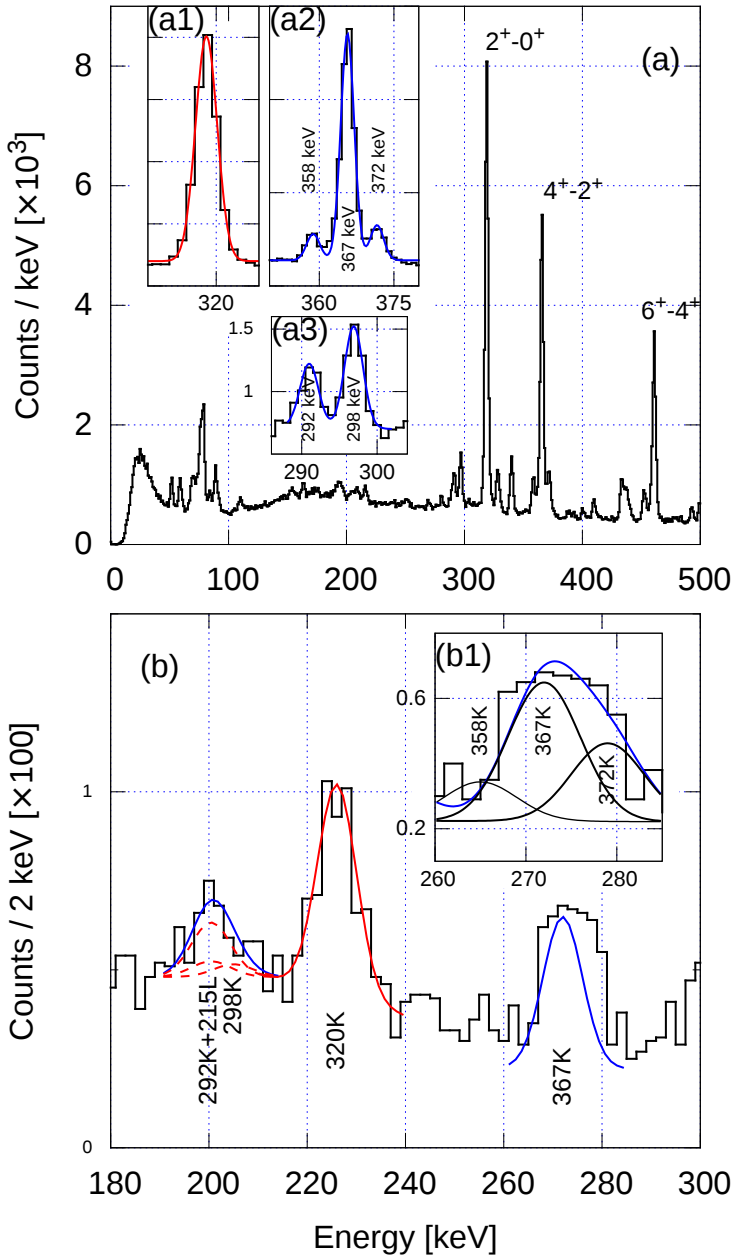

Figure 4.24: Examples of fits that are used to extract the ^{194}Po ground state ICCs. (a) Alpha- tagged γ-ray spectra from JUROGAMII (a1) Peak arising from the ground state band 2_1^+-0_1^+ transition with a fit. (a2) Peak arising from the ground state band 4^+-2^+ transition with a fit containing components from other local peaks. (a3) Peak arising from the 9^--7^- and ground state band 14^+-12^+ transition with a fits. (b) Alpha-tagged electron spectra. The K conversion-electron peaks from the ground state band transitions are fitted. (b1) A full deconvolution of electron spectrum between 260 and 285 keV, contribution from the 367K line is shown in (b).

4.4.3 Results

Mysterious electron peaks

The conversion electron data obtained with SACRED[1] show a structure resembling a doublet electron peak at around 120 keV without clear origin, and also a strong electron peak at about 200 keV. It was speculated that the peak at around 120 keV could be due to the decay and K conversion of a 0_2^+ state to the ground state (0_1^+) with the level energy of around 215 keV. Due to the energy separation and intensity ratios, it was also speculated that the peak at 200 keV could be due to L conversion of the same state. The same structures are detected in the SAGE experiment with similar characteristics as seen in figure 4.25. With SAGE, γ-rays coincident with the electrons are measured and a more thorough investigation of the origin of the structures can be made. First, possible contributions from the background are considered by extracting the random coincidence events. The alpha decay-tagged γ-rays falling into the recoil-γ time gate and passing the γ-γ time gate result to the matrix projections shown in figure 4.26. The events *not* falling into the γ-γ time gate but still passing the recoil-γ time gate reveal an interesting γ-ray peak at 193 keV. The energy of the background peak matches the energy of the $4^+ - 2^+$ transition of ^{170}Yb that is used as the target. As seen in figure 4.26 the 193 keV peak is present also in the accepted spectra and could therefore contribute to the unknown doublet. However, the energy of the 193K (132 keV) conversion peak is just above the higher energy component of the unidentified doublet shown in figure 4.25 and may contribute to the background below the doublet but cannot contribute as a component in the doublet. If the ^{194}Po alpha-tagged spectra are considered, one of the newly assigned ^{194}Po peaks in Ref. [104] is at 209 keV. The K conversion of this transition would have an energy of 116 keV and be at the correct energy to be the low energy component of the doublet. With the assumption that the 209 keV transition is of E2 character, the conversion would yield only roughly one tenth of the demanded peak intensity. With M1 character the resulting K conversion peak intensity would match the expected intensity. In the γ-ray spectra there are unknown transitions with energies of 206 and 215 keV. The 206 keV transition is much wider than the 209 and 215 keV transitions and is assumed to be arising from background. If the 215 keV transition is assumed to originate from ^{194}Po and to have M1 character, the K conversion from this peak would explain the higher energy component of the doublet. A more detailed analysis of the peak intensities related to the doublet is shown in table 4.7. Note that the ICC correction factor shown in figure 4.23 is taken into account when peak areas are calculated. Fits associated with the analysis are shown in figure 4.27. Neither of the 209 or 215 keV peaks is in clear coincidence with any transitions other than the strongest transitions in ^{194}Po and the placement of these transitions in the level scheme has not been possible. Note that the 372 keV transition (tentative 10_1^--9_1^-) has an α_K of 0.20(2) based on the fits shown in figure 4.24 and can be assigned as a M1 type

[1]The same beam with 143 MeV energy, same target material.

transition (Theoretical values with BrICC α_K(M1)=0.23,α_K(E2)=0.04). Similarly, the 292 keV peak has an α_K of 0.12(4) and the 298 keV an α_K of 0.04(1). If the pure M1 ICCs shown in table 4.7 are scaled down to reproduce exactly the measured peak areas then α_K values of 0.7(1) and 0.9(1) are necessary for the 209 and 215 keV transitions, respectively.

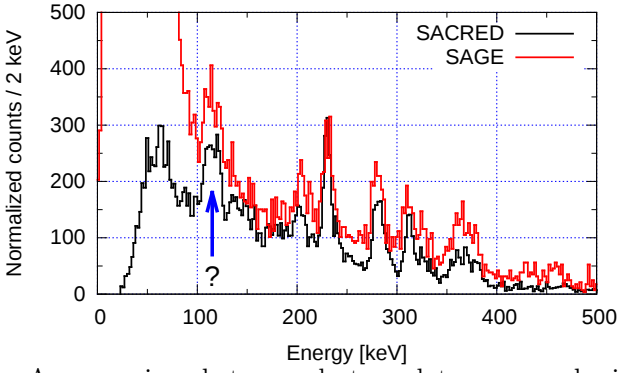

Figure 4.25: A comparison between electron data measured with SACRED and SAGE with alpha tagging. The electron doublet with an unknown origin is indicated. The SAGE result is scaled up to match the 320K peak area.

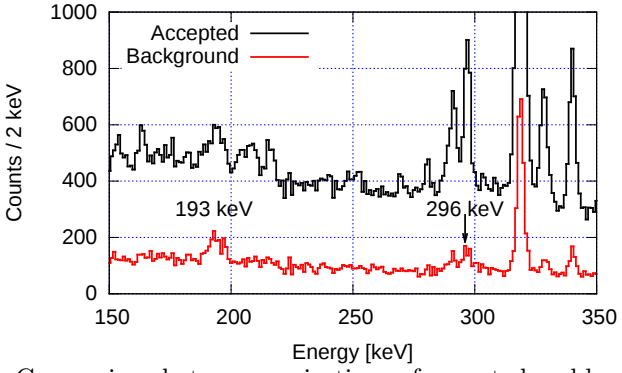

Figure 4.26: Comparison between projections of accepted and background γ-γ matrices. The peaks from $4^+ - 2^+$ (193 keV) and $6^+ - 4^+$ (296 keV) transitions of ^{170}Yb are labelled.

Table 4.7: Peak area (p.a.) estimations related to the observed electron doublet peak. Calculated value (Calc. p.a.) is a sum of the two calculated components, measured peak area (Meas. p.a.) is integrated from the electron spectrum.

Origin	E_γ [keV]	γ-ray p.a.	Type	Eff. γ	α_K [a]	Eff. $e-$	e^- p.a.	Calc. p.a.	Meas. p.a.
^{194}Po	215	1100(40)	E2	.073	.142×.92	.024	47(2)	75(6)	410(20)
^{194}Po	209	600(100)	E2	.073	.151×.92	.024	28(5)		
^{194}Po	215	1100(40)	M1	.073	1.032×.92	.024	340(20)	540(40)	410(20)
^{194}Po	209	600(100)	M1	.073	1.116×.92	.024	203(34)		

[a] With the ICC correction factor from figure 4.23.

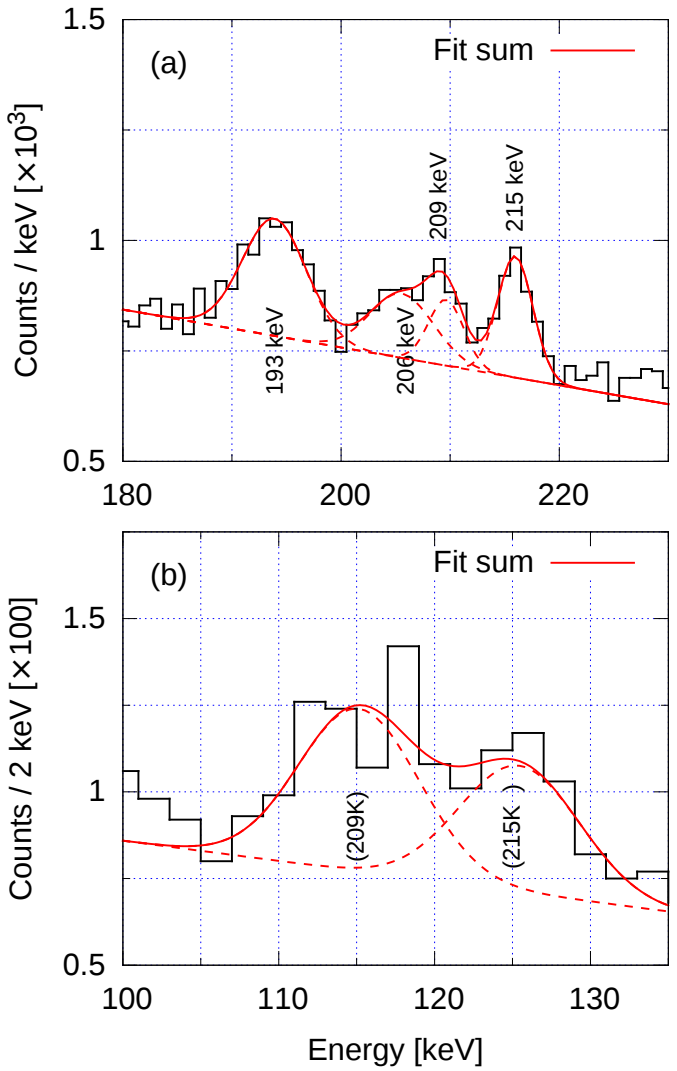

Figure 4.27: Example spectra tagged with the ^{194}Po alpha decay. (a) γ-rays. (b) Electrons. The 193 and 206 keV γ-ray transitions have roughly double the peak widths compared to the 209 and 215 keV transitions and are assumed to be originating from Coulex thus not contributing to the doublet. The structure and intensity of the doublet structure can be explained if both 209 and 215 keV transitions have M1 character.

Search for 0_2^+ level and E0 transition

A partial level scheme of ^{194}Po is shown in figure 4.13 and the lowest levels are reproduced in figure 4.28, which will be discussed in the following . Based on this scheme, the transition feeding the unknown 0_2^+ state (2_2^+-0_2^+) should be in coincidence with the 4_2^+-2_2^+ transition but not with the 2_2^+-2_1^+ transition. As can be seen from figure 4.29 after gating with the 4_2^+-2_2^+ (454 keV) transition a clear candidate peak appears at 494 keV. This corresponds to one of the new transitions belonging to ^{194}Po presented in Ref. [104]. Note that a transition with the same energy is listed in Ref. [46] but assigned to ^{195}Po. However, in the present work γ-γ coincidences do not reveal a 388 keV transition that should be in coincidence [91] with the 494 keV transition if the origin is assumed to be ^{195}Po. A partial level scheme with γ-ray intensity ratios deduced from the alpha-tagged γ-ray singles spectrum is shown in figure 4.28.

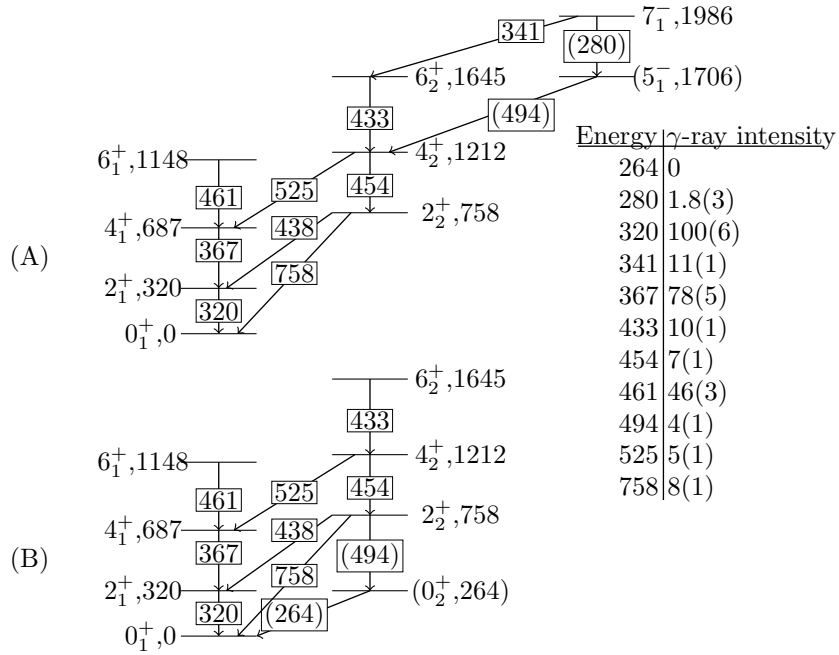

Energy	γ-ray intensity
264	0
280	1.8(3)
320	100(6)
341	11(1)
367	78(5)
433	10(1)
454	7(1)
461	46(3)
494	4(1)
525	5(1)
758	8(1)

Figure 4.28: Partial level schemes of ^{194}Po with two possible placements of the 494 keV transition and relative γ-ray intensities. Level and transition energies are in keV. The alpha-tagged γ-ray transition intensity is efficiency corrected and normalised to the intensity of the 320 keV peak (=100). Later in the text it is argued that scheme A is more likely to be correct.

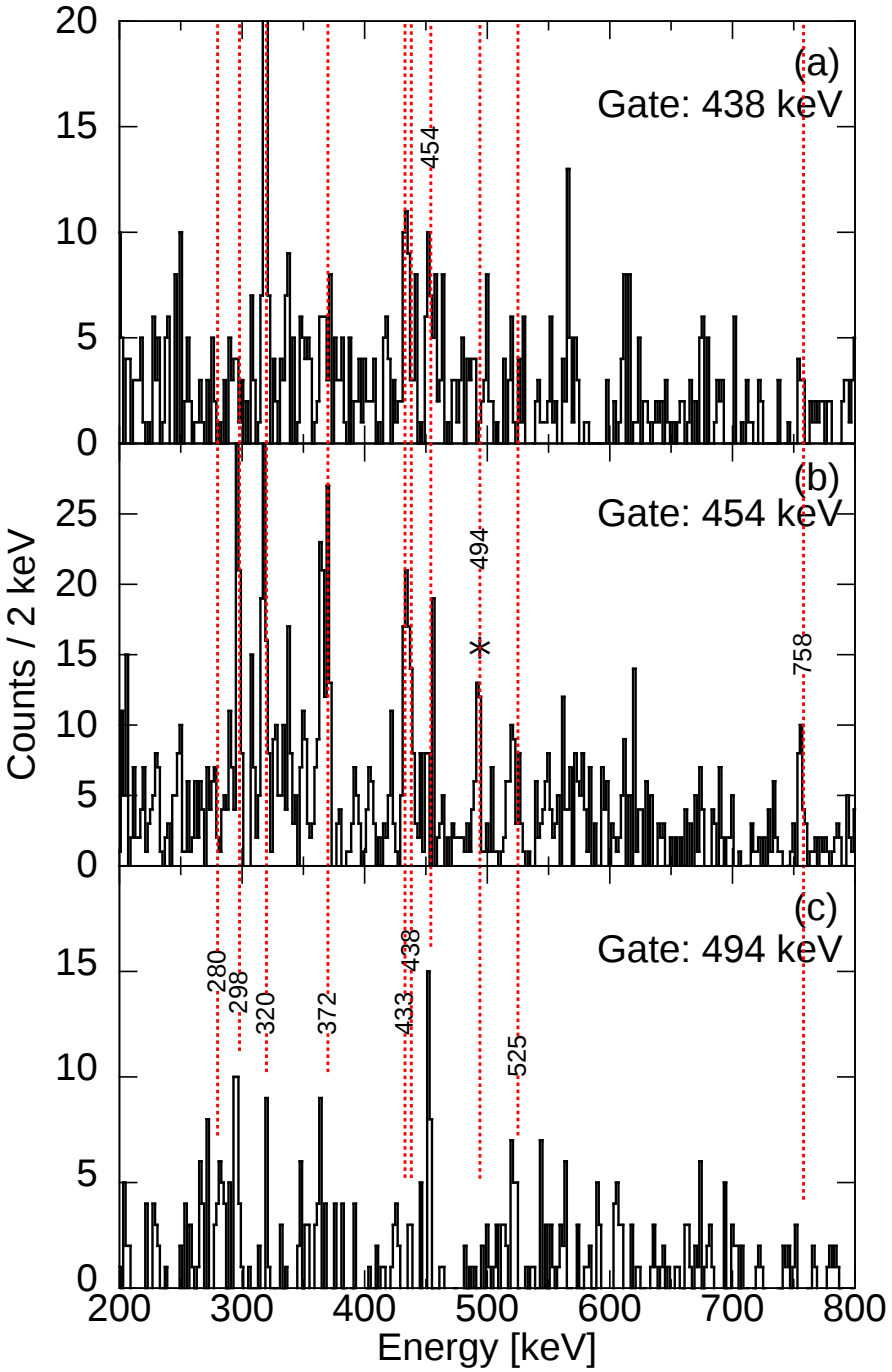

Figure 4.29: Background subtracted γ-ray energy spectra projected from the alpha-tagged γ-γ matrix (a) Gate 2_2^+-2_1^+ (438 keV) (b) Gate 4_2^+-2_2^+ (454 keV). The new transition at 494 keV is marked with an asterisk. (c) Gate at 494 keV. Dashed lines indicate the known side band transitions.

The coincidence between the 454 and 494 keV transitions is clear. If the 494 keV transition is placed between the 2_2^+ and 0_2^+ levels (scheme B in figure 4.28) the 0_2^+ level energy would be 264 keV. No transition with this energy is observed in the 494 keV gated γ-ray spectrum, further supporting the assignment. The resulting 264 keV E0 K and L conversion energies would be 171 and 248 keV, respectively. No 264 keV transitions are observed in the γ-γ matrices and

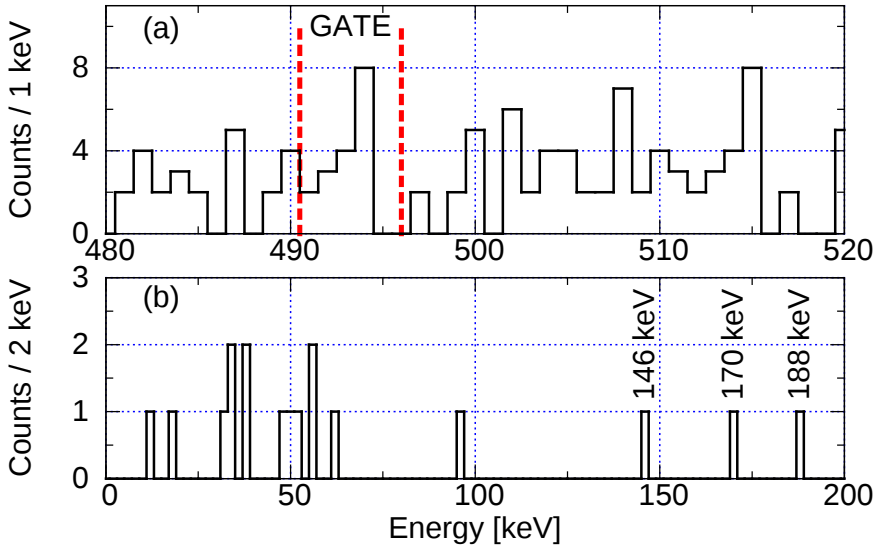

Figure 4.30: Alpha-tagged γ-electron matrix (a) A section of γ projection with the 2_2^+-0_2^+ (494 keV) gate indicated. (b) The resulting gated electron spectrum. No electrons were detected above energy of 188 keV.

therefore the 0_2^+ level assignment resulting in a fully converted E0 transition to the ground state is possible. Gating with 494 keV γ-rays in the ^{194}Po α-tagged γ-electron matrix results in the electron spectrum shown in figure 4.30b. One electron is detected with an energy corresponding to the E0 K conversion energy. In this experiment the typical electron detection FWHM is 9 keV resulting in σ of 3.8 at these energies. This means that all the other electrons in figure 4.30b fall outside the acceptable energy limits and cannot be accepted as E0 conversion electrons originating from the proposed 0_2^+ level. However, if the γ-ray intensities are taken into account, the assignment of the 494 keV γ-ray as the 2_2^+-0_2^+ transitions is questionable. Firstly, if the feeding and depopulation of the 2_2^+ state is considered there is a clear problem. Only one transition (454 keV) with intensity of 7(1) feeds the 2_2^+ state but three transitions (438, 758 and 494 keV) with total intensity of 19(2) depopulate the level. If we assume that the 494, 758 and 438 keV transitions have total ICCs less than 0.2, the 454 keV transition should have an ICC of the order of $\sim$1 to explain the missing intensity. It is shown later in this work that the total ICC of the 454 keV transition

is much less than 1. Secondly, if the intensities of the 494 and 320 keV γ-ray transitions are considered, with assumption that there is no side feeding and the electron detection efficiencies are roughly the same, the resulting relative 320K ($\alpha_K = 0.06$) conversion peak intensities would be 100(6)×0.06=6.0(4), and the 264K intensity would be ($\Omega_K/\Omega_L = 0.8$) 4(1)×0.8=3.2(8) meaning, that the intensity of the possible E0 264K (171 keV) peak should carry about 50% of the intensity of the 320K line. Clearly, it is seen from figure 4.21c that the ratios between electron peak areas do not match, the 171 keV electron peak is not clear and has the maximum upper limit area of ∼2 in relative units. Therefore, the 494 keV transition cannot be the 2_2^+-0_2^+ transition and the placement of the 0_2^+ level remains unclear. If the 494 keV transition is assumed to be feeding the 2_2^+ level (scheme A in figure 4.28) the population/depopulation scheme is much more agreeable. There are two transitions feeding the 2_2^+ state (454 and 494 keV) with total relative intensity of 11(2) and two depopulating transitions with total relative intensity of 15(2). In this case the 494 keV transition would most likely originate from a Band 3 level with negative parity and be of E1 type with a very small ICC. Tentatively this is supported by the fact that the 494K conversion line at 401 keV is missing or undetectably weak in figure 4.21. In addition there are traces of a 280 keV transition (see figure 4.29c) in coincidence with the 494 keV transition that might be the transition between 7_1^- and (5_1^-) levels. Note that in figure 4.30b the 188 keV electron is detected exactly at the energy expected from 280 keV K conversion.

Inter band transitions

The inter band transitions between the same spin and parity states carry information about the configuration mixing. In the present study of ^{194}Po there are two transitions of interest, the $4_2^+ - 4_1^+$ transition with an energy of 525 keV and the $2_2^+ - 2_1^+$ transition with an energy of 438 keV. The peak areas of these peaks in the ^{194}Po α-tagged γ-ray spectra are deduced with Gaussian fits shown in figures 4.31a1 and 4.31a2 (figure is at the end part of this section due to typesetting limitations). The conversion electron peak areas of these transitions, measured from the alpha-tagged spectrum shown in figure 4.31b, are estimated with two different methods. First, with the 438K conversion, fits with different background, common peak widths, fit limits and small variations (±1 keV) in peak positions, initially fixed by the γ-ray energies, were made and the given value is calculated with an average peak area given by the fits. Contrary to common procedure of fixing the peak width to value obtained from source measurement, the peak width is used as a fit parameter. One of the resulting fits is shown as an example in figure 4.31b. The 525K electron peak area is given by a best fit (shown in figure 4.31b1) with neighbouring peaks taken into account. The resulting K conversion coefficients for the 438 and 525 keV transitions with this fit method are 0.15(6) and 0.04(3), respectively. Secondly,

an integration over the expected peak width is made and contributions from the neighbouring peaks are subtracted according to the measured γ-ray intensities with Gaussian distributions. Subtracted peak areas deduced from the γ-ray intensities are shown in tables 4.8 and 4.9. With the integration method, the resulting K conversion coefficients for the 438 and 525 keV transitions are 0.16(2) and 0.04(2), respectively. The measured conversion coefficients are in general agreement with missing γ-ray intensity values reported in Ref. [46] that are 38(20)% for the 438 keV transition and 8(33)% for the 525 keV transition. Note that in figure 4.31b the 454K conversion peak at 361 keV is at most as large as the fitted 438K peak and cannot result in an ICC of $\sim$1. Such a value would require a 454K peak intensity roughly five times larger than is observed. In the following analysis, average values of the ICC obtained with the different methods are used.

Table 4.8: Peak areas related to the 438K electron, deduced using the integration method. The measured correction factor from figure 4.23 (CF) is taken into account. M+ notation refers to a higher order (MNOP...) conversion.

Peak: 438K / 345 keV 3σ integration limits: [330:360] keV Counts above background: 263							
Transition	Energy [keV]	γ-ray p.a.	Type	α $\times$CF	e- Eff.	Fraction	Counts
434K	341	38300	E2	0.03$\times$1.16	0.011	1	15
367L	351	309650	E2	0.02$\times$1.17	0.011	1	80
367M+	363	309650	E2	0.006$\times$1.17	0.011	0.3	7
372L	356	47000	M1	0.04$\times$1.17	0.011	0.8	19
372M+	368	47000	M1	0.012$\times$1.17	0.011	0.1	1
359L	342	21660	M1	0.04$\times$1.16	0.011	1.0	11
359M+	355	21660	M1	0.014$\times$1.16	0.011	0.8	3
454K	361	27200	E2	0.03$\times$1.17	0.011	0.5	5
						Sum:	141
					Total	438K:	122

Table 4.9: Peak areas related to the 525K electron, deduced using the integration method. The measured correction factor from figure 4.23 (CF) is taken into account. The total contribution within the integration limits from the higher order conversion (M+) is deduced to be 4 counts.

Peak: 525K / 432 keV 3σ integration limits: [415:445] keV Counts above background: 45							
Transition	Energy [keV]	γ-ray p.a.	Type	α ×CF	e- Eff.	Fraction	Counts
438L	422	27160	M1	0.026×1.25	0.009	0.9	7
454L	438	27200	E2	0.01×1.25	0.009	1	3
545K	452	115800	E2	0.019×1.25	0.009	0.2	5
462L	446	182500	E2	0.01×1.25	0.009	0.5	8
434L	418	38300	E2	0.01×1.25	0.009	0.5	2
M+	-	-	-	-	-	-	4
						Sum:	29
					Total 525K:		16

An attempt to deduce the mixing ratios of the 438 and 525 keV transitions were made as presented in sections 3.17 and 4.2 but the result was inconclusive, thus adopted values are used in the calculations. Together with an estimate of the E2 transition rate, this would have allowed a calculation of $\rho^2(E0)$ to be made, according to equation 2.36. As neither the mixing ratio or lifetimes are available, representative values for δ of 1 and 10 are used to calculate the expected ICCs for mixed M1+E2 transitions shown in table 4.10. The measured ICC for the 438 keV transition approaches that for a pure M1 transition, whilst that for the 525 keV transition is compatible with that of a mixed M1+E2 with a value of δ close to 1. This suggests that there may be a significant E0 component in the $2_2^+ - 2_1^+$ transition.

Table 4.10: Measured ICCs compared with calculated mixed ICCs of the inter band transitions with different adopted multipole mixing ratios.

J_i^π-J_f^π	$\alpha_{K,exp.}$	α_K M1	α_K E2	$\delta_{adopt.}$=1 $\alpha_K(M1+E2)$	δ_{adopt} =10 $\alpha_K(M1+E2)$
2_2^+-2_1^+	0.16(7)	0.15	0.03	0.0885	0.0304
4_2^+-4_1^+	0.04(4)	0.1	0.02	0.0557	0.0208

Table 4.11: Summary of the measured ICC values for transitions in ^{194}Po. The ground state band transitions are omitted as they are assumed to be in agreement with BrIcc values.

Transition J_i^π-J_f^π	γ-ray energy [keV]	e- energy [keV]	Character	Orbit	ICC
?	209	116	(M1)	K	0.8(1)
?	215	122	(M1)	K	0.9(1)
(10_1^-)-(9_1^-)	372	279	(M1)	K	0.20(2)
(14_1^+)-(12_1^+)	292	199	(E2)	K	0.12(4)
(9_1^-)-7_1^-	298	205	(E2)	K	0.04(1)
2_2^+-2_1^+	438	345	(M1)	K	0.16(7)
4_2^+-4_1^+	525	432	(M1+E2)	K	0.04(4)

4.5 Summary of the ^{194}Po results

Despite some experimental difficulties several details of ^{194}Po were successfully studied. The analysis of the γ-γ data allows a placement for one of the newly assigned ^{194}Po transitions to be proposed and gives hints about a new, coincident, transition with 280 keV energy. Based on energy level systematics, the 280 keV transition is tentatively placed between 7_1^- and (5_1^-) levels.

The ICCs of several transitions in ^{194}Po were successfully measured. In some cases the measured ICCs allow tentative level assignments to be made firm, or give insight into the character of the transition. A summary of the measured ICCs is given in table 4.11. The ICCs measured for the inter band transition between same spin and parity states (2_2^+-2_1^+ and 4_2^+-4_1^+) are in good agreement with results given in Ref. [46].

The main goal of the experiment, finding the elusive 0_2^+ level, was not achieved. Due to various problems, the analysis of the γ-electron coincidence data could not give more information about the matter as the statistics in this data set were very low. In all, some good results were obtained but there is a lot of room for improvement a.k.a the experiment should be ran again. However, the main features of the SAGE and SACRED electron spectra could be explained with aid of simultaneous γ-ray detection.

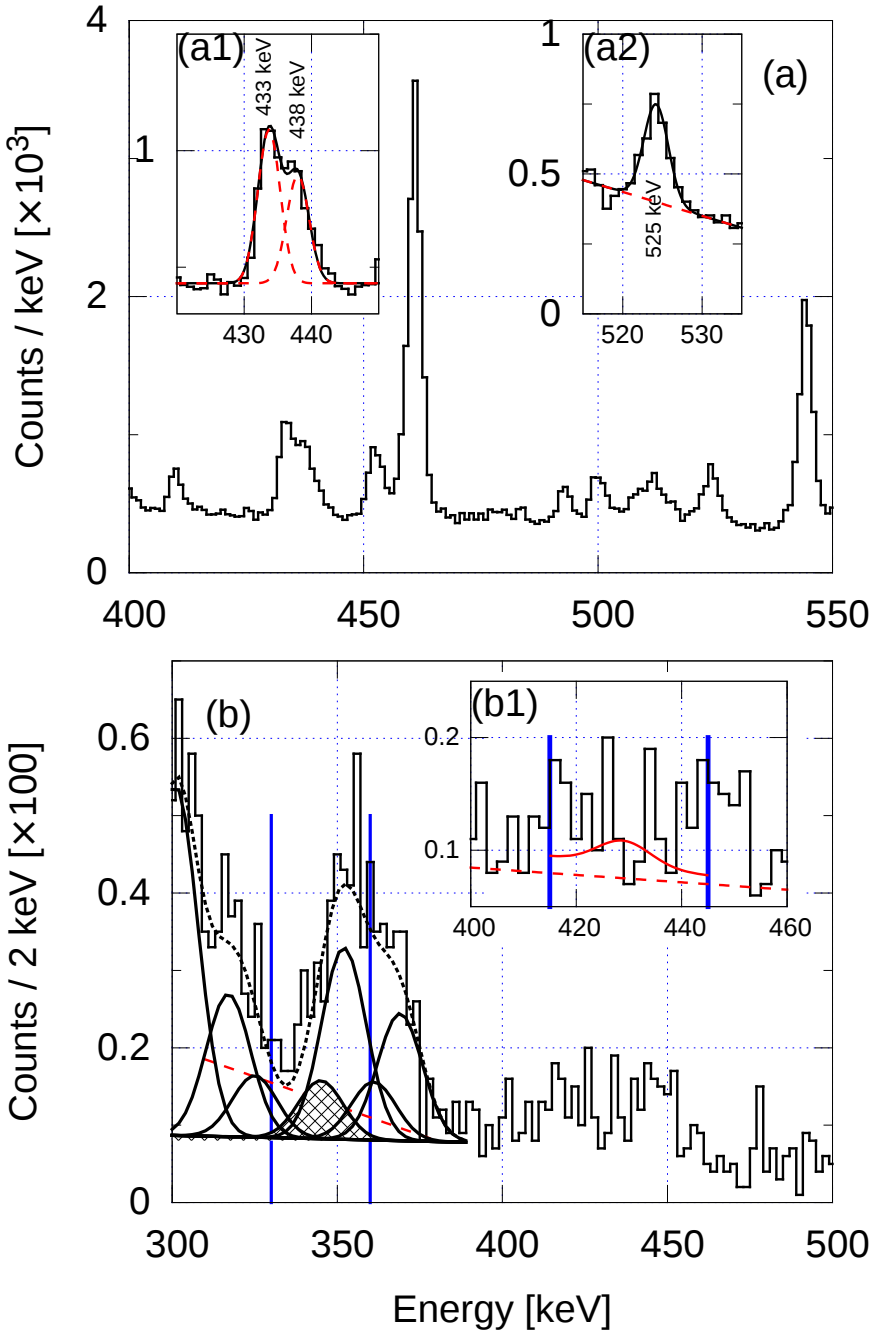

Figure 4.31: Alpha-tagged γ-ray and electron singles. Vertical lines denote the integration limits, dashed lines indicate the background used with the integration. (a) Partial γ-ray spectrum with fits to the $2_2^+ - 2_1^+$ transition with an energy of 438 keV (a1) and to the $4_2^+ - 4_1^+$ transition with energy of 525 keV (a2). (b) Partial electron spectrum with dotted line showing the best fit to data. Component peaks are shown below the best fit, filled peak marking the 438K conversion peak contribution.(b1) Best fit of the 525K conversion line.

Chapter 5

Discussion

5.1 Effect of the analysis tools developed

It was a great surprise that the very simple sounding task of extracting correct internal conversion coefficients from data measured with the SAGE spectrometer proved difficult. In the papers discussing measured conversion coefficients [88, 95] the measured values were normalised to those from known sources. In a recent conference proceedings paper [109] directly measured absolute ICCs are presented but in this case time gates were selected so that the ICCs at the energy range under investigation are produced correctly.

The time gate definition procedure presented in section 3.16 solves the problem in general. However, the method is not without drawbacks. It is clear that restricting the time gates can lead to lower statistics and the detection of low-intensity peaks becomes a more difficult process. This is shown in section 4.2 where the E0 transition strengths in ^{154}Sm are calculated. In several of the cases presented in this work only an upper limit could be given contrary to the case where the NPG method was utilized with the same dataset [88].

At first glance, the add-back procedure presented in section 3.14 seems very promising. Under closer inspection the resulting sum spectrum contains false secondary peaks below the true full energy peaks (see figure 3.48). The only feasible origin of these false peaks is a significant inactive volume within the Si-detector between the detector segments. Even though the add-back algorithm cannot be used to recover energy without care it can be used to veto scattered events and thus improve the spectral quality.

The effect of radial filtering presented in section 3.12 is limited, if one only

considers the singles spectrum. The main gain of the filtering is a significantly smaller amount of data to be processed during analysis, and a significant reduction of coincidence events. For example, the number of electrons in the γ-electron matrix used to determine ICCs in ^{154}Sm is reduced by $\sim$40% when the low-energy background is removed with the radial filter. The maximum radius function (Eq. 3.15, Fig. 3.43) behind the radial filtering may yet prove to be very useful. If the segmentation layout of the Si detector could be changed to be beam axis centred rather than magnetic axis centred a rough estimate of the emission angle of the electrons could be given. This would allow more precise Doppler correction and possibility for electron-γ angular correlation measurements.

The angular correlation method used to determine mixing ratios is not new, but rarely used with JUROGAMII. Usually a simplified form of it called directional anisotropy is used. The angular correlation yields very good results with source data (see section 3.17) but in the experimental conditions proves more challenging due to lower statistics. Most of the mixing ratio results for ^{154}Sm and ^{194}Po are considered to be tentative and are therefore not used in the determination of other quantities.

5.2 Results from the experiments

As stated previously, the results obtained for the transition strengths of ^{154}Sm in this work are not as good as might be expected due to time gate restrictions and the resulting reduction in statistics. Overall, the results presented in table 4.5 are consistent with literature values. Furthermore, the ^{154}Sm experiment was divided into two parts with different beam energies and in the latter part from which the results in this work are derived some contamination from beam hitting the target holder was present. From the seven days of beam time only one fifth is effectively analysed in this work. Note that in the analysis of Ref. [88] it was possible to retain a larger part of the data, reaching an effective beam time of one third of a week.

The latter part of the experimental chapter discusses spectroscopy of ^{194}Po. The main goal of the experiment was to establish the presence of the second 0^+ state. Earlier experiments [46, 105] had failed to locate the feeding 2_2^+-0_2^+ transition and tentatively assigned an electron peak originating from the 0_2^+-0_1^+ E0 transition. In a recent study [104] a set of new γ-transitions are assigned to ^{194}Po. One of these (209 keV) together with a neighbouring 215 keV transition (see figure 4.27) explains the electron peak present in the SACRED data. Another of the new transitions (494 keV) was considered as a candidate for the 2_2^+ to 0_2^+ transition thus giving the exited 0_2^+ level energy. However, a more detailed analysis places the transition, most likely, as an intraband

transition between (7_1^-) and (5_1^-) states. Unfortunately in the current work the electron detection efficiency was lower than expected and room for improvement still exists.

The determination of the monopole transition strengths of I_2-I_1 transitions via the relevant ICCs was a secondary goal of the ^{194}Po measurement. The measured ICCs for these type of transitions are roughly consistent with the earlier measurements presented in Ref. [46]. As the determination of the mixing ratio of these transitions resulted only inconclusive results the monopole transition strengths cannot be deduced. Again the lower than expected electron detection efficiency made it extremely difficult to determine internal conversion coefficients for these transitions. Future experiments, aimed at determining the values of δ and the E2 transition strengths (for example via Coulex at ISOLDE) may allow the results obtained here to be further interpreted.

5.3 Future of the SAGE spectrometer

From the technical point of view, the most immediate improvement will be the introduction of a 1.5 mm thick Si-detector in the near future[1] that will improve the electron detection efficiency above 500 keV. After the introduction of the thicker detector the usage and more detailed understanding of the add-back algorithm becomes more crucial. There are plans to exploit the backscattered ions (see section 4.11) in Coulomb excitation measurements. As can be seen in figure 4.12, a coincidence with backscattered ions removes the background from unwanted fusion products from the Coulex data. If the systematic study of nuclei near N∼90 is continued the main experimental method will be Coulomb excitation and the gating/vetoing methods to reduce background will be valuable. In addition to the method itself technical modifications allowing more efficient detection of the backscattered ions are being considered. For example, adding loops of plastic optical fibre [99] in the Si detector chamber or in the target chamber is under consideration.

[1] R-D. Herzberg, personal communication

Appendices

Appendix A

Target thickness study

A.1 Motivation

During an experiment[1] with the reaction ^{203}Tl(^{48}Ca@219 MeV,2n)^{249}Md it was noted that the production yield was dropping for no clear reason. Usually this is an indication that the target has been somehow damaged. After the experiment the target showed clear damage to the naked eye. A more detailed analysis was made in order to quantify the level of damage with the help of X-ray tomography. Note that other targets have been studied in a similar manner but in the Tl case the effect is the most prominent.

A.2 Procedure

A Xradia (ZEISS) microCT-400 located in the JYFL tomography laboratory was used to probe the target [2]. This study was performed in a very simplified way with just plane images taken through the target. In the thickness analysis the intact part of the target is taken as a reference (see figure A.1 left). An average penetration over the marked area is determined to be 0.94 in the reference case. In this case the intact target area has a surface density of 300 μg/cm^2 and the total surface density of the carbon layers suspending the Tl is 30 μg/cm^2 according to the manufacturer. With these details the material specific linear attenuation constant μ can be calculated from the general attenuation law

$$I = I_0 Exp[-\mu s/\rho] \tag{A.1}$$

[1] PAC experiment number S15.

[2] Images are produced with help of Mr. J.Parkkonen and Dr. T.Turpeinen.

where I is the number of detected X-rays, I_0 is the number of incident X-rays, μ is the linear attenuation constant, s is the surface density and ρ the density of the material (Tl: 11.85 g/cm^3). By using the reference surface density and measured penetration from the area shown in figure A.1 right, the μ_{ref} is calculated to be 2445 cm^{-1}. The average penetration over the center part of the target is measured to be 0.99. By using μ_{ref} this yields a surface density of 50 μg/cm^2 showing that the target was significantly thinned during the experiment.

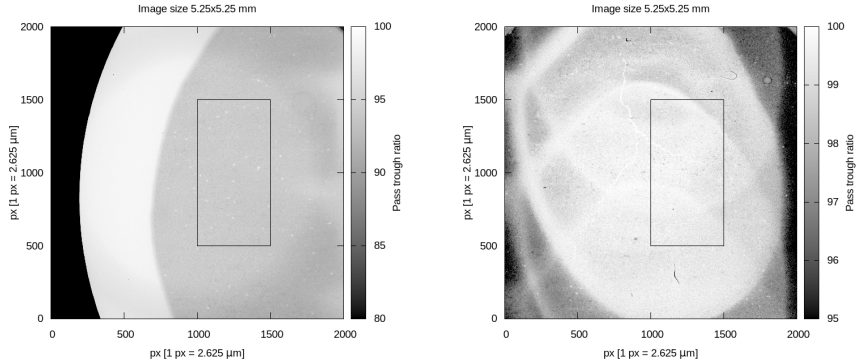

Figure A.1: Left: Edge part of a thallium target. Black part is the aluminium frame. White area is a double layer of carbon and light gray area is where thallium is sandwiched between carbon layers. Right: Center part of a thallium target. The arc shaped lighter areas are worn areas caused by different beam positions. In both figures the black box shows the area from where the attenuation was measured.

Bibliography

[1] P. Reiter et al. *Phys. Rev. Lett.*, 82:509–512, Jan 1999.

[2] A. N. Andreyev et al. *Nature*, 405(6785):430–433, May 2000.

[3] Kai Siegbahn. *Alpha-, beta- and gamma-ray spectroscopy Volume 1.* North-Holland publishing company, Netherlands, 1965.

[4] Professor E. Rutherford F.R.S. and H. Robinson M.Sc. *Philosophical Magazine Series 6*, 26(154):717–729, 1913.

[5] K.-E. Bergkvist et al. *Nuclear Physics B*, 39:371 – 406, 1972.

[6] R. A. R. Tricker. *Mathematical Proceedings of the Cambridge Philosophical Society*, 22(3):454–463, 1924.

[7] J. Van Klinken et al. *NIM*, 98(1):1 – 8, 1972.

[8] W. Neumann et al. *Nuclear Instruments and Methods*, 164(3):539 – 545, 1979.

[9] M.P. Metlay et al. *NIM A*, 336(1–2):162 – 170, 1993.

[10] T. Kibédi et al. *NIM A*, 294(3):523 – 533, 1990.

[11] P.A. Butler et al. *NIM A*, 381(2–3):433 – 442, 1996.

[12] H. Kankaanpää et al. *NIM A*, 534(3):503 – 510, 2004.

[13] S. Ketelhut et al. *NIM A*, 753:154 – 163, 2014.

[14] J. Andrzejewski et al. *NIM A*, 585(3):155 – 164, 2008.

[15] J. Perkowski et al. *Review of Scientific Instruments*, 85(4):043303, 2014.

[16] J. Konki et al. *EPJ Web of Conferences*, 63:01019, 2013.

[17] P. Papadakis et al. *JPS Conf. Proc.*, 6:030023, 2015.

[18] R. H. Stuewer. *George Gamow Symposium; ASP Conference Series*, 129:29, 1997.

[19] J. Chadwick. *Nature*, 129:312, Feb 1932.

[20] Kenneth S. Krane. *Introductory Nuclear Physics*. John Whiley & Sons Inc., USA, 1988.

[21] C.F.v. Weizsäcker. *Z. Phys.*, 96(7-8):431–458, 1935.

[22] K. Heyde. *Basic ideas and consepts in nuclear physics*. Institute of Physics publishing, London, UK, 2004.

[23] M. Goeppert-Mayer. *Phys. Rev.*, 75:1969–1970, Jun 1949.

[24] M. Goeppert-Mayer. *Phys. Rev.*, 78:16–21, Apr 1950.

[25] M. Goeppert-Mayer. *Phys. Rev.*, 78:22–23, Apr 1950.

[26] John Lilley. *Nucler physics - Prinsiples and applications*. John Whiley & Sons., England, 2004.

[27] The On-Line Encyclopedia of Integer Sequences. A018226. `https://oeis.org/A018226`, 2015.

[28] P. A. Butler and W. Nazarewicz. *Rev. Mod. Phys.*, 68:349–421, Apr 1996.

[29] S.G. Nilsson et al. *Kgl. Danske Videnskab. Selskab. , Mat. Fys. Medd. 29 No 16*, pages 1–69, 1955.

[30] R. F. Casten. *Nuclear structure from a simple perspective*. Oxford Univesity press, Oxford, UK, 2000.

[31] R.B. Firestone. *Table of Isotopes 8th edition. V.S. Shirley, John Wiley and Sons*, 1996.

[32] C. S. Wu et al. *Phys. Rev. C*, 45:2507, 1992.

[33] S. M. Harris et al. *Phys. Rev.*, 138:B509–B513, May 1965.

[34] J. Rubert et al. *J. Phys: Conference Series*, 420(1):012010, 2013.

[35] Aage Bohr and Ben R. Mottelson. *Nuclear Structure Volume II: Nuclear Deformations*. World Scientific Publishing Co. Pte. Ltd., Singapore, 2008.

[36] F.P. Larkins. *Atomic Data and Nuclear Data Tables*, 20(4):311 – 387, 1977.

[37] J. Kantele. *Handbook of nuclear spectrometry*. Academic press limited, Great Britain, 1995.

[38] T. Kibédi et al. *NIM A*, 589(2):202 – 229, 2008.

[39] J. Lange, Krishna Kumar, and J. H. Hamilton. *Rev. Mod. Phys.*, 54:119–194, Jan 1982.

[40] M. Mayer. *Naturwissenschaften*, 17(48):932–932, 1929.

[41] J. Weneser E. L. Church. *Phys. Rev.*, 103:1035–1044, 1956.

[42] J. O. Rasmussen. *Nucl. Phys.*, 19:85–93, 1960.

[43] J. Weneser E. L. Church. *Phys. Rev.*, 109:1299–1306, 1958.

[44] J.L. Wood. *Nuclear Physics A*, 651(4):323 – 368, 1999.

[45] A. M. Oros. *Nuclear Physics A*, 645(1):107 – 142, 1999.

[46] K. Helariutta et al. *Eur. Phys. J. A*, 6(3):289–302, 1999.

[47] J. Kantele et al. *Z. Phys. A*, 289(2):157–161, 1979.

[48] E. Der Mateosian and A.W. Sunyar. *Atomic Data and Nuclear Data Tables*, 13(4):391 – 406, 1974.

[49] E. Der Mateosian and A.W. Sunyar. *Atomic Data and Nuclear Data Tables*, 13(5):407 – 462, 1974.

[50] Kenneth S. Krane. *Atomic Data and Nuclear Data Tables*, 19(4):363 – 416, 1977.

[51] Toshimitsu Yamazaki. *Nuclear Physics*, 44:353 – 398, 1963.

[52] L. A. Currie. *Analytical Chemistry*, 40(3):586–593, 1968.

[53] H. Kankaanpää et al. *University of Jyväskylä, Research report No.8/2001*, 2001.

[54] P. J. Nolan et al. *Annual Review of Nuclear and Particle Science*, 44(1):561–607, 1994.

[55] J. Sorri et al. *Phys. Scr. 85*, page 055201, 2012.

[56] J. Pakarinen et al. *EPJ A*, pages 50–53, 2014.

[57] Department of Physics University of Jyvaskyla. K130 cyclotron. `https://www.jyu.fi/fysiikka/en/research/accelerator/accelerator/index_html/accelerator/accelerator/k130/`, 2015.

[58] C.W. Beausang et al. *NIM A*, 313(1–2):37 – 49, 1992.

[59] C. R. Alvarez et al. *Nuclear Physics News*, 3(3):10–13, 1993.

[60] G. Duchêne et al. *NIM A*, 432(1):90 – 110, 1999.

[61] M. Leino et al. *NIM B*, 99:653, 1995.

[62] J. Sarén et al. *NIM A*, 654(1):508 – 521, 2011.

[63] R.D. Page et al. *NIM B*, 204:634 – 637, 2003.

[64] Cobham plc. Opera 3d. `http://www.cobham.com/`, 2015.

[65] European Synchrotron Radiation Facility. Radia. `http://www.esrf.eu/Accelerators/Groups/InsertionDevices/Software/Radia`, 2015.

[66] P. Papadakis. *University of Liverpool, PhD Thesis*, 2010, Accessed 2015-06-17.

[67] JULABO GmbH. Julabo fp89-me. `http://goo.gl/mquP8v`, 2015.

[68] I.H. Lazarus et al. *IEEE Trans. Nucl. Sci.*, 48:567, 2001.

[69] A. Georgiev et al. *IEEE Trans. Nucl. Sci.*, 41:1116, 1994.

[70] P. Rahkila. *NIM A*, 595:637, 2008.

[71] S. Antalic. *NIM A*, 530:185–193, 2004.

[72] Inc. Glassman High Voltage. Glassman eh50n2. `http://goo.gl/cUJgUI`, 2015.

[73] I.S. Grant & W.R. Philips. *Electromagnetism.* John Whiley & Sons Ldt., England, 2004.

[74] TH. Lindblad et al. *NIM*, 126:397–406, 1975.

[75] D. Cline et al. *Ann. Rev. Nucl. Part. Sci.* , 36:683–716, 1986.

[76] G. Breit. *Proceedings of the national academy of sciences*, 67(4):849–855, 1967.

[77] J. Kalef-Erza. *NIM*, 195:587–595, 1982.

[78] D. M. Cox et al. *Proceedings of the Fifth International Conference on ICFN5*, pages 332–339.

[79] J. Sorri et al. *NIM A*, 812:24 – 32, 2016.

[80] NIST physics laboratory. Estar program. `http://physics.nist.gov/PhysRefData/Star/Text/ESTAR.html`, 2015.

[81] G. D. Archard et al. *Journal of Applied Physics*, 32(8):1505–1509, 1961.

[82] J.D. Meyer et al. *NIM B*, 190(1–4):379 – 382, 2002.

[83] V. B. Ndocko-Ndongue et al. *J. Phys. C*, 11(9):1733, 1978.

[84] ORTEC. Energy Loss with Heavy Charged Particles (Alphas). `www.ortec-online.com/download/Energy-Loss-Heavy-Charged-Particles-Alphas.pdf`, 2015.

[85] NIST physics laboratory. Astar program. `http://physics.nist.gov/PhysRefData/Star/Text/ASTAR.html`, 2015.

[86] D. M. Cox et al. *Eur. Phys. J. A*, 51(6):64, 2015.

[87] International Atomic Energy Agency. Angular correlation coefficients. `https://www-nds.iaea.org/xgamma_standards/angcorr.htm`, 2015.

[88] J. Smallcombe et al. *Phys. Lett. B*, 732:161–166, 2014.

[89] P. E. Garrett et al. *J. Phys. G*, 27(1):R1, 2001.

[90] J.H. Hamilton et al. *Nuclear Data Sheets. Section A*, 1(0):521 – 602, 1965.

[91] Brookhaven National Laboratory National Nuclear Data Center. Nudat2 database. 2015, Accessed: 2015-05-22. `http://www.nndc.bnl.gov/nudat2/`.

[92] J.H. Hamilton et al. *Nuclear Data Sheets. Section A*, 1:521 – 602, 1965.

[93] J.S. Dionisio et al. *NIM A*, 414(2–3):239 – 260, 1998.

[94] T. Möller et al. *Phys. Rev. C*, 86:031305, Sep 2012.

[95] M. Scheck et al. *Phys. Rev. C*, 83:037303, Mar 2011.

[96] Kenneth S. Krane. *Atomic Data and Nuclear Data Tables*, 16(4):383 – 408, 1975.

[97] J.L. Wood, E.F. Zganjar, C. De Coster, and K. Heyde. *Nuclear Physics A*, 651(4):323 – 368, 1999.

[98] K. Wimmer et al. *AIP Conference Proceedings*, 1090(1):539–543, 2009.

[99] P. Finocchiaro. *Nuclear Physics News*, 24(3):34–39, 2014.

[100] R. Julin et al. *J.Phys. G*, 27(7):R109, 2001.

[101] R. Julin et al. *J. Phys. G*, 43(2):024004, 2016.

[102] T. Grahn et al. *Phys. Rev. Lett.*, 97:062501, Aug 2006.

[103] T. Grahn et al. *Nuclear Physics A*, 801(3–4):83 – 100, 2008.

[104] B. Andel et al. *AIP Conference Proceedings*, 1681:–, 2015.

[105] P.T. Greenlees. Electron spectroscopy at jyfl, sacred @ ritu. `http://irfu.cea.fr/Sphn/Deformes/Exotag/11052004/Paul.pdf`, 2004. Presentation at Exotag Workshop on Spectroscopy of heavy elements with VAMOS.

[106] K.-H. Schmidt et al. Gamma-spectroscopic investigations in the radiative fusion reaction 90zr + 90zr. *Physics Letters B*, 168(1–2):39 – 42, 1986.

[107] R. S. Simon et al. *Z. Phys A*, 325(2):197–202.

[108] Paul E. S. et al. *Phys. Rev. C*, 51:78–87, Jan 1995.

[109] J. Pakarinen et al. *ISTROS 2015 conference proceedings*, Submitted.